UNIVERSITAT ROVIRA I VIRGILI

NOVEL ELECTRON ACCEPTORS AND NEW SOLUTION PROCESSED HOLE BLOCKING LAYER FOR ORGANIC SOLAR CELLS

Caterina Stenta

UNIVERSITAT
ROVIRA i VIRGILI

Novel electron acceptors and new solutions processed hole blocking layer for organic solar cells

Caterina Stenta

DOCTORAL THESIS
2018

UNIVERSITAT ROVIRA I VIRGILI
NOVEL ELECTRON ACCEPTORS AND NEW SOLUTION PROCESSED HOLE BLOCKING LAYER FOR ORGANIC SOLAR CELLS
Caterina Stenta

Novel electron acceptors and new solution processed hole blocking layer for organic solar cells

Caterina Stenta

Doctoral Thesis
Tarragona 2018

UNIVERSITAT ROVIRA I VIRGILI

UNIVERSITAT ROVIRA I VIRGILI
NOVEL ELECTRON ACCEPTORS AND NEW SOLUTION PROCESSED HOLE BLOCKING LAYER FOR ORGANIC SOL
Caterina Stenta

NOVEL ELECTRON ACCEPTORS AND NEW SOLUTION PROCESSED HOLE BLOCKING LAYER FOR ORGANIC SOL
Caterina Stenta

Caterina Stenta

Novel electron acceptors and new solution processed hole blocking layer for organic solar cells

Doctoral Thesis

Supervised by

Dr. Lluís Francesc Marsal Garví

Department of Electronic, Electrical and Automatic Control Engineering

Nano-Electronic and Photonic Systems (Nephos)

UNIVERSITAT ROVIRA I VIRGILI

Tarragona

2018

UNIVERSITAT ROVIRA I VIRGILI
NOVEL ELECTRON ACCEPTORS AND NEW SOLUTION PROCESSED HOLE BLOCKING LAYER FOR ORGANIC SOL
Caterina Stenta

UNIVERSITAT ROVIRA I VIRGILI

Departament d'Enginyeria Electrònica, Elèctrica i Automàtica

Escola Tècnica Superior D'Enginyeria

Campus Sescelades

Avinguda dels Països Catalans, 26

43007 Tarragona

Espanya

Tel.: + 34 977 559 610 / 559 728

Fax: + 34 977 559 605

Lluís Francesc Marsal Garví, full professor of the Departament of Electronic, Electrical and Automatic Control Engineering of the Universitat Rovira i Virgili,

CERTIFY:

That the present study, entitled "Novel electron acceptors and new solution processed hole blocking layer for organic solar cells", presented by Caterina Stenta for the award of the degree of Doctor, has been carried out under my supervision at the Department of Electronic, Electrical and Automatic Control Engineering of this university, and that it fulfils all the requirements to be eligible for the Doctorate Award.
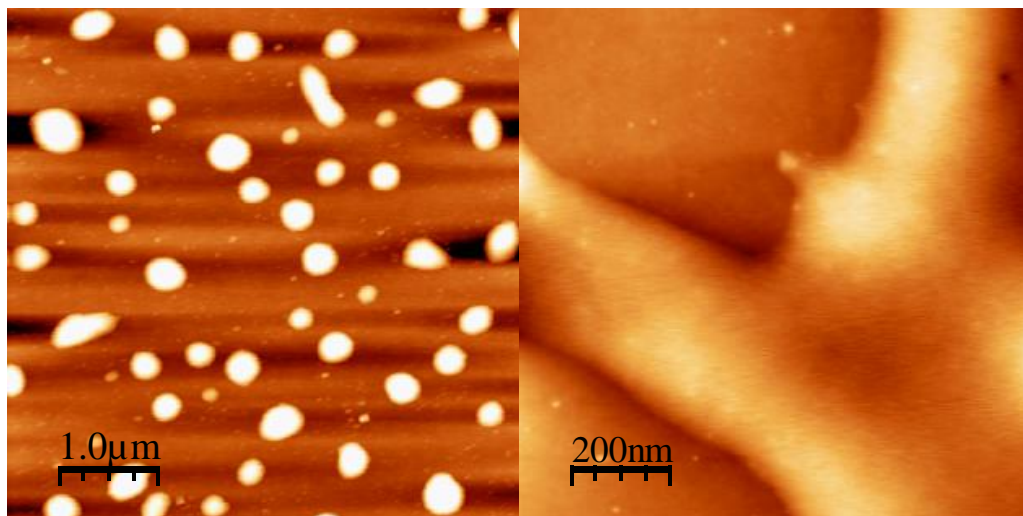
Tarragona, 23rd March 2018

Doctoral Thesis Supervisor

UNIVERSITAT ROVIRA I VIRGILI
NOVEL ELECTRON ACCEPTORS AND NEW SOLUTION PROCESSED HOLE BLOCKING LAYER FOR ORGANIC SOL
Caterina Stenta

For my family

"Life is and will ever remain an equation incapable of solution,
but it contains certain known factors"
Nikola Tesla

NOVEL ELECTRON ACCEPTORS AND NEW SOLUTION PROCESSED HOLE BLOCKING LAYER FOR ORGANIC SOLAR CELLS

Caterina Stenta

Acknowledgments

Contents

Chapter 1

Introduction

The limited supply of today's main energy sources in the form of oil, coal, natural gas and uranium and their adverse effects on the environment have focused research attention on alternative, renewable energy sources. The burning of fossil fuels by humans is the largest source of emissions of carbon dioxide and has dramatic contribution to global warming. Nuclear energy - an alternative to fossil fuels - besides the issue of waste management, has severe dangers associated with the nuclear radiation, highlighted by the disaster at Three Mile Island in 1979, Chernobyl in 1986, at the Fukushima power plants in 2011.

Reducing the reliance on both fossil fuels and nuclear energy by replacing them with renewable energy sources is therefore necessary to provide the future generations a habitable planet. Among all the renewable energy sources, solar energy is a promising alternative as it is by far the most abundant energy source. Sun delivers in fact more energy than the whole mankind needs. The net solar power input to the earth is more than 10000 times humanity's current rate of use of fossil and nuclear fuels [1].

Indeed, with a daily solar radiation in the order of 1.74×10^{17} Watt [1], this amounts roughly to the global energy consumption in a whole year.

Photovoltaic solar cells are thus a promising way for addressing these key energy challenges. Currently, the record laboratory solar cells efficiency are obtained with the multijunction cells with efficiency up to 46%, however the preparation of such devices is still too expensive as the input energy used for the preparation is higher than the energy obtained from them during their lifetime , limiting their applicability.

The photovoltaics market is still dominated by the single junction silicon solar cells, with demonstrated efficiency up to 25%, due to the excellent charge transport properties and environmental stability of high purity silicon. Si-based PV technology accounted for about 94% of the total production in 2016, shared between mono- and poly-crystaline Silicon technology. If mono-crystalline Si dominated the market for the last few decades, the share of multi-crystalline technology has now reached about 70% of total production [2].

Although the latest monocrystalline silicon PV modules are highly efficient, they are also

expensive because the manufacturing processes are slow, require highly skilled operators, and are labour- and energy- intensive.

As a result, numerous approaches to reduce the cost of crystalline silicon PV cells, or increasing their efficiency, have been under development during the past 20 years.

As alternative to the crystalline silicon (c-Si) devices, thin-film silicon devices have been largely studied and together with the other thin-film technologies based on cadmium-telluride (Cd-Te), copper-indium-gallium-selenide (CIGS), copper-indium-diselenide (CIS), are the leading contenders for large-scale production, taking around 6% of the market [2].Thin film CIGS cells have attained the highest laboratory efficiencies of all thin film devices, around 20% [3].

Thin-film silicon devices are based on either amorphous silicon (a-Si:H) or microcrystalline (also called nanocrystalline) silicon (μc-Si:H). Amorphous silicon cells are much cheaper to produce than those made from crystalline silicon. a-Si:H is also a better absorber of light, so thinner and thus cheaper films can be used.

Modules based on all of these technologies have reached the production stage, but production volumes are small [1].

A radical different, photoelectrochemical approach to produce cheaper technologies, has led to the development of the Dye-sensitized solar cells (DSSC).

The actual version of a dye solar cell was originally invented in 1988 by Brian O'Regan and Michael Grätzel and this work was further optimized until the publication of the first high efficiency DSSC in 1991[4].

In contrast to the conventional system where the semiconductor assumes both the task of light absorption and charge carrier transport, in the DSSC these two functions are separated. In these solar cells, the contacting phase of the semiconductor is replaced by an electrolyte, liquid, gel or solid, forming a photo-electrochemical cell.

The light is absorbed by a sensitizer and charge separation takes place at the interface via photo-induced electron injection from the dye into the conduction band of the solid.
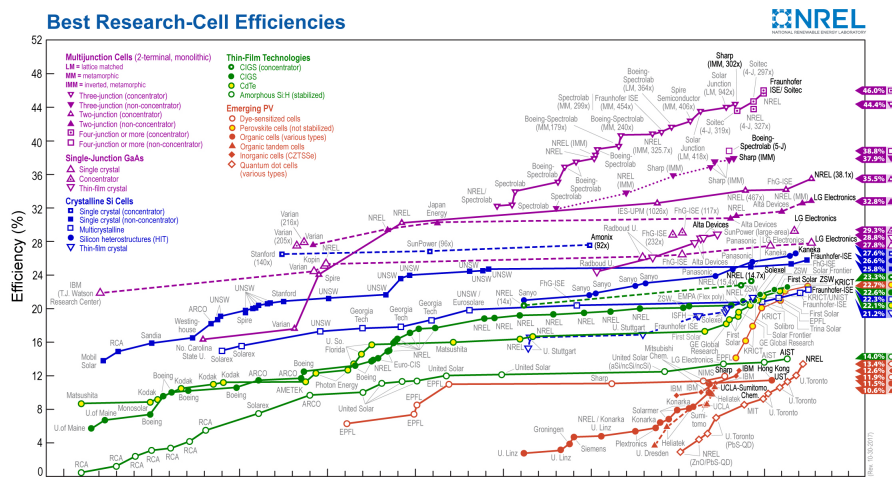
Figure 1.1 Reported timeline of solar cell energy conversion efficiencies since 1976, NREL [3].

Further research for low cost solar cells has led researcher to organic semiconductors as possible alternative candidates.

From the late 90' these two technologies have been widely investigated, but from 2012 DSSCs have lost interest in the PVs research field, leaving the organic semiconductors as one of the most investigated technologies to date.

The use of organic semiconductor materials opens, in fact, the possibility for a further decrease of solar cell production costs. After the discovery of polymer with both conductive and semiconductor properties in 1906 [5] such materials have been intensively studied for different PV applications. Extensive research over the last 5 years has produced increases in the efficiency of OPV devices. The current certified record of power conversion efficiency is 13.2% as reported by the National Renewable Energy Laboratory [3].

Organic photovoltaics (OPV) has been developed rapidly in the past decade because the semiconductor materials are earth-abundant and because they can be produced using solution phase techniques, such as ink jet printing or coating using roll-to-roll (R2R) machinery, thus allowing for fast, simple, low-cost and large-volume processing. The potential speed and simplicity of OPV processing is unmatched by other current technologies.

Additionally, organic semiconductors have very high absorption coefficients, which allow very thin films to be used, whilst still absorbing a sufficient portion of the solar spectrum. This property allows OPV devices to be flexible and thus be used in many situations where inorganic cells cannot, such as in complex surfaces.

The key issue for the commercialization of flexibles and low cost organic devices and for the further progress in the OPV field is the deposition process of each material.

In recent years much research have focused on the perovskite solar cells, another emerging thin film technology which includes a perovskite structured compound, most commonly a hybrid organic-inorganic lead or tin halide-based material, as the light-harvesting active layer. Solar cell
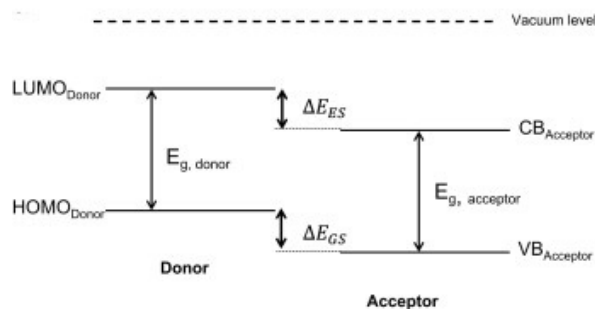
Figure 1.2 General energy band diagram of the heterojunction formed in a hybrid solar cell[6].

efficiencies of these devices have increased in the last years, making them the fastest-advancing solar technology to date.

1.1 Organic solar cell operating principles

The main difference in the working principle between organic and inorganic PV lies in the manner in which charges are generated under illumination. In the inorganic material, when the photon is absorbed, free charge carriers are created. For example, in a silicon solar cell, upon photo excitation an electron from the valence band is promoted to the conduction band, thus forming an electron-hole pair. Due to the crystalline nature of the silicon lattice, these charge carriers experience only a small force of interaction, that is, absorption in silicon leads to effectively free charge carriers.

Whereas, in organic semiconductors there exists a large electrostatic force between electrons and holes, due the much lower relative dielectric constant in comparison to inorganic semiconductors. This difference strongly dictates the charge generation mechanism for each type of devices.

The operating mechanism of an OSC is therefore a multi-step process. When a photon is absorbed in the organic material, an excited electron-hole pair is formed, where the electron and hole are coulombically bound. This excited state is referred to as an "exciton". A force is needed to overcome this excitonic binding energy so that free charge carriers can be created and transported throughout the device and to the electrodes. The force needed to overcome the exciton binding energy is given by the differences between the highest occupied molecular orbital (HOMO) of the donor and the lowest unoccupied molecular orbital (LUMO) of the acceptor. This energy offset used to dissociate excitons is denoted as Δ_{ES} in figure 1.2, which is the excited state energy offset.

The photoelectric conversion process in OPV can be described in 4 steps:

1) Exciton generation: absorption of a photon and generation of an exciton: Ehen a photon is absorbed in the donor material an electron is "promoted" to the LUMO, while leaving the
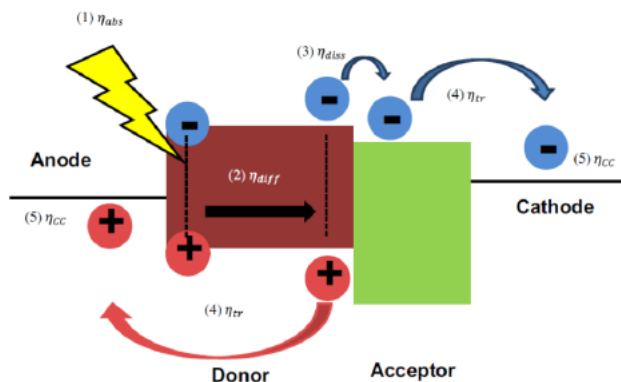
Figure 1.3 Energy band diagram illustrating the five steps in the charge transfer process. The efficiency of these steps determines the EQE of the hybrid device [6].

positive charge in the HOMO. This excited pair is still bound by coloumb attraction forces, forming an exciton.

2) Excition diffusion: migration of the exciton to the interface of the donor and acceptor material through diffusion.

3) Exciton dissociation: the excited electron on the donor is transferred to the LUMO of the acceptor at the donor-acceptor interface, forming a charge transfer state (CTS). The electron transfer process follows Markus theory and the thermodynamics of it are linked to the energy difference between the highest occupied molecular orbital (HOMO) of the donor and the lowest unoccupied molecular orbital (LUMO) of the acceptor [7].This energy offset is denoted as Δ_{ES} in figure 1.2. This hole-electron pair is still bound by coloumbic attraction forces.

4) Charge separation: the CTS undergoes charge separation to free charge carriers (or charge separated state (CST)) whose kinetics are described by Onsager's model [8]. The electron is transported to the cathode for charge collection through acceptor domains. The hole produced in the donor material travels throughout the donor fraction and is collected at the anode. This mechanism is displayed in figure 1.3. The free charge collection at opposite electrodes is achieved by the asymmetric ionization energy or work function of the electrodes, that means a discrepancy between the work function of the anode and the cathode electrode material is required to provide a direction for the photocurrent. The same process also occurs for the acceptor, albeit that the acceptor donates a hole to the donor.

There are competing processes that also occur during the abovementioned steps that can lead to losses in efficiency, they can be summarized as follows:

• Exciton recombination occurs because the exciton has a limited lifetime. The kinetics of recombination are generally slow compared to exciton diffusion and exciton dissociation.

• The lack of injection: if the offset between the excited state energy of the donor and electron affinity of the acceptor is not sufficient the injection will be limited, leaving the electron to decay to its ground state.

- Geminate recombination: occurs when after charge separation the bound electron recombine with the hole it originated from.

- Non-geminate recombination occurs after charge separation, when a hole and an electron which have escaped the coulombic attraction recombine at the donor-acceptor interface. During transport, if the film has any defects or traps states the free charges may combine with them. It is well established in fact that the charge transport in organic materials occurs via a process of hopping between energy states and is affected by traps and recombination sites in the photoactive film.

- Surface recombination: depending on the device architecture and film nanostructure charges may recombine at the wrong electrode.

1.2 Device architecture

The common structure of the organic solar cells comprises a multilayer stack. Usually the active layer, which is a combination of donor and acceptor materials, is sandwiched between two electrodes. A discrepancy between the work function of the anode and the cathode electrode material is required to provide a direction for the photocurrent. One of the electrodes needs to be transparent for illumination of the cell. Buffer layers are applied between the electrodes and the active layer to ensure charge-selective transport.

In the above description of the operating principles of OSC a very simple bilayer structure has been presented, which has the advantage that the photogenerated exciton can migrate to the interface in a facile manner, can undergo charge separation and the electron can be transported through a pure acceptor domain to the cathode, leaving very few problems in charge generation or collection. However bi-layers structures are limited in excitonic dissociation, as there exist only one interface, that is, only the photons absorbed by a very thin layer next to the interface can contribute to the photocurrent while the rest is lost through recombination mechanisms. In fact, the typical exciton diffusion length of an organic molecule is extremely low, being on the order of 10 nm. This is significantly lower than the thickness required for an organic film to absorb all of the sun's photons, typically 1 µm.

That means that any exciton generated more than 10 nm away from the donor-acceptor interface will not reach the interface and separate into free charge carriers.

Increasing the interfacial area should allow improved free charge generation and higher photocurrents. In order to increase the heterointerfacial area, the donor and acceptor material can be mixed in a bulk, forming a nanoscale morphology, called a bulk heterojunction device structure.

In this way, the interface is extended throughout the whole active layer, and the device requires smaller exciton diffusion length, providing more efficient charge separation and separate paths for the transport of free carriers.

Bulk heterojunction (BHJ) devices are most commonly solution processed, as in this thesis, but they can also be processed through co-evaporation [9].
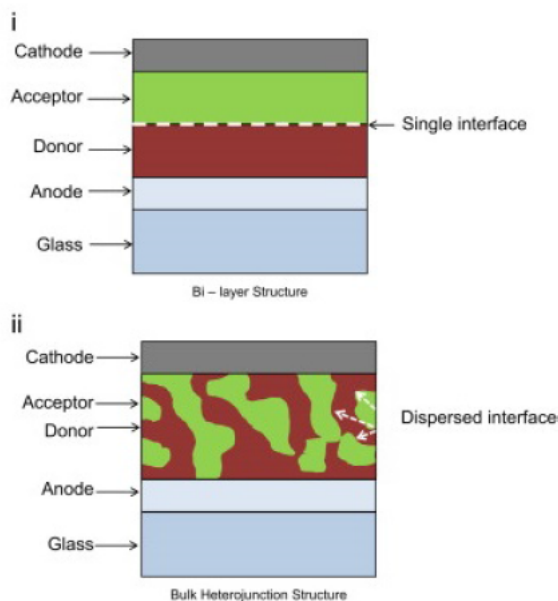
Figure 1.4 Schematic diagram of (i) bi layer heterojunction, and (ii) bulk heterojunction photoactive layers.

In the solution processed BHJs several parameters must be optimized during the fabrication process. As molecules are processed together they must both be compatible and have similar solubility in a given solvent. Furthermore, the solvent must allow for good phase separation between the two materials so that donor-rich domains and acceptor-rich domains are formed. The dimensions of the domains should ideally be on the same order of the exciton diffusion length, so that every exciton can reach the donor-acceptor interface. Also, the morphology of each layer must provide good pathways between each domain. This allows the use of thicker films than those used in the bilayers devices, which allows more light to be absorbed and therefore higher photocurrents.

An important issue for BHJ devices is surface recombination, so the use of buffer layer such as electron transport layer (ETL) and hole transport layer (HTL) is of great importance. The role of those buffer layers is to act as a barrier or selective membrane to prevent unwanted charges reaching the wrong electrode. The most common HTLs are either a polymeric binary mixture composed of poly(3,4-ethylenedioxythiophene) and sodium polystyrene sulfonate (PEDOT:PSS) or transition metal oxides. The optimization of BHJ blend morphologies is critical in order to achieve high performance in OPV devices.

Several parameters must be optimized such as solvent, concentration, processing methods, as well as the post deposition techniques such as annealing via thermal or solvent vapour method. Thermal and solvent annealing have shown to be necessary for improving BHJ morphologies and performance. Thermal annealing consists in heating the film or the complete device to allow the components to arrange in a more favourable configuration.

The molecules may adopt different packing geometries, domain sizes can grow and the surface

energy can change. Applying heat can in fact increase the amount of free energy and improve the electronic properties. Solvent vapour annealing (SVA) induces similar effects and consists in immersing the films in a vessel saturated with solvent vapour. Another BHJ structure is the interdigitated ordered morphology. Ordered structures are generally made by infiltrating polymers into nanostructured oxides, which are used as a template. Previous work from the Marsal's group, focused on fabricating nanopillars BHJ solar cells, where the pillars should have the optimum width to maximize the photogeneration, and the maximum length to ensure all charge carriers can be transported along their length to reach the electrodes. Aluminum oxides templates have been used in previous work to create the nanopillars structure with pore diameter of up to 100 nm The characterization of the nanopillar morphology is key factor to fully understand these type of devices This overview on the different device architectures has illustrated that there are many factors to consider when designing and optimizing a device. Studying all these aspects in more detail is the key to further improve the OSCs characteristics to their full potential.

1.3   Photovoltaic performance characteristics

In this work complete solar cells have been characterized by means of current density-voltage J(V) measurements. Current density-voltage measurements are the most common tool for solar cell evaluation and characterization. These measurements are obtained when photocurrent is measured as the applied potential is varied. To obtain the I-V curve the photocurrent is scanned over a range of voltages under a certain illumination intensity.

To allow for valid comparison of device performance, an international standard intensity for input power is used. This standard is an incident spectrum of AM 1.5 G, which imitates the solar spectrum and is also called 1 sun 1.5 Air Mass Global, which refers to the radiation of the sun at 48.2° from the zenith at sea level. This standard can be approached by commercial solar simulators, which consist of a lamp with stabilized light density flux, the appropriate set of filters to emulate the 1.5 AM G described above, with an intensity of 1000 W/m2, whilst the cell is at a standard temperature of 25°C.

1.3.1   Electrical model

Fig. X shows an equivalent circuit model which is commonly used to interpret the characteristic of PV devices. The circuit is typically used for inorganic solar cells, but although the specific physical processes in organic semiconductors may be different and therefore lead to other parameters, the principal loss mechanism are the same and the same circuit can be applied. The solar cell in the dark acts as a simple diode: the current-voltage relationship follows the exponential relation of the pn-junction, the Shockley equation:

$$J(V) = J_0(e^{qV/AkT} - 1)$$

1.3. PHOTOVOLTAIC PERFORMANCE CHARACTERISTICS 11
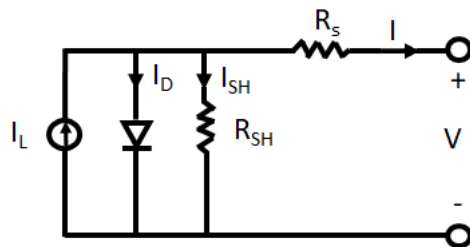
Figure 1.5: The equivalent circuit of a solar cell.

Eq.1.1

Where k is the Boltzmann constant, T the absolute temperature, V is the voltage across the terminals, J(V) the current density, A the diode quality factor and q the elementary electric charge. J(V) is obtained by dividing the current to the device area [9].

For a better description of a real device, resistive losses need to be added into this equation: A series resistance Rs and a shunt resistance Rsh. Additionally, a photo-generated current density J_L has to be introduced into the equation to describe the device mechanism under illumination (in the dark J_L=0). In thin film solar cells, JL may depend on the applied bias voltage. The so called 1-diode model describing the current-voltage characteristic of a solar cell is given by the following equation:

$$J(V) = J_0 \left[exp(\frac{q(V - R_s J(V))}{AkT}) - 1 \right] + \frac{V - R_s J(V)}{R_p} - J_L$$

Eq. 1.2

Where J(V) accounts for the current density flowing through the device which is the sum of the current density flowing through the diode (first term), the current density flowing through the parallel resistance (second term) and the photo-generated current density (last term) [10].
The illuminated cell behaviour can be related to that of a diode parallel connected with a current source R_S, these connected in series with a shunt resistance R_{SH}.
• The diode D takes into account the current losses due to recombination in the interior of the cell. D has an ideality factor n and a saturation current I_0 (current in the dark at reverse bias);
• The current source is equivalent to the photo generated current due to the PV effect I_L;
• R_S considers all the resistances at interface in the layers, the conductivity of the semiconductors, and the electrodes;
• R_{SH} takes into account the recombination of charge carriers near the dissociation site (e.g. D/A interface). Low shunt resistance causes power losses in solar cells by providing an alternate current path for the light-generated current. This reduces the amount of current flowing through

the solar cell junction and reduces the voltage from the solar cell. The effect of a shunt resistance is particularly severe at low light levels, since there will be less light-generated current. So, for good performance of the OPV device, R_S needs to be low and R_{SH} to be high);

• Solar cell voltage V: the cell can generate a voltage between 0 and V_{OC} depending on the size of the load resistor. In order to obtain IV curve data in the other voltage ranges in the IV curve an external voltage source is required [10].

We note that also the voltage drops across a load resistor - the range between 0 and V_{OC} - can be simulated by the same voltage source so that the entire range can be scanned by applying an external voltage. These are the components of a ECD with which we can associate the most important effects in solar cells of all types. However a more comprehensive ECD for organic devices may comprise other extra components, such as another diode D2 , a capacitor C and an extra shunt resistor R_{SH2} [9].

The I-V characteristic for a typical solar cell, when light is shone on the device, becomes a superposition of the dark J-V with the light-generated current with the curve shifted by a quantity equal to the current that is generated by the cell. The characteristic curve of an illuminated solar cell can be presented by considering only the fourth quarter of the graph and with an inverted current verse. This facilitates the determination of the basic parameters. The J-V characterization means the determination of the basic parameters: the open circuit voltage V_{OC}, the short-circuit current J_{SC}, the fill factor FF, and efficiency η which are determined by only three points on the J-V curve and are briefly described below.

1.3.2   Power conversion efficiency

The power conversion efficiency (PCE) of a solar cell is defined with the following formula:

$$PCE = \frac{J_{SC} \times V_{OC} \times FF}{P_{in}}$$

<div align="right">Eq. 1.3</div>

Where J_{SC} is the short circuit current density, V_{OC} , is the open circuit voltage, FF is the fill factor and P_{in} is the incident power of the lamp [9].

1.3.3   Fill factor

The fill factor describes the "squareness" of the J-V curve. It is the ratio between the maximum product of J and V and the product Voc and Isc.

$$FF = \frac{J_m \times V_m}{J_{SC} \times V_{OC}}$$

<div align="right">Eq. 1.4</div>

Thus

$$P_{max}(JV) = V_{OC} \times J_{SC\times} FF$$

<div align="right">Eq. 1.5</div>

Where J_m and V_m are the current density and voltage at the maximum power point [9]. The maximum power point (P_m) determines the operating point where the delivered power to the load resistance will be the highest possible. The higher the FF the more the J-V characteristics resembles a constant current source with a maximum voltage and the higher is the electric power that can be extracted. The voltage-current (V_p, I_p) combination that gives the largest power rectangle is called the maximum power point. Due to physical constraint on diode quality, the practical limit to the FF is less than the ideal value of 1 [6]. The FF can be limited by several reasons, such as a miss-match in charge carrier mobilities of the donor and acceptor material, large series resistance (R_S) or low parallel shunt resistance (R_{SH}), poor contacts or recombination (geminate and/or non-geminate).

1.3.4   Open circuit voltage

V_{OC} can be derived quantitatively using:

$$V_{OC} = \frac{nkT}{q} ln\left(\frac{I_L}{I_0} + 1\right)$$

<div align="right">Eq. 1.6</div>

In contrast to inorganic solar cells, the origin of the V_{OC} in OSCs is still under discussion. Multiple reports have investigated this property for OPV devices and have shown that most likely the origin of the V_{OC} is determined by the potential energy differences at the donor/acceptor interface, and by the recombination kinetics of the charge carriers [11]. The potential energy at the donor/acceptor interface derives from the differences between the HOMO level of the donor and the LUMO level of the acceptor. In 2006 a report studied the relationship between the energy levels of the donor-acceptor blend and the Voc for bulk heterojunction devices [12]. It was found that there exists a linear relationship between the HOMO position, which is related to the band gap of the heterojunction, and the Voc. This relationship between the HOMO of the donor material and the V_{OC} of the device was found:

$$V_{OC} = \frac{1}{e}(\mid E^{Donor}HOMO \mid - \mid E^{Acceptor}LUMO \mid) - 0.3V$$

<div align="right">Eq. 1.7 [6]</div>

By definition the V_{OC} is the voltage at which no current flows between the terminals (I=0 A) but there is of course current being generated within the device, but this photocurrent is being balanced by recombination current in the device. The recombination rate scales with the

equilibrium charge carrier concentrations and therefore exponentially with the energy levels, with changes in energetics having a large influence on V_{OC}. The more charges are generated, the faster the charges recombine. Increasing applied bias, leads to an increase in potential energy within the device and thus an increase in the recombination current. So the V_{OC} can be estimated by taking into account the flux of photogenerated charges and the flux of charge recombining non-geminately:

$$J_{tot} = J_{gen} + J_{loss}$$

<div align="right">Eq. 1.8 [9]</div>

Where J_{gen} is the generation current density, which in a device with neglible field dependent generation can be assumed to be J_{SC} and J_{loss} is the current density lost to non-geminate recombination. J_{loss} is obtained by considering the ratio between the charge carrier density, n, and the charge carrier lifetime τ_n:

$$J_{loss} = \frac{edn}{\tau_n}$$

<div align="right">Eq. 1.9</div>

Where e is the elementary charge and d is the active layer thickness. This approximation is key to understand the importance of charge carrier kinetics in controlling the V_{OC}.

1.3.5 Short circuit current density

The short circuit current density J_{SC} is the maximum photocurrent density which can be extracted from the device at short circuit conditions, that is when no voltage is applied.

It is the point where the J-V curve crosses the y-axis. The J_{SC} is directly related to the external quantum efficiency (EQE), which is defined as the ratio between the number of electrons on the external circuit and the number of incident photons at a specific wavelength.

J_{SC} can be expressed as [6]:

$$J_{SC} = \frac{q}{hc} \sum \int_{\lambda min}^{\lambda max} EQE \times P_{in}(\lambda)\lambda \times d\lambda$$

<div align="right">Eq. 2.0</div>

For the operation of a hybrid solar cell, EQE is dependent on five major steps, each of which has some associated efficiency. Thus is can be expressed as:

$$EQE = \eta_{abs} \times \eta_{diff} \times \eta_{tr} \times \eta_{cc}$$

<div align="right">Eq. 2.1</div>

The parameter η_{abs} describes the absorption yield of the device. The absorption spectrum of the material is determined by both the band gap and absorption coefficient of the material, whilst the thickness of the photoactive layer will also affect the absorption yield [13].

The parameter η_{diff}, describes the ability of an exciton to diffuse to a donor-acceptor interface. This parameter depends on both the exciton diffusion length, which is a material property, and the distance between excitation and the nearest interface, which is related to the nanoscale design of the photoactive layer. As the excitonic diffusion length in conjugated polymers is very low, control over the D-A morphology is important for successful exciton diffusion. The parameter η_{diff} is the exciton dissociation yield. The energy offset, required to allow conduction to occur, must be larger than the excitonic binding energy in the material to facilitate charge transfer. This energy is typically in the range of 0.1-0.5 eV [14].

The parameter η_{tr} describes the efficiency of charge carrier transport throughout the device.

The parameter η_{cc} describes the efficiency of charge collection at the electrodes. This represents the ability of the charge carriers to be injected into the electrodes from the photoactive layer. The success of this step is dependent on the electronic composition of the device.

Chapter 2

Organic solar cells overview

Since the discovery of high conductivity in perylene-iodine complex in 1954 [15],organic semiconductors have been under intense research. Organic semiconductors are carbon-based materials possessing semiconductor characteristics. Atoms within an organic semiconductor molecule are bonded by conjugated π-bonds, while molecules are bonded to one another by Van der Waal's forces or hydrogen bonds, considerably weaker compared to the covalent bonds linking atoms in inorganic semiconductors. An organic photovoltaic cell is composed of a film of organic photovoltaic active layer, "sandwiched" between a transparent electrode and a metal electrode. There are two major classes of organic semiconductors: low-molecular weight materials and polymers.

Polymer solar cells (PSCs) have attracted much more attention due to the early discovery of the semiconducting properties of conjugated polymers. Indeed, carbon- based polymers were known to be insulators until 1977 when Alan J. Heeger, Alan G. MacDiarmid and Hideki Shirakawa accidentally discovered that conjugated polymers can gain high conductivity upon doping. They were awarded with Nobel Prize in chemistry "for the discovery and development of electrically conductive polymers" in the year 2000 [16].

The doping process can be done by insertion or removal of electrons from the polymer backbone, corresponding to the reduction or the oxidation, respectively. Shirakawa et. al. doped polyacetylene (PA) with iodine: As iodine is a strong electron acceptor, it disrupted the electron delocalization of PA and enabled the polymer to conduct electricity billion folds more than undoped PA [17]. This breakthrough caused intense research of the other conjugated polymers, such as polyparaphenylene (PPP) and polythiophene (PT) [18].

To allow such R2R technique to be used and thus obtaining flexibles solar cells, it is important that each layer is deposited from a solvent solution. While this requisite has often been met for the electron blocking layer and the absorber layer, the hole blocking layer is been most often produced with water sensitive metals such as Ca, or Metal oxides and is virtually always deposited from vacuum deposition methods. In this work we investigated the use of bathocuproine, a low cost organic molecule, as a hole blocking later deposited from solution processing on polymer based organic solar cells. Another way to further progress in the solution-processed OPV

UNIVERSITAT ROVIRA I VIRGILI
NOVEL ELECTRON ACCEPTORS AND NEW SOLUTION PROCESSED HOLE BLOCKING LAYER FOR ORGANIC SOLAR CELLS
Caterina Stenta

18   CHAPTER 2. ORGANIC SOLAR CELLS OVERVIEW

field, is the implement of low synthetically demanding acceptors to replace the fullerene deriva-
tives. Nowadays fullerene-based acceptors have infact received extensive attention and have led
to PCE superior to 10%. They present however difficult synthesis methods and complicated
purification processes thus leading to higher production costs. The need of more versatile and
less synthetically demanding acceptors, has focused the attention on small molecules acceptors.
In this work we present and study alternative acceptor materials, the perilenediimide (PDI)
family. We present the synthesis and characterization of new PDI derivatives together with a
study of X-Ray and AFM to determine the morphology of these devices. Further experimental
techniques, such as current-voltage, EQE analysis and charge extraction measurements are used
to better characterize the interface.

2.1 Active layer materials for organic solar cells

Many different donor materials, including polymers and small molecule compounds, have been
developed in the past decades. The donor material in the solar cell has beenthe light absorbing
material, a polymer or small molecule, in which an electron is excited and transferred to the
acceptor. Conjugated polymers based on cyanated poly(phenylenevinylene) (PPV) backbones
were the first investigated independently by Friend and Heeger [19].

Both teams demonstrated that photogenerated excitons in the polymer layer can be efficiently
dissociated into free carriers at the photoactive blend interface. Friend and co-workers used a
mixture of two PPV polymers, donor poly(2-methoxy-5-(2'-ethyl-hexyloxy)-1,4-phenylenevinylene)
(MEH-PPV)and acceptor C6-Cyano-polyphenylene (C6-CN-PPV) to fabricate solar cells, while
Heeger and co-workers used the same donor polymer but MEH-CN-PPV as the acceptor.

Further research on the active layer polymers led Arias et al.to investigate the phase sep-
aration and photovoltaic properties of PF8BT in combination with the donor polymer PFB.
PF8BT is a highly luminescent polymer with a high electron affinity (3.53 eV) whereas PFB is a
triarylamine-based hole transporting polymer. Bradley and co-workers [12] employed the same
acceptor (PF8BT) but Poly(3-hexylthiophene) P3HT as the donor polymer [19].

P3HT (Figure 2.1) gained wide popularity as a donor material in OSCs, after it was found
to give improved efficiency when blended with PCBM as an acceptor. The polymer/fullerene
blend scheme as since dominated the field of BHJ OSCs for almost a decade. P3HT is still to
date the most studied polymer for polymer solar cells. The efficiency of a P3HT/PCBM solar
cell is typically 4-5 %, which is close to the optimal performance for this system [20].

The structures of a conjugated polymer play an important role in determining the physical and
chemical properties of donor and acceptor materials and further influence the performance of
solar cells. Materials with a delocalized π electron system can absorb sunlight and create and
transport photogenerated charge carriers.

Most donor polymer or co-polymer structures are obtained from monomers such as thiophene,
fluorine and carbazole. These low band gap polymer donors contribute to a wide spectrum

response and serve as an excellent charge transporter with a high hole mobility.

2.1.1   Donor materials

Polymers

Polythiophene and its derivatives Poly(3-alkylthiophene) (P3AT) have been used as active material for optoelectronic devices, especially for photovoltaic cells. P3HT is the most used and best one in P3ATs as photovoltaic material.

Solar cells with optimized performance have been developed using P3HT/PCBM blends, and these cells feature nearly ideal photon-to-current quantum efficiency (IPCE) in the mid-visible reagion. By using P3HT as a donor material blending with PCBM as acceptor, over 4 % PCE has been reported by different research groups and P3HT has attracted much attention in the OPV field. The high efficiency of P3HT/PCBM devices may result from a unique microcrystalline lamellar stacking in the blends.

The photovoltaic properties of P3HT/PCM system are very sensitive to the morphology of the active layer, this lead researcher to develop processing techniques to control the nanomorphology of the active layer and consequently to improve device performance. It has been demonstrated that device performance can be enhanced by careful selecting the processing solvent, solvent and thermal annealing, and additives.

Further improvement of PCSs in P3HT/PCBM is hindered by its large bandgap (-2.0 eV) [21].

It became therefore important to design polymers that can harvest more photons from the available sunlight. It also important to consider that narrowing the bandgap will cause a decrease in open circuit voltage and thus a decrease in PCE. Through a careful estimation, an optical bandgap of 1.4 eV will be ideal for conjugated polymer as the active absorbing materials blended with PCBM in BHJ solar cells [12].

A few examples are reported below with the description of the most used polymers. PCPDTBT is a donor and acceptor alternating conjugated polymer (Figure 2.1). It possesses an optical bandgap of 1.4 eV (absorption onset 890 nm) and an electrochemical bandgap of 1.7 eV with a HOMO level of -5.3 eV and a LUMO level of -36 eV[22].

This polymer is the first low bandgap polymer with a highly efficient photovoltaic response in the near IR region and has a PCE of 3.2 % blended with PC71BM. Another type of donor polymer is the PsiF-DBT, which is a 2,7-silafluorene (SiF) and a 4,7-di(2'-thienyl)-2,1,3-benzothiadiazole (DBT) alternating polymer with an optical bandgap of 1.8 eV. The HOMO level from electrochemical measurements was -5.4 eV [22].

In a blend with PC60BM the device exhibited a PCE up to 5,4%. This combination is the first low band gap polymer with a PCE over 5%.

A silo-contained polymer, PSPTPB, with similar molecular structure as PCPDTBT was synthesized and also exhibited excellent photovoltaic properties. In PSBTBT, an Si atom was introduces to the bridge point (3, 3' positions) on the bithiophene unit [23].
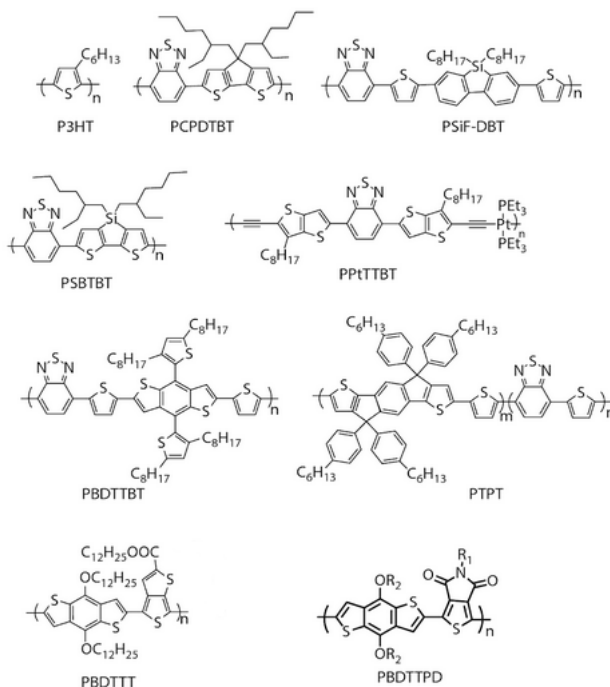
Figure 2.1 Representative donor conjugated polymers.

The silicon atom of PSBTBT can also be replaced by a nitrogen atom, and the polymer PDTPBT was obtained.

PBDTTBT is different from most of linear donor-acceptor type conjugated polymers as it possesses a cross-conjugation segment in its donor. This polymer has three absorption bands, and therefore absorbs widely from 300 to 700 nm with an optical bandgao of 1.75 eV. PBDTTBT presents HOMO and LUMO levels of -5.6 eV and -3.7 eV respectively [24].

Good stability and efficiency were shown by devices fabricated with PTPT as donor together with PC71BM as acceptor, with a PCE of 4.4% [25].

Another class of donor materials which play an important role in the polymer-fullerene solar cells are the DPP-based polymers. Their low bandgap property leads to absorption up to 900 nm, which covers the near-IR energy in the solar spectrum. Various aromatic spacers are copolymerized with the DPP unit, and excellent solar cell performances are achieved [26]. Relatively high hole mobilities of DPP polymer also suppressed the carrier recombination, which ensured a high FF.

A promising donor material in BHJ OPVs recording the remarkable PCE because of its superior optoelectronic properties is the poly(4,8-bis[(2-ethylhexyl)oxy]benzo[1,2-b:4,5-b´]dithiophene-2,6-diyl-alt-3-fluoro-2-[(2-ethylhexyl)carbonyl] thieno[3,4-b]thiophene-4,6-diyl) (PTB7) [14]. The low-band gap polymer PTB7 is well-suited to [6,6]-phenyl-C71-butyric acid methyl ester (PC71BM) which absorbs a broad range of light [27].

Small molecules

Small molecular organic semiconductors with appropriate properties can also be used as electron donor materials in OPV devices.

Although polymers have led to high efficiencies, they present some disadvantages related to their molecular structure. They can present batch-to-batch variations, as well as variations in the molecular weight, polydispersity and purity, which could lead to limited reproducibility. Whereas, the small molecules present better defined structures and are less affected by batch to batch variations. Compared to the polymers they have more versatile molecular structure and can be easier synthetically modified. Recent results in the use of small organic molecules in solution-processed devices have demonstrated a record efficiency of 10 % [28].Various different small molecules have been studied leading to different parameters such as charge carrier mobility, absorption coefficients, film morphology, bad-gap and energy level alignment, a new class of donor materials have been developed. One of the most successful examples are the phtalocyanines (Pc), porphyrins (PQR), the merocyanines (MC), polyacenes, squaraines (SQ), diketopyrrolopyrrole (DPP) and donor-acceptor (D-A) structures based on oligothiophenes.

The DPPs based molecules present some advantages compared to other small molecules, as they are easier to synthesized and they present the possibility to control the morphology using solvent annealing process [29].They present as well good solubility and are thus desirable for solution processed systems. The device performance of the devices made from these donors, is somehow limited by the high HOMO energy level and the imbalance of carrier mobility compromising the FF of the devices [30].

The donor-acceptor (D-A) structures based on oligothiophenes have been recently developed and show some great features [30]. Due to the presence of the thiophenes they present a high absorption coefficient. The concept of these devices is to alternate electron-reach donors and electron-deficient acceptors in the same molecular framework resulting in a reduced bandgap via molecular orbitals hybridization and intramolecular charge transfer. Controlling the molecule energy levels is essential for an effective material development. Choosing a wrong donor or acceptor moieties could lead in fact to a reduction of the absorption capability of the overall molecule, deterioration of the hole mobilities and a bad charge dissociation. The design of the π-bridge molecular backbone is also very important to determine the properties of the molecules.

2.1.2 Electron acceptor materials

Fullerene and derivatives

Fullerene and its derivatives have been widely used as electron acceptor materials in OPVs until the recent surge of non-fullerene acceptors with efficiencies overtaking those of fullerene-based devices.

Sariciftci *et al* reported the efficient photoinduced electron transfer (PET) in a conjugated

polymer-fullerene (Buckminsterfullerene, C_{60}) composite as early as 1992 [14].

In this report, a very fast PET was observed- in the order of femtoseconds- from a conjugated polymer to a fullerene, which is several orders of magnitude faster than any photoexcitation radiative decay or back electron transfer process. Thus, this was a demonstration that the quantum efficiency of charge separation in such a composite can approach the unity.

The tendency of fullerenes (e.g C_{60}, C_{70}) to crystallize in organic solvent and on surfaces, however, leads to unfavourable phase separation in thin film composites. This implies that charge carriers lack the necessary channels to reach the electrodes. To address this drawback, different substituents were introduced on fullerene conjugated core.

In 1995, Hummelen and Wudl first reported an approach to synthesize a 6,6]-phenyl-C61-butyric acid methyl ester functionalized C_{60} ($PC_{61}BM$). Heeger et al. first described $PC_{61}BM$ as an acceptor blended with a conjugated polymer (MEH-PPV) as donor, and achieved much higher efficiency compared with C_{60}-based photovoltaic devices.

$PC_{61}BM$ later became one of the most used fullerene derivative in OPVs, exhibiting excellent photovoltaic properties as electron acceptor material and excellent solubility in various organic solvents. The replacement of C_{60} with the more soluble and less symmetrical $PC_{61}BM$ decreases the formation of large fullerene clusters and therefore, increases the possibility to form a D-A interpenetrating network materials in the active layer [31].

This network, with a large conjugated polymer:fullerene interfacial area and the appropriate phase domain size, fits the required compromise between optical length and exciton diffusion length. Since then, many efforts have been put forth to design new soluble π-conjugated polymers as donor material for BHJ solar cells when fullerene derivatives are primarily used as an electron acceptor, for example $PC_{61}BM$, $PC_{71}BM$.

Based on these results, a variety of other PCBM-analogous fullerene derivatives have been synthesized to improve the device efficiency through enhancing the solubility, thermal stability, and light-harvesting ability of the fullerene acceptor. Novel fullerene derivatives such as sily-methyl[60] fullerenes (SIMEFs), methano indene fullerenes (MIFs), fullerenyl esters, and lithium ion-encapsulated fullerene derivatives have been developed [32, 33].

The search for novel alternative acceptors led to the fabrication of novel fullerene derivatives, the azafullerenes, which are a class of heterofullerenes in which the element substituting for carbon is nitrogen [32].

Wudl at al reported the first bulk preparation of structurally defined azafullerenes C59N2 and RC59N [34].

While von Delius and co-workers pioneered their application to OSC devices.

In addition to $PC_{61}BM$ there are many other types of fullerenes, some examples are shown in Figure 2.3. $PC_{71}BM$, the C_{70} equivalent of $PC_{61}BM$, was synthesised but is based on C_{70}. Researchers have studied several derivative of fullerenes in order to tune the energy levels of the compounds, e.g. the LUMO level of ICBA is 0.17 eV higher compared to $PC_{61}BM$, this means that the VOC and thus the efficiency is increased when using ICBA instead of $PC_{61}BM$ in a P3HT based solar cell [31].
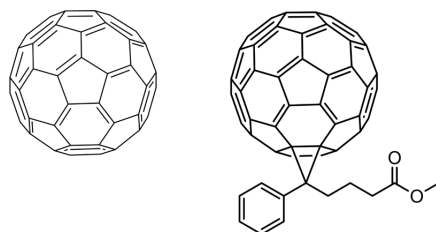
Figure 2.2 Illustrations of C_{60} and $PC_{61}BM$.

Figure 2.3: Other types of fullerene, PC71BM and indene/bis/C61/adduct (ICBA).

2.1.3   Non fullerene acceptor (NFA)-based solar cells

The dominance of fullerene derivatives in the OPV research landscape stems from advantageous properties such as (I) the ability to efficient transfer charges due to a LUMO that is delocalized over the whole surface of the molecule, (ii) high electron mobilities, (iii) multiple reversible electrochemical reductions, and (iv) the ability to aggregate in bulk heterojunctions to form both pure and mixed domains of the appropriate length scale for charge separation, that is good blend morphology with the donor material. Nevertheless, fullerene-based acceptors have some significant limitations including (I) poor absorption in the solar spectrum range, which limit their ability to harvest photocurrent and limit the performance of the device (ii) synthetic inflexibility , i.e. limited tunability in terms of spectral absorption, (iii) high synthetic cost, which limit the large-scale application of this type of acceptors. Furthermore, fullerene acceptors have (iv) morphological instability due to fullerene diffusion and aggregation in the thin film over time, resulting in device instability[35].

In the last years, much research has been focused on developing donor materials optimized specifically for these fullerene acceptors materials and thus accommodating these limitations in terms of absorption profile and electronic properties. The study and research of new donor materials using this approach has undoubtedly advanced the OPV field significantly. However, the fine-tuning of molecular and electronic properties of the electron donor to fulfil the requirements dictated by the fullerenes is a rigid design strategy. So, another approach to further improve the OPV device performance focuses on the development of new non-fullerene acceptors (NFAs) to
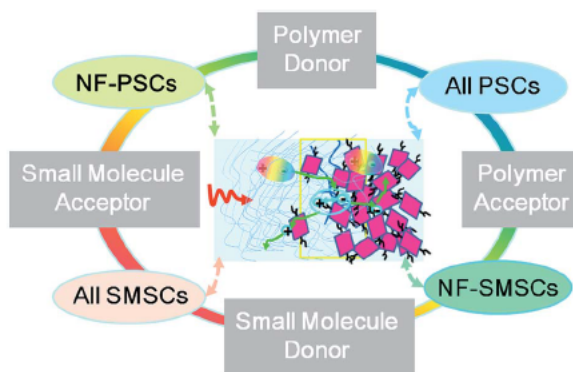
Figure 2.4 Four possible organic-donor-to-organic-acceptor combinations arising for non-fullerene solar cells: the combination of polymer donor to polymer acceptor gives rise to the so-called all polymer organic solar cells (all PSCs);52 the combination of small-molecule donor to small-molecule acceptor gives rise to the so-called all smallmolecule organic solar cells (all SMSCs) [36].
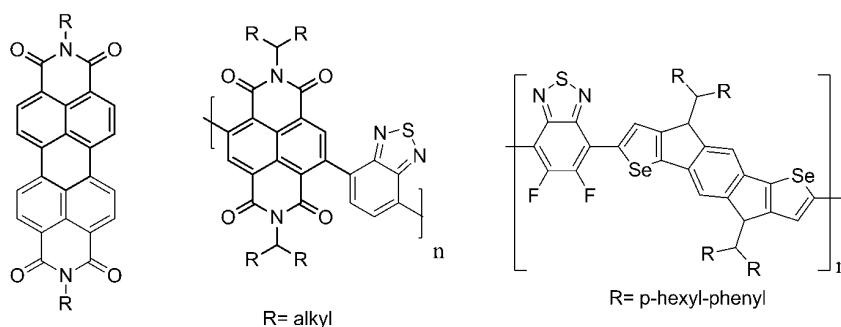
Figure 2.5 Examples of small molecules and pokymers used as acceptors.

be used in conjunction with the vast number of small molecule and polymeric donor materials that have been widely developed over the past decade. The PCEs of the non fullerene solar cells have been busted to more than 14% during the last years and this rapid increase in performance started the new development cycle in this area.

Like donor materials, of which there are polymer and small-molecule types, organic acceptor materials can also be classified into small-molecule and polymer types. There are therefore four possible donor-to-acceptor combinations, from polymer donor and acceptor as well as small-molecule donor and acceptor, giving rise to four kinds of NF-OSCs, as Figure 2.4 shows.

Polymer non-fullerene acceptors

Polymers have also been studied as acceptors in order to prepare all-polymer solar cells [19]. The advantage of the polymer acceptor is that it is easier to tune the band gap of the polymers and thus ensure efficient charge transport between the donor and acceptor in the active layer. Some examples of small molecules and polymers used as acceptors in organic solar cells can be seen in Figure 2.5.

Similarly to the small molecules, the perylene diimide based systems are widely investigated polymer acceptors. Bao, Zhao and coworkers reported 4.21% efficiency from a PDI-thiophene based polymer acceptor, P1. When using P3HT as the donor, the PDI bithiophene based polymer (P2) had a PCE of 2.17% [37].

NDI based polymers are another interesting class of polymer acceptors. NDI-2T is one of the most famous electron-transporting polymer due to its high electron mobility. The performance of all polymer OPV cells do not yet compete with those of polymer donor/molecular acceptor devices. The origin of this efficiency discrepancy has often been attributed to the lower electron mobility of most conjugated polymers compared to fullerenes and inappropriate electronic coupling between the donor/acceptor components To date, less polymeric acceptors have been synthesized when compared to the donor counterpart. However, momentum toward the development of new electron depleted building blocks is increasing due to the recent promising results in electron-transporting materials for OLED, OLETs, and OTFTs. Furthermore, the recent first certified all-polymer cell achieving PCE up to 106% indicates that there are no fundamental reasons as to why all-polymer blends cannot achieve efficiencies of fullerene-polymer devices [19].

Small molecule acceptors

In recent years, small molecule non-fullerene acceptor materials have attracted more and more attentions due to their adjustable energy level, easy synthesis, low production cost and excellent solubility. More importantly, this kind of materials have a broader absorption range in the visible solar spectrum than fullerenes and their derivatives [38].

One of the most studied small molecules NFAs are the ones based on the 2-(3-oxo-2,3-dihydroinden-1-ylidene)malononitrile (IC) electronwithdrawing group; they have been the most efficient molecular system until now 80–84 The representative molecular structures for the IC family are shown in Figure . Most of these molecules are low band gap materials with an optical band gap (E_{optg}) of 1.6 eV, and hence commonly show intense light absorption in the long wavelength range.

The most efficient molecules of this family are the ITIC, IT-M and m-ITIC which have shown efficiency of 10,7% and 11,5% respectively [39]. Latest results on an IC derivative showed a record efficiency of 13 % [40].

Other small-molecule non-fullerene acceptors which have been well investigate are molecules built around the corannulene, truxene, subphtalocyanine, perylenediimide cores or linear alternating donor/acceptor-shaped molecules.

Naphtaldiimde (NDI) acceptors have a similar structure to Perylene-diimide. They have high thermal and oxidative stability, as well as high electron affinity, and have been considered as promising fullerene alternative. Compared with PDI, NDI has a wide band gap, which is difficult to reach the visible range in spectral absorption. Therefore, relatively few studies have been applied to these molecules. However, there are some methods to extend absorption in

UNIVERSITAT ROVIRA I VIRGILI
NOVEL ELECTRON ACCEPTORS AND NEW SOLUTION PROCESSED HOLE BLOCKING LAYER FOR ORGANIC SOLAR CELLS
Caterina Stenta

26   *CHAPTER 2. ORGANIC SOLAR CELLS OVERVIEW*

to the visible range, such as extending the conjugation of NDI through the core and using electron-donating substituients [40].

Fused ring (indacenodithiophene, IDT and indacenodithieno[3,2-b]-thiophene, IDTT) have been used as electron acceptors. IDT and IDTT have large and rigid planar conjugated structures, which benefits the delocalization of π electrons and interaction between aromatic rings. Thereby high carrier transport mobility can be obtained [41]

PDI based small molecules

The optimal optoelectronic properties of the Perylene-diimide units, such as good absorption, the electron mobility, stability and chemical ease of synthesis among others, make them a potential candidate for constructing organic acceptors. However, molecular self-assembly studies on PDI derivatives have clearly demonstrated that the large planar p-system of the PDI chromophore often leads to the formation of hundreds of nanometric crystalline aggregates due to the presence of strong π- π stacking interactions [42]. These domains are too large and prevent a suitable interfacial area between the donor and acceptor material for an efficient exciton splitting. At the same time this π- π stacking tendency can be an attractive feature as it forms crystal motifs that can be suitable for charge transport and thus give the PDI a suitable transport ability. In order to avoid the formation of these large PDI domains, without decreasing the good transport ability, several functionalization design have been proposed to change the molecular structure of the PDI. From here the need to functionalize the PDI units. The functionalization consists in introducing some bridges between the PDI units via their lateral ortho or bay positions. The steric hindrance caused by the functional groups induces a change in conformation of the PDIs which is the key to avoid the formation of large aggregates in the solid state. In this thesis we have studied three differentPDIs: PDI 1, PDI 2 and PDI 3 with different linker between the PDI units.
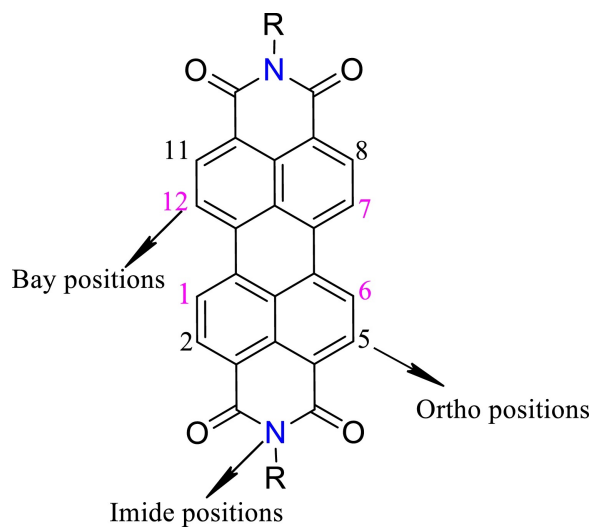
Figure 2.6 Functional positions of PDI.
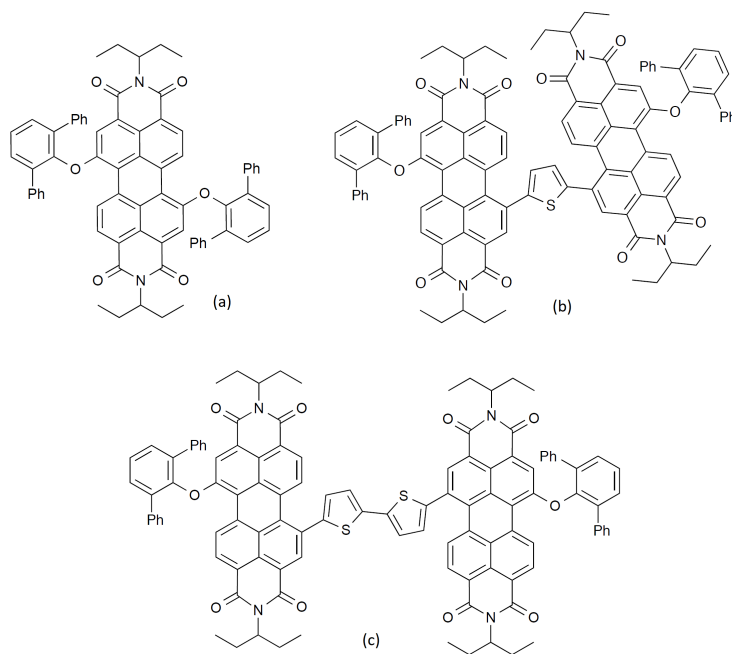
Figure 2.7 Molecular structure of (a) PDI 1, (b) PDI 2 and (c) PDI 3.

Chapter 3

The intermediate layer

It is known that the potential loss due to the energy level offset between the donor and acceptor materials in OSCs makes the electrode contacts crucial parameters to derive the net potential out of the BHJs [43].

Therefore, the formation of a good Ohmic contact at the interfaces between the active layer and electrodes for efficient charge extraction and transportation.

A significant step for the achievement of high efficiency OSCs is providing a driving force for extraction of holes and electrons to their respective electric contacts. This requires the optimization of the absorber/electrode interfaces which can be obtained either by electrode surface treatments or, as in this work, by insertion of an intermediate or buffer layer as charge-extracting or charge-blocking layers.

The intermediate layer has the function to (i) selectively transport only one type of charge, electron or hole e, while simultaneously blocking the opposite charge, decreasing in this way the probability of charge recombination.

Furthermore, intermediate layers are used (ii) to tune the energy level alignment between the active layer and an electrode. The intermediate layer can, in some cases, as well (iii) compensates for the roughness that electrodes have and that might result in shunts in the film. Another functions of the interface material are (iv) to determine the polarity of the device and (v) to prohibit a chemical or physical reaction between the polymer and electrode.

The intermediate layers materials mainly include inorganic metal oxides, polymers and small molecules, carbon-based materials, metal salts complexes, organic-inorganic hybrids/composites and other alternatives.

The most widely used electron blocking layer material has been polyethylenedioxythiophene:polystyrenesulfonate (PEDOT:PSS).

3.1 Hole blocking layers

3.1.1 Semiconducting layers: Metal Oxides

Metal oxides can be p-type and n-type, depending on the position of the valence band and conduction band. n-type like transition metal oxides have been successfully introduced in OPV as hole blocking layer.

OSCs based on metal oxide intermediate layers exhibit high performance which can be attributed to the fact that the metal oxide layers have salient features of ambient stability, good solution processability, high optical transparency and excellent capability to extract/transport electron carriers. To date, effective materials for OSCs include binary oxides (such as ZnO_x, TiO_x, Nb_2O_5, and SnO_x) [44], and newly emerged ternary oxides (such as Al-doped ZnO, Mg-doped ZnO, and Cs-doped metal oxides) [45].

These materials are transparent in the visible light spectrum but absorb ultraviolet (UV) light. The layer thickness of the interfacial layer is tuneable without absorption losses in the visible (VIS) light and thus can additionally act as optical spacer [46].

The design of 3-dimensional structures of metal oxides is another approach to improve the PCE and many groups compare 2-dimensional ZnO layers with 3-dimensional nanostructures [47]. The increased interface acceptor/interfacial layer improves the electron transport and is expected to allow for thicker active layers.

Mor at al. presented a vertically oriented TiO2 nanotube film with P3HT:PCBM infiltrated into the nanotubes [48].

Zinc Oxide

As an inorganic n-type semiconductor, ZnO is one of the most used choices in metal oxide intermediate layers materials due to its features such as low cost, easy synthesis, non-toxicity, high stability, and unique optical/electronic properties [49].

Titatium oxide

Titanium oxide (TiO_2 or TiO_x) is another n-type metal oxide used as intermediate layer material because it has good optical transparency, relatively high electron mobility, and environmental stability.

By solution processing from a sol–gel precursor or from TiO_x nanoparticles (NPs), TiO_x films were fabricated as effective intermediate layers for both conventional and inverted OSCs [50]. When incorporated into conventional OSCs, titanium oxide can serve as an optical spacer to redistribute the light intensity within the active layer to enhance light absorption, and can act as an electron-transporting/hole-blocking layer to improve charge collection [51].

As a result, the conventional PCDTBT:PC_{71}BM-based device using the sol–gel TiO_x intermediate layers showed increased PCE of 6.1% with an internal quantum efficiency approaching 100% [46].

Niobium Oxide

Similar to ZnO and TiO$_x$, wide-bandgap niobium oxide (Nb$_2$O$_5$ or NbO$_x$) materials have high transparency at visible wavelengths and inherently n-type characteristics. Thereby they can act as electron-transporting layers for OSCs [52].

Tin Oxide

Tin oxide (SnO$_2$ or SnO$_x$) is another promising wide-bandgap metal oxide. The higher intrinsic mobility of tin oxide compared to other n-type oxides, offers its advantages in the efficient carrier transport. Recently, solution-processed SnO$_x$ films and SnO$_2$ NPs were developed as CILs for inverted OSCs [53].

Ternary Metal Oxides

Using n-type doping in binary oxides, a series of ternary metal oxide electron-transporting materials were developed as intermediate layers [54]. When they served as intermediate layers in inverted OSCs, improved PCEs and device stability were demonstrated, providing a very promising strategy to develop high performance OSCs toward practical utilization. Recently, bandgap tunable Zn$_1$–xMg$_x$O (ZMO) metal oxides were proposed by Yin et al. as a novel class of CILs for enhancing efficiency and stability of OSCs [54]. By Mg doping in ZnO, solution-processed ZMO intermediate layers showed tuneable bandgaps, WFs and energy levels depending on the amount of Mg doping, thereby enabling to tune their transmittance, charge-collection, and interfacial properties for a better device performance.

Semiconducting layers: Polymers and Small-Molecules

In recent years, to avoid thermal annealing of interlayers and improve their compatibility with organic active layer, solution-processable polymers and small-molecules are often used as interface materials for improving solar cell performance. The structures of organic molecules can be easily modified towards suitable energy levels and optical/electronic properties. Owing to the intermolecular dipole moment and the ability to form self-assembled monolayers, organic intermediate layers can induce an interface dipole pointing from the cathode to the active layer, thereby effectively reducing the WF of cathodes and increasing the built-in potential of OSCs [54]. The progress of polymer CILs for both conventional and inverted OSCs has been discussed in a recent review [55].

Water/alcohol soluble conjugated polymers are effective intermediate layers for OSC applications.

Due to their ambient solution processability, several water/alcohol soluble conjugated polymers were designed as intermediate layers for efficient electron injection/transport in OSCs. A representative example is poly[(9,9-bis(3′-(N,N-dimethylamino)propyl)-2,7-fluorene)-alt-2,7-(9,9-dioctylfluorene)] PFN, shown in Figure 3.1
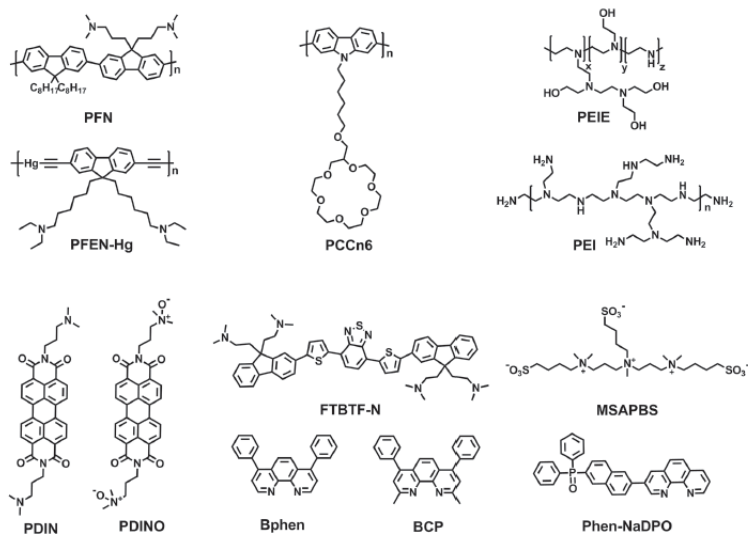
Figure 3.1: Molecular structures of some representative polymers and small molecules for intermediate layers.

In addition to the polymeric intermediate layers, small-molecule layers can also be used for OPV applications due to their attractive characteristics such as well-defined chemical structures and ease synthesis with high purity.

Thermally deposited or water/alcohol-processable small-molecules, such as bathocuproine (BCP in Figure 3.1), bathophenanthroline (Bphen in Figure 3.1), pyridinium salt-based molecules, triazine- and pyridinium-based small molecules, zwitterions, amino acids or peptides, and self-assembled ionic liquid, have been reported as effective intermediate layers for OSCs.

BPhen and BCP are good electron transport layers and good hole blocking layer.

In this thesis we investigated the use of Bathocuproine, a low cost organic molecule, as a hole-blocking layer deposited from solution processing on top of the PTB7:PCBM active layer.

Despite the fact that BCP has mostly been used in vacuum processed devices, we found that is very well suited for solution processing. Contrary to vacuum deposition, where extremely high purity sublimed materials are needed, in the solution processing a simple recrystallization is required.

In small molecule OPVs, which are comprised of a multilayers structure, it is well known that the insertion of an exciton blocking layer having a large band gap improves the PCE significantly by conveying the excitons to the interface of a donor and an acceptor.

The requirements for efficient exciton blocking layer are (i) a larger band gap than the photoactive layer which blocks the excitons but does not dissociate them, and (ii) no charge injection barrier from a photoactive layer to an exciton blocking layer.

Conducting layers: Metals

Besides the mostly used metal oxides and organic materials for intermediate layers, metals have also been developed as electron-transport materials for OSCs.

Metals can be thermally evaporated in optical thick and thin layers to form a non-transparent or transparent electrode or/and interfacial layer [56].

A combination of a low work function metal such as Ca, Mg, Ba with Ag or Al is a common way to decrease the work function of cathodes to make ohmic contacts with fullerene for efficient electron extraction and to prevent Ag and Al atoms from diffusing into the polymeric layer [57].

Salts

Solution-processable metal salts are another prominent approach to improve the device performance of OPV and broaden the available choices of intermediate layer materials. The incorporation of metal salt CILs in OSCs can improve the wettability between the electrode and the hydrophobic organic mactive layer surface, resulting in better interfacial contacts and reduced contact resistances [58].

Among the salts Cs_2CO_3 has drawn considerable attentions due to its capability of dissolving in highly polar solvent. Cs_2CO_3 has excellent electron transport properties, but suffers from poor hole blocking properties. LiF is another commonly used in OPV which can significantly enhance the energy-level alignment and stability of the cathode interface. Other versatile metal salts such as alkali carbonates (e.g., Li_2CO_3, Na_2CO_3, etc.) cesium acetate, cesium or sodium halides (i.e., CsI, CsCl, CsF, NaI), cesium stearate (CsSt), and disodium edentate have been designed as intermediate layers for OPV applications [59]. These materials exhibited facile solution processability and low WFs, which favor the formation of interfacial dipoles between the active layer and electrode, and increase charge collection [60].

Additionally, several classes of metal complexes, including copper chelates [61], such as zinc chelates [62], titanium chelates and zirconium chelates [63] were used to improve the efficiency and/or stability of OSCs.

Carbon-based materials

Carbonaceous materials are a promising class of candidates for intermediate layers materials due to their high conductivity, good structural stability and tuneable functionality. To date, fullerene, carbon nanotube and graphene as well as their derivatives have been developed as effective CIL components [64].

Graphene and its derivatives have a unique 2D structure, high transparency, and their WFs can be tuned through simple chemical modifications [28].Solution-processed graphene quantum dots were adopted as intermediate layer to facilitate charge transfer and reduce charge recombination in inverted OSCs due to their low WFs and unique optical/electronic properties [65].

Inorganic-organic hybrids and composites

Combining inorganic, organic and other useful components the hybrid/composite electron-transporting layer materials can be fabricated and they are excellent candidates to engineer the interfaces of OSCs because they combine merits of both inorganic and organic parts. There is a growing interest to develop these hybrid/composite interface materials toward OSCs with high efficiency and good stability [67].

Among various hybrid/composite intermediate layers materials, organic/inorganic materials are a major family of electron-transporting materials for OSCs applications. Lots of organic materials such as polymers and small-molecules can be used to dope inorganic metal oxides or other inorganic compounds.

Chapter 4

Organic solar cells fabrication and characterization

4.1 Solar cells preparation

4.1.1 Substrate cleaning

Prepatterned Indium Tin Oxide (ITO) on sodalime glass substrates with nominal sheet resistance of 5 and 15 Ohm/square (purchased from PSiOTec, Ltd., UK) were first rinsed with acetone to remove the residual photoresist layer. The substrates were then placed in a teflon holder and sequentially sonicated in acetone, methanol and isopropanol for 10 minutes and finally dried under flow of Nitrogen. The ITO substrates where ozone-treated in a UV-ozone cleaner for 30 min in ambient atmosphere to eliminate organic residues.

4.1.2 General remarks on experimental data

Poly-(Ethylene dioxythiophene) doped with Poly-(styrene sulphonic acid) (PEDOT:PSS), PTB7 (Mw: 22900 g mol-1) and PC71BM (Mw: 1030.99 g mol-1) were purchased from One-material and Solenne, respectively. DPP(TBfu)$_2$ was purchased from Lumtech and further purified by column chromatography, using a reported procedure. BCP (96%) was purchased from Aldrich and further recrystallized from boiling toluene, and sublimed twice. All solvents and additives were purchased Sigma–Aldrich and used without further purification. High-purity (99.99%) silver (Ag) wires were obtained from Testbourne Ltd., and high-purity calcium (Ca) pellets (99.5%) was purchased from Sigma-Aldrich. High purity (HPLC gradient grade, 99.9 %) CHCl$_3$ was used for the active layer deposition. The solvent was dried with activated molecular sieves and kept in a sealed bottle with silver foil prior to use.

BCP purification:

BCP was placed in round bottom flask mounted with a reflux condenser. A minimum amount

35

of toluene was added and the mixture was brought to reflux (110°C). Toluene was further added dropwise, slowly enough to maintain the reflux, until all the BCP had dissolved. At this point the reflux condenser was removed, the flask was stoppered and left to cool down to room temperature undisturbed over night. The resulting light yellow solid was filtered and dried under high vacuum overnight, after which time it was used directly for the deposition of BCP layers. A a batch of the recrystallized BCP was sublimed twice in a row in a sublimation tube (DSU-20, Creaphys, GmbH). The purest fraction of the first sublimation step was resublimed in the same conditions as the first step (5×10^{-7} mBar, 120-150ºC).

4.1.3   Device preparation

The ITO substrates were coated in air with a layer of filtered (0.45 µm, cellulose acetate) solution of Poly(3,4-ethylenedioxythiophene) : poly(styrenesulfonate) (PEDOT:PSS, HC Starck Baytron P).

PEDOT:PSS (30-40 nm thickness) was spin coated onto the ITO surface at 4500 rpm 30 seconds followed by 3500 rpm 30 seconds. The PEDOT:PSS films were dried at 120 ºC under inert atmosphere for 15 min and transferred into a nitrogen-filled glove box ($<$ 0.1 ppm O_2 and H_2O).

In the case of the BCP solar cells, the blend solution of PTB7 and $PC_{71}BM$ (1:1.5, w/w) was prepared in CB : DIO (3% w/w) and stirred for 24 h at 40°C in an inert atmosphere glove box. The total concentration of solids was 25 mg/ml. The blend solution was left to cool down to room temperature and stirred for a further 48 h, after which the active layers were spin-coated over the PEDOT:PSS layer.

For the PDI solar cells the blend layers were spin coated at 1900 to 2600 rpm from a 25 or 15 mg/ml (total concentration) solution of the PTB7 and the PDI electron donor.

For the BCP, the PTB7:$PC_{71}BM$ active layers (ca.100 nm thick) were deposited by spin coating at 800 rpm for 30 s on the ITO/PEDOT:PSS substrate without further treatments.
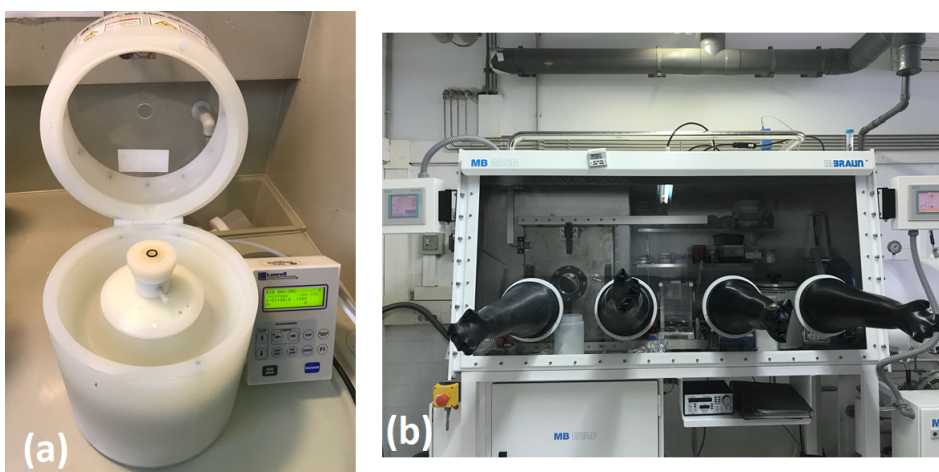
Figure 4.1 Pictures of (a) the Spin coating used for PEDOT:PSS and active layer deposition and (b) the inert atmosphere Glove box used for device fabrication.
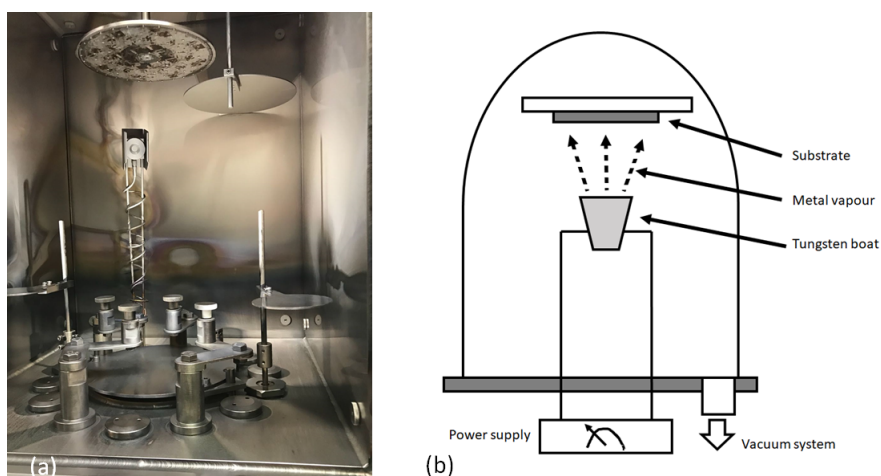
Figure 4.2 (a) Pictures and (b) scheme of the evaporator chamber used to deposit the metal contacts.

The BCP spin coating solution was prepared from a stock solution of BCP (5mg/mL) in toluene/methanol (1:9) and was left under stirring at 50ºC in an inert atmosphere glove box over night. The solution was subsequently diluted 10 folds in pure methanol and used straight after. Solution processed BCP was deposited at 4000 rpm for 1 min. Thermally evaporated BCP (5 nm; 0.2 A/s) was thermally evaporated under high vacuum of 1×10^{-6} mbar.

Subsequently the samples were transferred into a ultra high vacuum chamber ($1 \cdot 10^{-6}$ mbar) located in the same glovebox, for the thermal evaporation of the cathode.

A 20 nm Ca layer and an 100 nm Ag layer were deposited in sequence under the vacuum of $1 \cdot 10^{-6}$ mbar. Metals were evaporated through a shadow mask leading to devices with an area of 9 mm^2 at a rate of 0.1 Å/s and 0.5-1 Å/s, respectively.

Following fabrication, the films were maintained under a Nitrogen atmosphere and stored in the dark until used.
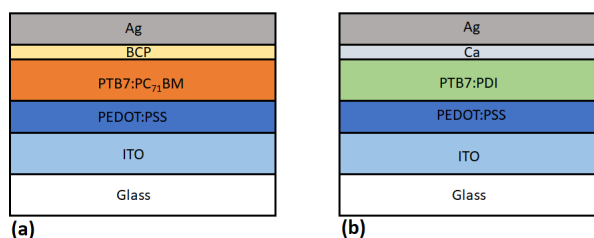
Figure 4.3 Schematical representation of the solar cells with (a) the solution processed BCP layer and (b) the PDI acceptor.
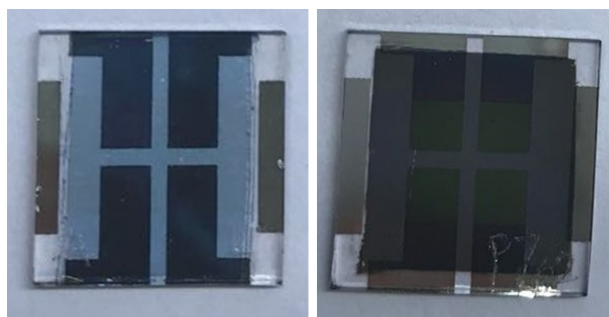
Figure 4.4 Pictures of the solar cell samples.

4.2 Materials characterization

4.2.1 Atomic force microscopy

Atomic force microscopy (AFM) topographic and phase images of the sample were performed in the acoustic mode using Agilent 5500 SPM. Samples were measured on ambient conditions using Budget Sensors s with a typical force constant of 1−7 nN/m and at resonant frequency of 75 kHz.

4.2.2 X-Ray diffraction

Conventional XRD measurements on thin films were carried out on a Bruker-AXS D8-Discover diffractometer with parallel incident beam (Göbel mirror), a vertical theta-theta goniometer, a XYZ motorized stage mounted on an Eulerian cradle, an incident and diffracted beam Soller slits, a 0.02^o receiving slit and a scintillation counter as a detector. Diffraction pattern were recorded over an angular 2theta range of 1° to 15°. The data were collected with an angular step of 0.05^o at 10 sec per step. Cuk$_\alpha$ radiation was obtained from a copper X-ray tube operated at 40 kV and 40 mA.

2D XRD measurements were performed with the same diffractometer equipped with an HI-STAR area detector (multiwire proportional counter of 30x30 cm with 1024x1024 pixel) and GADDS software (General Area Diffraction System). Samples were placed directly on the sample holder and the area of interest was selected with the aid of a video-laser focusing system. An X-ray collimator system allows to analyze areas of 500 µm wide. 2D XRD patterns (one

frame) were collected covering 1.2-22.3º 2ϑ from at a distance of 15 cm from the sample. The exposition time was 600 sec per frame.

4.2.3   Differential pulse voltammetry

DPV measurements were performed for the PDI in a conventional three-electrode cell using a µ-AUTOLAB type III potentiostat/galvanostat at 298 K, over $CHCl_3$ and deaerated sample solutions (~0.5 mM), containing 0.10 M tetrabutylammonium hexafluorophosphate (TBAPF6) as supporting electrolyte. A carbon working electrode, $Ag/AgNO_3$ reference electrode and a platinum wire counter electrode were employed. Ferrocene/ferrocenium couple was used as an internal standard for all measurements.

4.3   Solar cells characterization

4.3.1   Hole and electron mobilities

Mobility measurements were performed on hole-only and electron-only devices using the Mott-Gurney equation from the J-V characteristics measured in the dark. Mobility values were obtained by fitting the J-V plots in the SCLC region to a Mott-Gurney equation (1) with the static permittivity of the active layer (ε) fixed to 3, µ0 being the zero-field mobility.

$$J = \frac{9}{8}(\varepsilon\mu_0)/L^3 x V^2$$

Eq. 2.2

Mobility measurements were repeated at least three times (using different devices) to confirm the reproducibility of the results.

4.3.2   Current density-voltage characteristics

The J-V characteristics of the devices were measured in the dark and under AM 1.5G conditions using a Sun 2000 solar simulator (150 W, ABET Technologies model 11000 class type A, Xenon arc.).

The applied potential and cell current were recorded using a Keithley 2400 digital source meter. A home built Labview© interface was used to control the source meter and record the J-V curves. The solar radiation standard conditions or 1 Sun conditions (AM 1.5 G, 1000 W/m^2) were obtained uing a calibrated silicon diode (NREL) and lower light conditions were simulated using appropriate filters. All devices were measured in a sealed holder using a N_2 atmosphere.
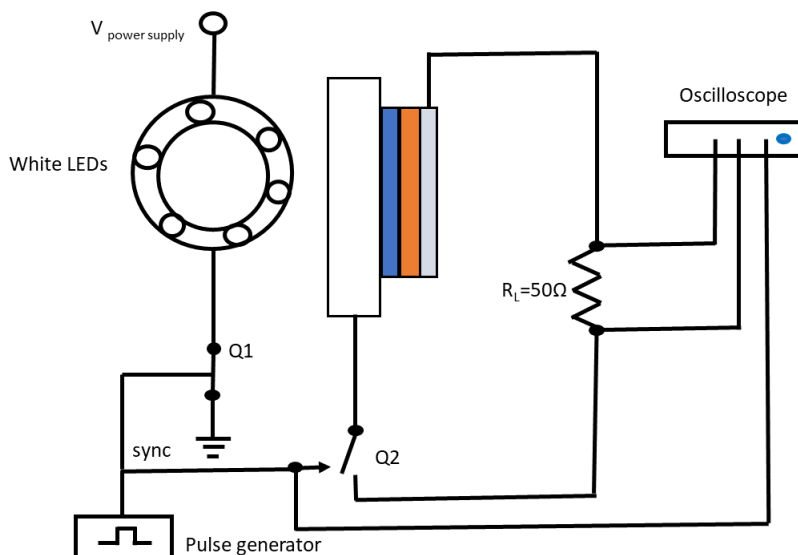
Figure 4.5: Schematic diagram of the CE setup.

4.3.3   External Quantum Efficiency

The External Quantum Efficiency (EQE) was measured using a home built system consisting of a 150 W Oriel Xenon lamp, connected to a motorized Spectral Products cm100 monochromator (CM100) and a Keithley 2400 digital source meter to record the current at each specific wavelength. The photocurrent and irradiated light intensity were measured simultaneously and processed with a home built Labview© software.

4.3.4   Charge extraction

In this work we used Charge extraction (CE) measurements to estimate the average charge density within the active layer under open circuit conditions using a home built system. Devices were held at open circuit by applying bias from a focused array of LEDs. Once the device reached steady state it was then short-circuited with the LEDs switched off simultaneously (switch-off time / relay = 300 ns), leaving the charge stored in the active layer to decay through a small 50 Ω resistor.

A Yokogawa 2052 digital oscilloscope was used to record the voltage decay across the resistor. Using Ohm's law the voltage transient could be turned into a current transient, which was subsequently integrated to calculate the total charge in the active layer at each light applied bias. In general the device is measured from open circuit voltage values corresponding to >1 Sun conditions to 0 V.

Figure 4.6 Schematic diagram of the TPV setup.

4.3.5 Transient Photovoltage

Transient photovoltage (TPV) measurements were carried out on working devices through applying a light bias (the same ring of LEDs used in CE) and holding the device at steady state in open circuit conditions. Once the device reached steady state conditions, a low-intensity laser pulse (PTI GL-3300 Nitrogen Laser) irradiated the sample to allow a small excess number of charge carriers to be generated. As the device is being held at open-circuit, the excess charge generated has no choice but to recombine. The transient decay of the charge carriers is recorded using a Yokogawa 2052 digital oscilloscope. Sweeping from high-applied bias (high illumination) to low-applied bias (low illumination) allows a correlation between charge carrier lifetime and voltage to be made. The irradiation wavelength was chosen to be close to but not at the maximum of the donor absorption spectrum. . A graded neutral density filter was used to control the intensity of the small perturbation, so that the approximation $\Delta n << n$ is held (usually keeping the value between 5 and 10 mV).

Chapter 5

Conclusions

This thesis presents an investigation of different types of bulkheterojunction organic solar cells.

We optimized the fabrication processes and studied their device mechanism through different characterization procedures.

In particular, two different types of organic solar cells have been fabricated and characterized: A novel type of solar cell with a non fullerene acceptor material from the Perylene-diimide family and one with a new solution processed hole blocking layer to replace the vacuum-processed calcium, the Bathocuproine.

In the work of the PDI, three new perylenediimide, PDI1, PDI2, PDI3 have been prepared and applied as electron acceptors instead of $PC_{70}BM$ to produce solution-processed bulk heterojunction solar cells.

We reported on a library PDI molecules substituted at bay position with diphenylphenoxy groups. It has been shown that the perpendicular arrangement of the diphenylphenoxy group with respect to the perylene core impedes intermolecular - stacking between the conjugated cores and effectively reduce the aggregation of the perylene derivatives in solution and leads to completely amorphous active layers.

We then synthesized and characterised two new PDI dimers bridged through the bay position with one and two thiophene units.

The new PDI were used to fabricate bulk-heterojunction solar cells.

We optimized the fabrication procedure, studying the donor-acceptor ratio, the annealing type and additive content and studied the impact of the PDI on the device performance via optical and electronical studies. To assess the impact of the PDIs in avoiding the formation of over-sized crystalline domains we conducted a morphological study using X-Ray diffraction and AFM microscopy techniques and link the morphology data with the photophysical properties of the devices, we carried out electron mobility measurements on hole-only and electron-only devices fabricated under identical conditions as in OSC devices.

In order to understand how the non-geminate recombination contributes to V_{OC}, a qualitative recombination study was carried out using a well-established charge extraction (CE) and

transient photovoltage (TPV) method and we found out that non-geminate recombination plays a major role in determining the V_{OC} of the devices.

We found out that the PDI-based devices exhibit a significantly higher V_{OC} than PCBM-based devices.

In the work regarding the solution processed bathocuproine we replaced the conventional calcium hole-blocking layer by a solution processed bathocuproine (BCP).

To best best demonstrate the applicability of BCP to solution processing methods, we based the study on state of the art polymer-based OSCs, and devices with active layers composed $PTB7/PC_{71}BM$ have been fabricated.

The devices comprising solution processed BCP as the hole-blocking layer were compared to devices where the BCP layer was thermally evaporated and with reference devices comprising a standard Ca/Ag cathode.

We optimized the fabrication processes studying different fabrication parameters, particularly the concentration parameters and annealing processes. Contrary to vacuum-processed devices, where extremely pure BCP (doubly or triply sublimed) is usually necessary, in our case lower purity BCP has been used and showed similar performance than e-BCP-based devices.

We have characterized the solar cells via J-V characteristics. The EQE (External Quantum Efficiency) was measured as well using a home made set up.

We demonstrated how the BCP-processed devices show superior stability than their respective reference devices in all aspects of their characteristics and how devices comprising a thin layer of BCP as hole blocking layer led to similar performance than standard devices made from either vacuum-processed calcium or evaporated BCP and furthemore they showed much higher stability in air than calcium based or thermally evaporated BCP devices.

While extremely pure BCP is usually necessary for vacuum-processed devices, for our solution-processed devices, lower purity BCP showed to lead to similar performance than evaporated BCP-based devices.

We showed with this work how BCP can be a very economical alternative to the commonly vacuum-processed hole blocking materials in OPV.

Chapter 6

Appendices

Appendix 1

Reproduction of the article

"Solution Processed Bathocuproine for Organic Solar Cells"

Caterina Stenta, María Pilar Montero-Rama, Aurelien Viterisi, Werther Cambarau, Emilio Palomares, Lluis F. Marsal

Solution Processed Bathocuproine for Organic Solar Cells

Caterina Stenta, María Pilar Montero-Rama, Aurelien Viterisi, Werther Cambarau,
Emilio Palomares, and Lluis F. Marsal 🔘 *, Senior Member, IEEE*

Abstract—PTB7/PC$_{71}$BM bulk heterojunction solar cell devices where the conventional calcium hole-blocking layer has been replaced by a solution processed bathocuproine (BCP) layer is described. The BCP thin film was deposited *via* spin coating from a dilute solution of BCP in a mixture of toluene and methanol directly on the top of the active layer. The silver cathode was subsequently deposited *via* thermal evaporation. The study shows that solar cells devices comprising solution-processed BCP show similar performance than devices made from either calcium or evaporated BCP. Moreover, the devices made from solution-processed BCP show superior stability in air than calcium and evaporated BCP-based devices. This is to the best of our knowledge, the first report of the use of solution processed BCP in organic solar cells.

Index Terms—Photovoltaics, polymer solar cells, small molecule solar cells, bulk heterojuntion, bathocuproine.

I. INTRODUCTION

THE advent of organic solar cells has brought great hopes for the future of electrical energy generation. With laboratory power conversion efficiency (PCE) now exceeding 10 % either in polymer-based or small molecule-based bulkheterojunction solar cells, or multiple junction *vacuum* processed solar cells, [1]–[4] the technology is deemed mature for the manufacture of commercial products. Indeed, numerous companies (BeElectric, Heliatek, PVinfinity) have invested considerably in manufacturing plants (*vacuum* processing, roll to roll), and prototypes are now available on the market. However, the recent stark decrease in the market price of monocrystalline and polycrystalline Silicon-based solar cells (typically below 1 \$/watt) [5] imposes a tremendous financial pressure on these new technologies. Indeed, given that the efficiency of organic solar cells in modules is still well below that of commercial silicon-based solar panels (6–8 % PCE for organic solar cell modules of 100 cm^2 compared to up to 19 % for state of the art Si-Monocrystalline solar panels of 1.5 m^2) [6] to be competitive with the Silicon technology, the price of OSCs will need to drop well below 1 \$/watt. [7], [8] This objective will require on one hand the use of low-cost light absorbing materials and on the other hand the possibility to manufacture with the highest possible turn over yields. As such, Roll-to-Roll solution processing is the method of choice as it allows for extremely fast deposition rates, however it imposes very stringent requirements on the materials to be deposited. Indeed, since the films are deposited successively from materials in solution, it is imperative that each material is deposited from a solvent orthogonal to the layer it is deposited onto. [9], [10] While this requisite has been met for the electron blocking layer (PEDOT:PSS deposited from aqueous solution) and the absorber layer (deposited from an apolar organic solvent), the hole blocking layer–most often water sensitive metals such as Ca, or Metal oxides– is virtually always deposited from *vacuum* deposition methods in the laboratory.

With these requisites in mind, we investigated the use of bathocuproine (BCP), a low cost organic molecule, as a hole-blocking layer deposited from solution processing on polymer-based organic solar cells. Although several phenantroline derivatives are available for PV applications [26], [27], BCP has been the most commonly used derivative in organic solar cells. Until recently, BCP had only been used in *vacuum*-processed devices, apart from a recent report in which it was deposited from an ethanol solution on top of a lead-halide perovskite film. [22] In the study herein, we found that BCP is very well suited for solution-processing on organic solar cell devices' active layers. Contrary to *vacuum* deposition, where extremely high purity materials are needed, obtained *via* low-yielding sublimation, a simple recrystallization is required (from commercially available 96 % pure BCP). The devices fabricated with BCP were compared with state of the art polymer BHJ devices, and were found to lead to similar performance than respective reference devices, as well as higher stability towards humidity and oxygen.

This is the first example, to the best of our knowledge, where BCP was used *via* wet deposition methods in organic solar cell devices. The ease of fabrication, associated with the lower cost of the material, with respect to conventional *vacuum* deposition methods, will certainly grant it widespread application in industrial processes.

C. Stenta, M. P. Montero-Rama, A. Viterisi, and L. F. Marsal are with the Departament d'Enginyeria Electrònica, Elèctrica i Automàtica, Universitat Rovira i Virgili, Tarragona 43007, Spain (e-mail: caterina.stenta@urv.cat; mariadelpilar.montero@urv.cat; aurelien.viterisi@urv.cat; lluis.marsal@urv.cat).

W. Cabarau and E. Palomares are with the Institut Català d'Investigació Química, Tarragona 43007, Spain (e-mail: wcambarau@ICIQ.ES; epalomares @iciq.es).

Color versions of one or more of the figures in this paper are available online at http://ieeexplore.ieee.org.

II. Experimental

Materials and solution preparation: indium tin oxide (ITO) coated glass substrates (with nominal sheet resistance of 15 Ohm/square and 120 nm of thickness) were purchased from PsiOTec Ltd. Poly-(Ethylene dioxythiophene) doped with Poly-(styrene sulphonic acid) (PEDOT:PSS), PTB7 (Mw: 22900 g mol^{-1}) and PC$_{71}$BM (Mw: 1030.99 g mol^{-1}) were purchased from One-material and Solenne, respectively. DPP(TBfu)$_2$ was purchased from Lumtech and further purified by column chromatography, using a reported procedure. BCP (96 %) was purchased from Aldrich and further recrystallized from boiling toluene, and sublimed twice (see below). All solvents and additives were purchased Sigma–Aldrich and used without further purification. High-purity (99.99 %) silver (Ag) wires were obtained from Testbourne Ltd., and high-purity calcium (Ca) pellets (99.5 %) was purchased from Sigma-Aldrich.

The blend solution of PTB7 and PC$_{71}$BM (1:1.5 w/w) was prepared in CB:DIO (3 % w/w) and stirred for 24 h at 40 °C in an inert atmosphere glove box. The total concentration of solids was 25 mg/ml. The blend solution was left to cool down to room temperature and stirred for a further 48 h. [11], [12].

Purification of BCP: BCP was placed in round bottom flask mounted with a reflux condenser. A minimum amount of toluene was added and the mixture was brought to reflux (110 °C). Toluene is further added dropwise, slowly enough to maintain the reflux, until all the BCP had dissolved. At this point the reflux condenser was removed, the flask was stoppered and left to cool down to room temperature undisturbed over night. The resulting light yellow solid was filtered and dried under high *vacuum* overnight, after which time it was used directly for the deposition of sp-BCP.

For e-BCP a batch of the recrystallized BCP was sublimed twice in a row in a sublimation tube (DSU-20, Creaphys, GmbH). The purest fraction of the first sublimation step was resublimed in the same conditions as the first step (5 × 10^{-7} mBar, 120–150 °C).

Preparation of solar cells: The ITO substrate were cleaned by ultrasonication in detergent, water, acetone and isopropyl alcohol and subsequently dried in a stream of Nitrogen. PEDOT:PSS (30–40 nm thickness) was spin-coated on top of the pre-treated ITO surface (ultraviolet-ozone for 15 min in ambient conditions) and subsequently annealed at 120 °C for 20 min in an inert atmosphere glove box (<0.1 ppm O$_2$ and H$_2$O). PTB7:PC$_{71}$BM active layers (ca.100 nm thick) were deposited by spin coating at 800 rpm for 30 s on the ITO/PEDOT:PSS substrate without further treatments. The BCP spin coating solution was prepared as follows: a stock solution of BCP (5 mg/mL) in toluene/methanol (1:9) was left under stirring at 50 °C in an inert atmosphere glove box over night. The solution was subsequently diluted 10 folds in pure methanol and used straight after. Sp-BCP was deposited at 4000 rpm for 1 min. e-BCP (5 nm; 0.2 A/s) was thermally evaporated under high *vacuum* of 1 × 10^{-6} mbar. The Ca layer (20 nm; 0.3 A/s) and an Ag layer (100 nm; 1 A/s) were deposited in sequence under high *vacuum* of 1 × 10^{-6} mbar. The effective area of the device was 0.09 cm^2.
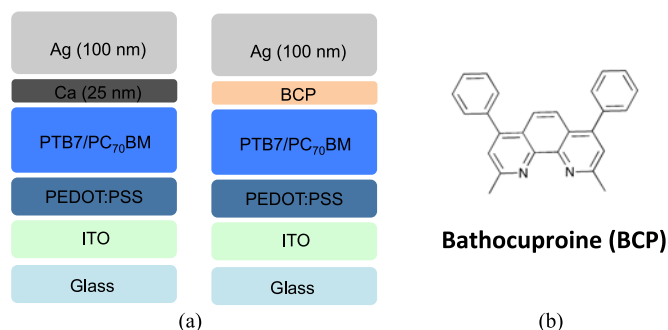
Fig. 1.   (a) Structure of the reference and BCP-based solar cell devices (b) Chemical structure of BCP.

Solar cells characterization: The *J-V* characteristics of the devices were recorded using a Sun 2000 Solar Simulator (150 W, ABET Technologies). The illumination intensity was measured to be 100 mW/cm^2 with a calibrated silicon photodiode (NREL). The appropriate filters were utilised to faithfully simulate the AM 1.5 G spectrum. The applied potential and cell current were measured with a Keithley 2400 digital source meter. The current to voltage characteristics (*J-V* curve) were plotted automatically with a home-built Labview software. The EQE (External Quantum Efficiency) was measured using a home made set up consisting of a 150 W Oriel Xenon lamp, a motorized monochromator and a Keithley 2400 digital source meter. The photocurrent and irradiated light intensity were measured simultaneously and processed with a home-built Labview software.

III. Results and Discussion

To best demonstrate the applicability of BCP to solution processing methods, we based our study on state of the art polymer-based OSCs. As such, devices with active layers composed of a PTB7/PC$_{71}$BM blend have been chosen, since they have led to record efficiencies in the field. The devices comprising solution processed BCP (sp–BCP) as the hole-blocking layer were compared with devices where the BCP layer was thermally evaporated (e–BCP) and with reference devices comprising a standard Ca/Ag cathode (Fig. 1). The structure of the reference devices was identical to previous reports, and the structure of the BCP-based devices only differs from the reference by their hole-blocking layer.

Interestingly, although extremely pure BCP (doubly or triply sublimed) is usually necessary for *vacuum*-processed devices, [17]–[21] for our solution-processed devices, lower purity BCP showed to lead to similar performance than e-BCP-based devices. BCP with a purity of 96 % was purchased from commercial sources and simply recrystallized from boiling toluene, and dried under high *vacuum* prior to deposition (see experimental section). The BCP layer was deposited on top of the active layer *via* spin coating, in an inert atmosphere glove box, from a solution of toluene/methanol (0.5 mg/mL conc.). The concentration of BCP was finely tuned in order to produce BCP thin films with the optimum properties. The concentration leading to the
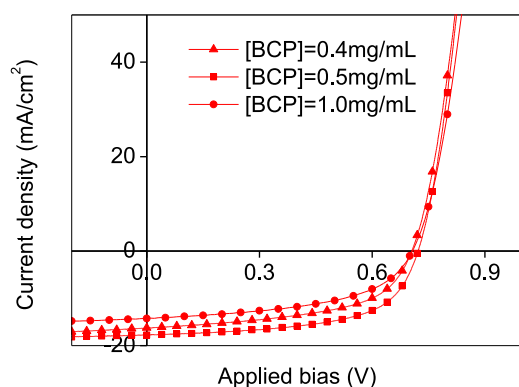
Fig. 2.   *J-V* characteristics of devices with BCP layer deposited from different concentration solutions.
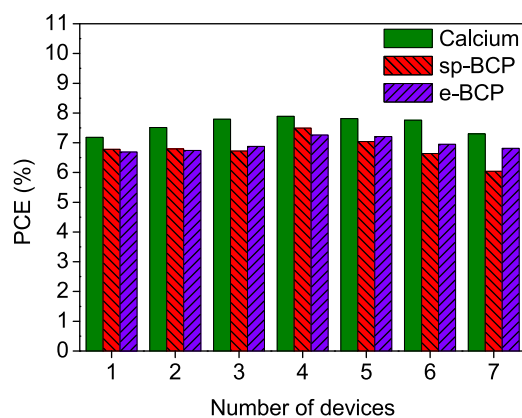
Fig. 3.   Histogram of the PCE given by a statistically relevant batch of solar cell devices made with Ca, sp-BCP and e-BCP buffer layers. Average PCE: Ca: 7.6%; sp-BCP: 6.8%; e-BCP: 6.9%.
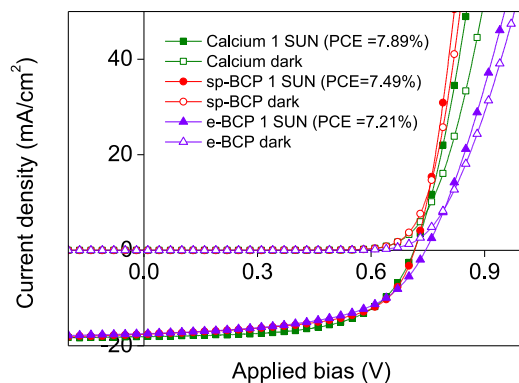
Fig. 4.   *J-V* characteristics of best-performing reference and BCP-based solar cell devices.

best performing devices was found to be 0.5 mg/mL as seen in Fig. 2.

The devices made from the optimum BCP concentration show very similar performance to either the devices made from e-BCP or to the reference devices. Fig. 3 depicts the efficiency of statistically relevant devices made from each type of buffer layer. The plot clearly shows a trend where Ca-based devices lead to slightly higher PCE than those made from either sp-BCP or e-BCP. However, the difference in PCE is on average not superior to 10 %.
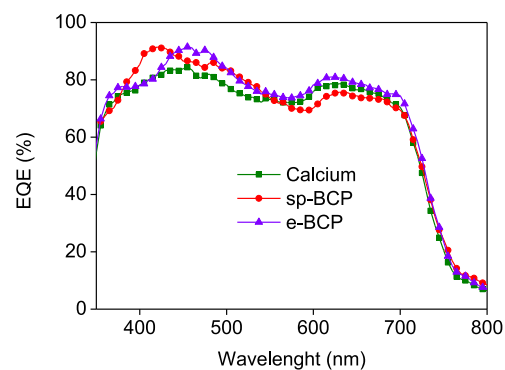
Fig. 5.   EQE spectra of Ca-based reference device and sp-BCP and e-BCP-based devices.
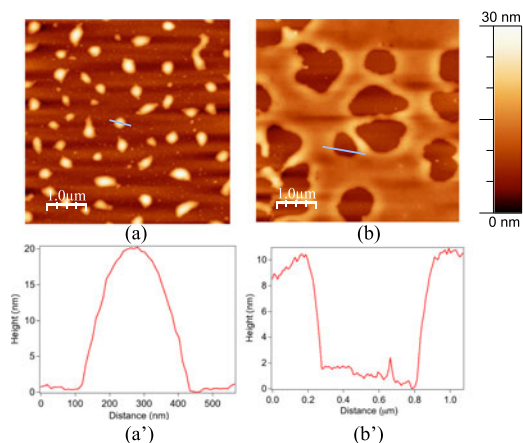
Fig. 6.   (a) and (b) AFM topography images of sp-BCP and e-BCP thin films on glass substrates taken 2 hours after deposition. (a') and (b') Topography profile curve corresponding to the blue line on the images.
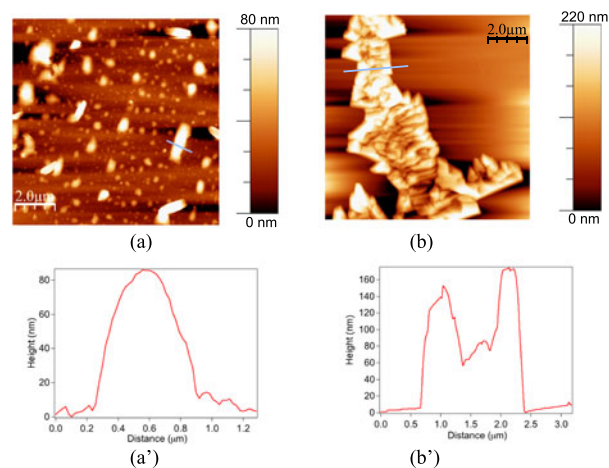
Fig. 7.   (a) and (b) AFM topography images of sp-BCP and e-BCP thin films on glass substrates taken 7 days after deposition. (a') and (b') Topography profile curve corresponding to the blue line on the images.

The *J-V* characteristics of the best-performing devices made from the different buffer layers is shown in Fig. 4. Their characteristics vary slightly, mostly by their FF and series resistance; nevertheless the devices show a very similar J_{SC} and comparable PCE (Fig. 4).
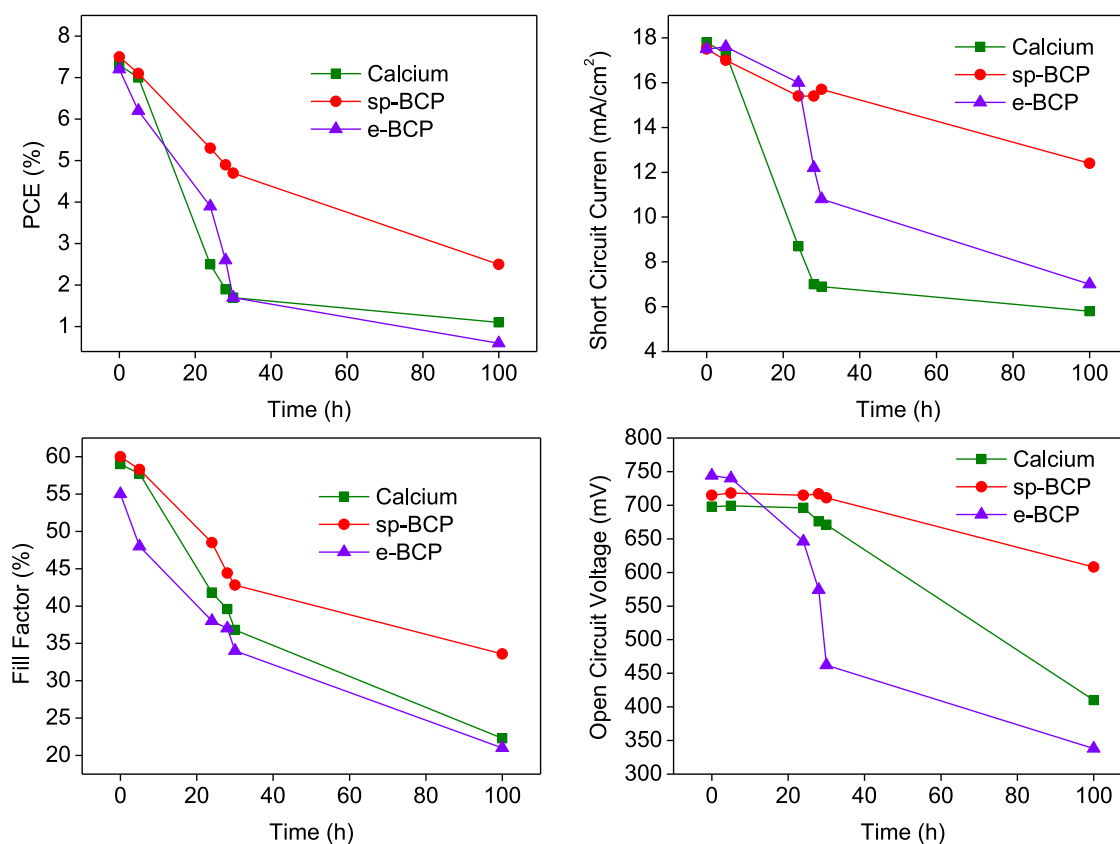
Fig. 8.   Decomposition study: plots of the evolution of PCE, J_{SC}, V_{OC} and FF *vs.* time.

As expected, the EQE spectra of all three devices have virtually identical features and overall intensity (Fig. 5). Nonetheless, a slight difference in shape between the spectra– presumably due to a difference in light reflection properties of the buffer layers– can be observed. The difference is very likely the result of the pattern formed by the BCP protrusions and voids, as seen by AFM images of the BCP layers (see discussion below), which would induce a difference in light reflectance.

AFM topography images of films deposited on glass substrates in identical conditions as in devices show that BCP does not form homogeneous layers, neither when solution processed nor when thermally evaporated (Fig. 6). Interestingly, while the sp-BCP is seen to aggregate into rather well distributed protrusions, the e-BCP shows the opposite trend where voids form from a rather leveled thin film. In the case of sp-BCP the protrusions are as high as 20 nm, while the height of the "plateaus" in e-BCP is c.a. 10 nm, as seen in the profiles in Fig. 6(a') and (b').

Interestingly, when left in air, both sp-BCP and e-BCP layers are seen to evolve with time, where material is seen to aggregate further to an extreme extent. As seen in Fig. 7(a) and (b), the sp-BCP evolves to protrusions of up to 80 nm in height and c.a. 1 um width, while e-BCP layer evolves to extremely large domains of up to 200 nm height and several microns width, leaving most of the bottom surface "naked". This can be rationalized in the framework of a nucleation a growth mechanism, in which the very small aggregates will grow to larger aggregates to minimize surface tension. Such a process might be accelerated by humidity

similarly to when a solvent annealing process is applied to an organic layer [23]–[25].

To further demonstrate the usefulness of the process, we carried out a broad stability study on the devices. That is, reference Ca-based devices and both e-BCP- and sp-BCP-made devices were left in air for a prolonged period of time and their characteristics were recorded regularly. The evolution of the key parameters of the devices (V_{OC}, J_{SC}, FF, PCE) was plotted *vs.* time, and the results are reported on Fig. 8.

As seen in the plots, the BCP-processed devices show superior stability than their respective reference devices in all aspects of their characteristics. As expected, J_{SC}, FF, and PCE all show a steady decrease with time in both the reference Ca-based devices and BCP-based devices. However the kinetics of the decrease are significantly slower in sp-BCP-based devices. Indeed, after 160 hours, the J_{SC} of BCP-based devices is still twice as high as the Ca-based device, showing a PCE close to 3 % while that of the reference devices dropped to close to 1 %. This difference in decomposition kinetics is as well demonstrated by the evolution of the FF, which is seen to drop to 25 % in the reference devices while remaining above 35 % in the BCP-based devices over the same period of time. Similarly the V_{OC} in the Ca-based devices is seen to fall abruptly after 20 hours of monitoring reaching a final value just above 400 mV after 160 h, while the BCP-based devices still show a V_{OC} superior to 600 mV after the same time.

Surprisingly, devices made from e-BCP showed faster kinetics of degradation than those made from sp-BCP. Although

this was rather unexpected, it can be related to the fact that the formation of voids and protrusions in both BCP films is a dynamic process. As seen in the AFM images of the BCP layers, the evolution of the buffer layer morphology is faster in the case of e-BCP. This analysis indicates that the degradation of the characteristics of the BCP-based devices is likely related to morphological factors. On the contrary, the degradation of Ca-based device is purely of a chemical nature, as calcium hydrolyses rapidly in air, forming an insulating barrier of calcium hydroxide.

The difference in V_{OC}, and series resistance in the BCP-based devices is likely the result of the difference in morphology between the BCP layers. Indeed, the surface recombination kinetics of the sp-BCP are expected to be faster than those of the e-BCP, since the former has a visually lower area coverage than the e-BCP. This is consistent with the fact that devices made from sp-BCP lead to lower V_{OC} than those made from e-BCP. The higher series resistance in e-BCP, on the other hand, is presumably due to a reduced hole-injection rate consistent with the higher area coverage of the e-BCP.

Finally, the dynamic evolution of the BCP layer is likely to be responsible for the slight increase in J_{SC} observed after monitoring the devices for 24 hours (Fig. 8).

IV. CONCLUSION

In the present study we demonstrated that BCP is well suited for solution processing in polymer-based solar cells, particularly those composed of a PTB7/PC$_{71}$BM blend. We demonstrated that devices comprising a thin layer of BCP as hole blocking layer, spin coated from a dilute toluene/methanol solution directly on top of the active layer, led to similar PCEs than standard devices with *vacuum*-processed calcium as hole blocking layer. Additionally, BCP-based devices showed to have much higher stability in air than either Ca-based devices or thermally evaporated BCP. We have shown that in the case of BCP, the degradation of the devices' characteristics is likely due to a morphological evolution of the BCP layer as opposed to calcium, which is widely known to undergo chemical decomposition in air. All in all, these results provide for a very economical alternative to the commonly *vacuum*-processed hole blocking materials in OPV. The solution processed BCP has a wide range of applications either in academic research (solution processed single junction and multiple junction organic and hybrid solar cells) or in industry for the manufacture of organic solar cell modules. Work is currently under way to further slow down the kinetics of the sp-BCP evolution over time.

REFERENCES

[1] L. Dou *et al.*, "Tandem polymer solar cells featuring a spectrally matched low-bandgap polymer," *Nat. Photon.*, vol. 6, pp. 180–185, 2012.
[2] J. D. Chen *et al.*, "Single-junction polymer solar cells exceeding 10% power conversion efficiency," *Adv. Mater.*, vol. 27, pp. 1035–1041, 2015.
[3] Z. He *et al.*, "Single-junction polymer solar cells with high efficiency and photovoltage," *Nat. Photon.*, vol. 9, pp. 174–179, 2015.
[4] W. Zhao *et al.*, "Fullerene-free polymer solar cells with over 11% efficiency and excellent thermal stability," *Adv. Mater.*, vol. 28, pp. 4734–4739, 2016.
[5] [Online]. Available: https://http://www.ise.fraunhofer.de/en/downloads-englisch/pdf-files-englisch/photovoltaics-report-slides.pdf
[6] [Online]. Available: http://www.heliatek.com/en/heliafilm/technical-data
[7] T. D. Nielsen, C. Cruickshank, S. Foged, J. Thorsen, and F. C. Krebs, "Business, market and intellectual property analysis of polymer solar cells," *Sol. Energy Mater. Sol. Cells*, vol. 94, pp. 1553–1571, Oct. 2010.
[8] L. Lucera *et al.*, "Guidelines for closing the efficiency gap between hero solar cells and roll-to-roll printed modules," *Energy Technol.*, vol. 3, pp. 373–384, 2015.
[9] M. Jørgensen, K. Norrman, S. A. Gevorgyan, T. Tromholt, B. Andreasen, and F. C. Krebs, "Stability of polymer solar cells," *Adv. Mater.*, vol. 24, pp. 580–612, 2012.
[10] R. R. Søndergaard, M. Hösel, and F. C. Krebs, "Roll-to-roll fabrication of large area functional organic materials," *J. Polymer Sci. Part B, Polymer Phys.*, vol. 51, pp. 16–34, 2013.
[11] P. Han *et al.*, "Improving the efficiency of PTB1: PCBM bulk heterojunction solar cells by polymer blend solution aging," *IEEE J. Photovolt.*, vol. 5, no. 3, pp. 889–896, May 2015.
[12] V. Samuel Balderrama *et al.*, "Organic solar cells toward the fabrication under Air environment," *IEEE J. Photovolt.*, vol. 6, no. 2, pp. 491–497, Mar. 2016.
[13] H. Gommans *et al.*, "On the role of bathocuproine in organic photovoltaic cells," *Adv. Funct. Mater.*, vol. 18, pp. 3686–3691, Nov. 24, 2008.
[14] T. Sakurai, S. Toyoshima, H. Kitazume, S. Masuda, H. Kato, and K. Akimoto, "Influence of gap states on electrical properties at interface between bathocuproine and various types of metals," *J. Appl. Phys.*, vol. 107, Feb. 15, 2010, Art. no. 043707.
[15] B. E. Lassiter *et al.*, "Organic photovoltaics incorporating electron conducting exciton blocking layers," *Appl. Phys. Lett.*, vol. 98, Jun. 13, 2011, Art. no. 243307.
[16] P. Peumans and S. R. Forrest, "Very-high-efficiency double-heterostructure copper phthalocyanine/C-60 photovoltaic cells," *Appl. Phys. Lett.*, vol. 79, pp. 126–128, Jul. 2, 2001.
[17] J. W. Ryan, T. Kirchartz, A. Viterisi, J. Nelson, and E. Palomares, "Understanding the effect of donor layer thickness and a MoO3 hole transport layer on the open-circuit voltage in squaraine/C-60 bilayer solar cells," *J. Phys. Chem. C*, vol. 117, pp. 19866–19874, Oct. 3, 2013.
[18] S. Wang *et al.*, "N,N-diarylanilinosquaraines and their application to organic photovoltaics," *Chem. Mater.*, vol. 23, pp. 4789–4798, 2011.
[19] S. Wang *et al.*, "High efficiency organic photovoltaic cells based on a vapor deposited squaraine donor," *Appl. Phys. Lett.*, vol. 94, Jun. 8, 2009, Art. no. 233304.
[20] G. Wei, S. Wang, K. Renshaw, M. E. Thompson, and S. R. Forrest, "Solution-processed squaraine bulk heterojunction photovoltaic cells," *ACS Nano*, vol. 4, pp. 1927–1934, 2010.
[21] X. Xiao *et al.*, "Small-molecule photovoltaics based on functionalized squaraine donor blends," *Adv. Mater.*, vol. 24, pp. 1956–1960, 2012.
[22] D.-X. Yuan *et al.*, "A solution-processed bathocuproine cathode interfacial layer for high-performance bromine-iodine perovskite solar cells," *Phys. Chem. Chem. Phys.*, vol. 17, pp. 26653–26658, 2015.
[23] G. De Luca *et al.*, "Nucleation-governed reversible self-assembly of an organic semiconductor at surfaces: Long-range mass transport forming giant functional fibers," *Adv. Funct. Mater.*, vol. 17, no. 18, pp. 3791–3798, 2007.
[24] G. De Luca *et al.*, "Self-assembly of discotic molecules into mesoscopic crystals by solvent-vapour annealing," *Soft Matter*, vol. 4, no. 10, pp. 2064–2070, 2008.
[25] G. De Luca *et al.*, "Solvent vapour annealing of organic thin films: Controlling the self-assembly of functional systems across multiple length scales," *J. Mater. Chem.*, vol. 20, no. 13, pp. 2493–2498, 2010.
[26] C. Li *et al.*, "A phenanthroline derivative as exciton blocking material for organic solar cells," *Dyes Pigments*, vol. 97, no. 1, pp. 258–261, 2013.
[27] H. Gommans *et al.*, "On the role of bathocuproine in organic photovoltaic cells," *Adv. Funct. Mater.*, vol. 18, pp. 3686–3691, 2008.

Authors' photographs and biographies not available at the time of publication.

Appendix 2

Reproduction of the article

"Diphenylphenoxy-Thiophene-PDI Dimers as 2 Acceptors for OPV Applications with Open Circuit 3 Voltage Approaching 1 Volt"

Caterina Stenta, Desiré Molina, Aurélien Viterisi, María Pilar Montero-Rama, Sara Pla, Werther Cambarau, Fernando Fernández-Lázaro, Emilio Palomares, Lluis F. Marsal, Ángela Sastre-Santos

nanomaterials

MDPI

Article

Diphenylphenoxy-Thiophene-PDI Dimers as Acceptors for OPV Applications with Open Circuit Voltage Approaching 1 Volt

Caterina Stenta [1],[†], **Desiré Molina** [2],[†] [ID], **Aurélien Viterisi** [1] [ID], **María Pilar Montero-Rama** [1], **Sara Pla** [2], **Werther Cambarau** [3], **Fernando Fernández-Lázaro** [2] [ID], **Emilio Palomares** [3] [ID], **Lluis F. Marsal** [1],* and **Ángela Sastre-Santos** [2],* [ID]

[1] Departament d'Enginyeria Electrònica, Elèctrica i Automàtica, Universitat Rovira i Virgili, Avda. Països Catalans 26, 43007 Tarragona, Spain; caterina.stenta@urv.cat (C.S.); aurelien.viterisi@urv.cat (A.V.); mariadelpilar.montero@urv.cat (M.P.M.-R.)
[2] Área de Química Orgánica, Instituto de Bioingeniería, Universidad Miguel Hernández, Avda. de la Universidad, s/n, 03203 Elche, Spain; d.molina@umh.es (D.M.); saplagar@hotmail.com (S.P.); fdofdez@umh.es (F.F.-L.)
[3] Institut Català d'Investigació Química, Avda. Països Catalans 16, 43007 Tarragona, Spain; wcambarau@iciq.es (W.C.); epalomares@iciq.es (E.P.)
* Correspondence: lluis.marsal@urv.cat (L.F.M.); asastre@umh.es (Á.S.-S.); Tel.: +34-977-559-625 (L.F.M.); +34-966-658-408 (Á.S.-S.)
† These two authors contributed equally to the work described herein.

check for updates

Abstract: Two new perylenediimides (PDIs) have been developed for use as electron acceptors in solution-processed bulk heterojunction solar cells. The compounds were designed to exhibit maximal solubility in organic solvents, and reduced aggregation in the solid state. In order to achieve this, diphenylphenoxy groups were used to functionalize a monomeric PDI core, and two PDI dimers were bridged with either one or two thiophene units. In photovoltaic devices prepared using PDI dimers and a monomer in conjunction with PTB7, it was found that the formation of crystalline domains in either the acceptor or donor was completely suppressed. Atomic force microscopy, X-ray diffraction, charge carrier mobility measurements and recombination kinetics studies all suggest that the lack of crystallinity in the active layer induces a significant drop in electron mobility. Significant surface recombination losses associated with a lack of segregation in the material were also identified as a significant loss mechanism. Finally, the monomeric PDI was found to have sub-optimum LUMO energy matching the cathode contact, thus limiting charge carrier extraction. Despite these setbacks, all PDIs produced high open circuit voltages, reaching almost 1 V in one particular case.

Keywords: organic solar cells; photovoltaics; perylenediimide; non-fullerene acceptor; PTB7; bulkheterojunction

1. Introduction

The power conversion efficiency (PCE) of organic solar cells (OSCs) has surged in the last decade. Particularly, those made from bulk heterojunction solution-processed active layers have shown the most potential for practical applications [1]. In this respect, polymer and small molecule donors have both been the focus of significant research, leading to PCEs of over 10% when blends containing a fullerene-based acceptor [2–5] perylenediimide are used. Fullerenes such as $PC_{60}BM$ and $PC_{70}BM$ have traditionally dominated the field of solution-processed OPV. However, the high costs associated with their use have driven the quest for less synthetically-demanding acceptors. In addition to cost,

the poor light absorption properties of fullerenes in the visible region of the solar spectrum limit the efficiency of the active layer to that of the donor's fraction. Consequently, both polymers [6–9] and small molecules [10–17] have been considered as alternatives. Although polymers showed promising results initially, small-molecule non-fullerene acceptors ultimately became the most studied entities. Among them, molecules built around the coranulene, truxene, subphtalocyanine, perylenediimide cores, or linear alternating donor/acceptor-shaped molecules, have yielded the best results to date. Although the PCEs were typically lower than those of similar devices fabricated with [6,6]-phenyl-butyric acid methyl ester (PCBM), polymer/non-fullerene acceptor OSC devices have surpassed all reported records of polymer solar cells in recent tests, thus demonstrating that fullerenes are no longer an essential component in OPV [18–24]. Despite these encouraging results, non-fullerene acceptor materials are still yielding inconsistent results. The perylenediimide family, however, has shown more balanced performance, with several acceptors showing PCEs of over 5% [25–32], and recently, PDI-based dimers with a twisted configuration have produced a PCE of more than 8% [33]. Moreover, the important mechanisms underlying suboptimum microstructure formation in perylene-based active layers have been identified [34,35]; namely, extensive conjugation in perylene cores induces intense π–π stacking, leading to the formation of micrometer-sized acceptor domains as well as excimers in the excited state [36], both of which are detrimental to J–V characteristics of OSC devices. To overcome these problems, it was found that bridging two or more perylenediimide cores via their lateral ortho- or bay-positions reduced the propensity for aggregation, thus leading to the formation of an active layer with crystallites of moderate size [26,30,37–40].

In an attempt to tune the aggregation properties of PDI acceptors, herein we report on a library of PDI molecules substituted at the bay position with diphenylphenoxy groups. The perpendicular arrangement of the diphenylphenoxy group with respect to the perylene core was shown to effectively reduce the aggregation of the perylene derivatives in solution [41,42]. We extended this concept to the solid state by applying diphenylphenoxy-substituted PDIs to OSCs. We carried out the synthesis and characterization of two new PDI dimers bridged through the bay position with one and two thiophene units and applied them to bulk-heterojunction solar cells. The impact of the PDIs on the active layer microstructure was studied via X-ray and atomic force microscopy (AFM). Additionally, the optical and electronic properties of the active layers of all the PDIs were assessed via a study of non-geminate recombination kinetics, using the charge extraction/transient photovoltage (CE/TPV) method and electron and hole mobility measurements.

2. Results

2.1. Synthesis and Characterization of the PDI-Acceptors

PDI 1 was synthesized using methods reported in the literature [42]. PDI 2 was synthesized via Suzuki–Miyaura coupling from monobrominated intermediate PDI-Br (see ESI) and 2,5-*bis*(4,4,5, 5-tetramethyl-1,3,2-dioxaborolan-2-yl)thiophene in a 66% yield. PDI 3 was also synthesized from PDI-Br; however, in this case, via Stille coupling with 5,5′-*bis*(tributylstannyl)-2,2′-bithiophene in a 70% yield. All derivatives were purified via flash column chromatography, and were obtained in high purity (Scheme 1).
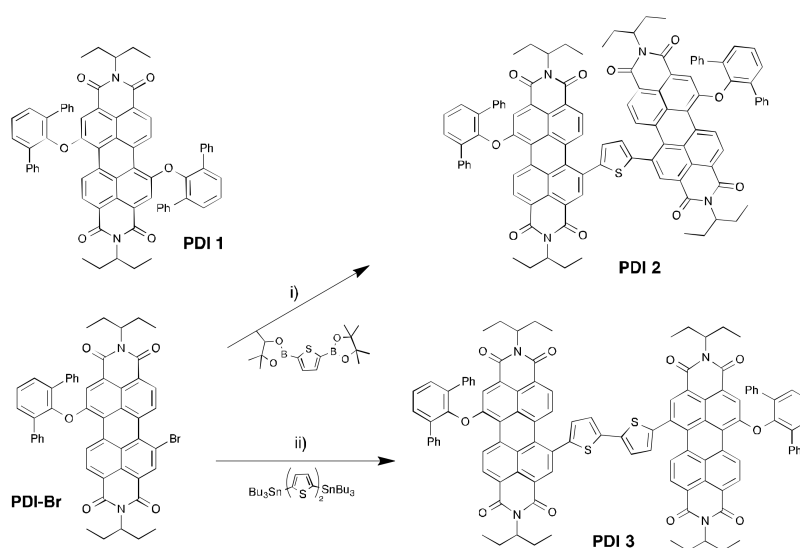
Scheme 1. Chemical structure of PDI 1 and synthesis of PDI 2 and PDI 3. Reaction conditions: (i) $Pd_2(dba)_3$, $(C_8H_{17})_4NBr$, THF/H_2O, 66%; (ii) $Pd_2(dba)_3$, $(o\text{-MeOPh})_3P$, Toluene, 70%.

In solution, all three PDIs show two intense absorption bands well centered in the visible region of the absorption spectrum, with a maximum absorption coefficient in the 10^4 range (Figure 1). Although these bands display a peak situated at an almost identical wavelength, their relative intensity varies in each PDI. The bands become broader with increasing conjugation, as seen with PDI 2 and PDI 3. When blended with PTB7 and deposited into an active layer, the PDIs are shown to extend the absorption of the active layer well in the visible region of the solar spectrum. The characteristic absorption features of both materials can be clearly seen from the absorption spectra, with absorption bands of the polymer located from 600 nm, and those of the PDIs below that value. Interestingly, with respect to the spectra, the bands belonging to the PDIs are almost unchanged when in solution. This is evidence of reduced aggregation, since a broadening of the absorption bands is usually observed in the solid state. The experimental HOMO–LUMO levels, measured via differential pulse voltammetry (see ESI) are within a similar range to those of PCBM acceptors. The LUMO levels are almost identical to those of $PC_{70}BM$ for PDI 2 and PDI 3, but significantly lower for PDI 1. The HOMO levels are slightly shifted upwards with respect to $PC_{70}BM$ (Figure 2).
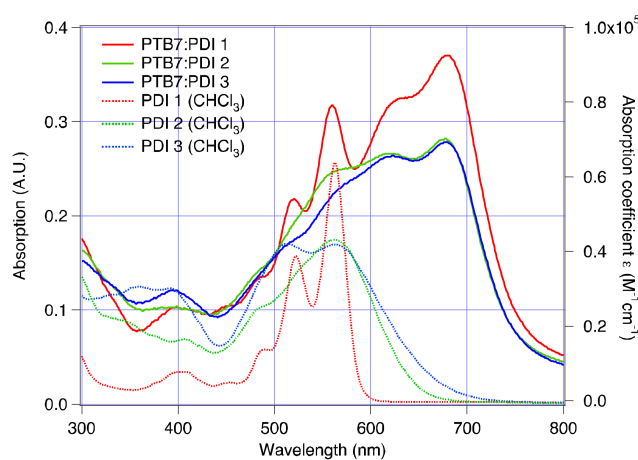
Figure 1. UV-Vis spectra of the PDI acceptors in chloroform (dotted line, right axis); UV-Vis spectra of active layers (PTB7:PDI) processed using deposition parameters from the fabrication of optimized devices (solid line, left axis).
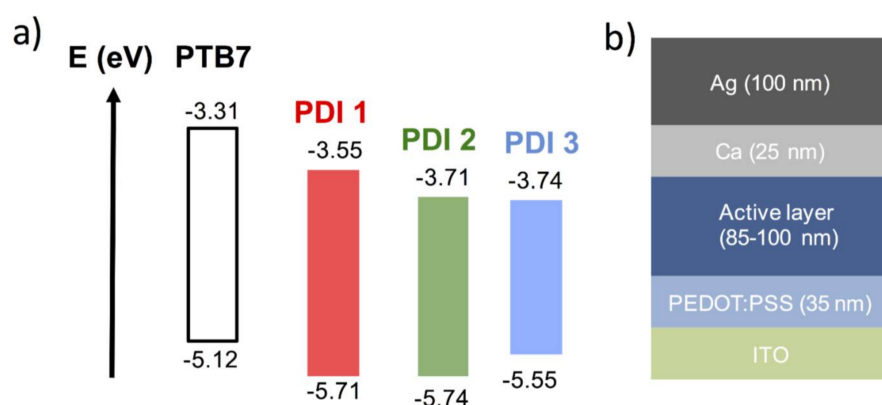
Figure 2. (**a**) HOMO and LUMO energy levels of the three PDIs; (**b**) Solar cell device architecture.

2.2. Solar Cell Devices Fabrication and Characterization

In order to assess the photovoltaic properties of our diphenylphenoxy-substituted PDIs, we fabricated solar cell devices following standard polymer-based architectures, as shown in Figure 2.

We chose PTB7 as a candidate for the polymer donor since the benzodithiophene –thienothiophenediyl copolymer family has shown the best results in devices fabricated with PDI acceptors [26–30]. The three PDIs were optimized for the donor/acceptor (D/A) ratio, annealing type and additive content. PDI 2 and PDI 3 showed high solubility in chlorobenzene at the concentration used for high PCEs PTB7/PC$_{70}$BM solar cell devices. PDI 1 had poorer solubility, and the solution of the blend was therefore diluted down to 15 mg/mL. The *J–V* characteristics of the best-performing devices are shown in Figure 3a; the main properties are shown in Table 1.
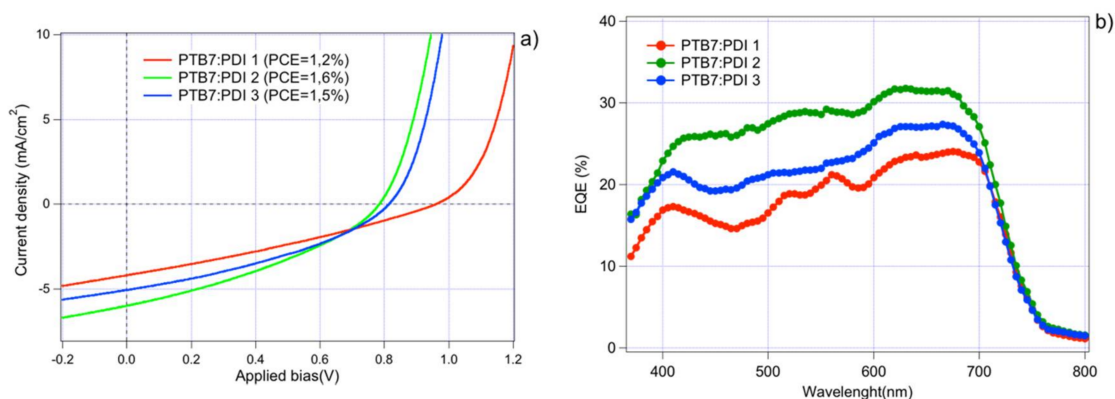
Figure 3. (**a**) *J–V* characteristics of the best performing PTB7:PDI devices recorded at 1 SUN A.M 1.5 illumination; (**b**) external quantum efficiency (EQE) spectrum of devices made from PTB7:PDI active layers.

Table 1. Organic solar cell (OSC) device parameters.

Acceptor	AL Thickness (nm)	J_{SC} (mA/cm^2)	V_{OC} (mV)	FF	PCE (%)
PDI 1	100	4.20	0.960	0.29	1.20
PDI 2	90	5.98	0.784	0.35	1.61
PDI 3	85	5.04	0.814	0.36	1.54

Interestingly, the best-performing devices were obtained when no annealing was applied, nor additive added, to the processing blend. Both thermal or solvent vapor annealing were found to

have a detrimental effect on *J*–*V* characteristics, while the addition of diiodooctane (DIO) additive was found to have no positive effect. The *J*–*V* characteristics show modest PCEs, with limited J_{SC} and an unusually low fill factor (FF). The V_{OC}, however, is seen to be higher than that of typical devices made from PCBM, approaching 1 V for PDI 1. The J_{SC} is higher with dimers than with the mono-adduct, while the V_{OC} is lower. Amongst the two dimers, the monothiophene-bridged PDI 2 was shown to yield the highest efficiency, although that of PDI 3 was very similar.

The J_{SC} trend is corroborated by the external quantum efficiency (EQE) spectrum of PDI-made devices, as seen in Figure 3b. Importantly, the PDI acceptors are seen to contribute significantly to photon conversion efficiency at lower wavelengths (500 to 600 nm). The EQE over the 350–500 range is, however, slightly lower than that of the remaining wavelengths as a result of the limited absorption of the active layers in that region of the spectrum (Figure 1).

2.3. Morphologival Characterization

To assess the impact of the PDIs whereby the formation of over-sized crystalline domains is avoided, we conducted a morphological study using X-ray diffraction and AFM microscopy techniques. Thin films of active layers were deposited on Pedot:PSS-covered glass substrates and monocrystalline Silicon (001) substrates in identical conditions to those of solar cell devices. Bragg–Brentano (theta–theta) diffractograms and grazing incidence X-ray diffraction (GIXRD) 2D area images of active layers made from each PDI were recorded in identical conditions as those previously described for PTB7/PCBM blends (see ESI) [43,44]. Unfortunately, no diffraction peaks could be detected using either technique, indicating that the PDI does not form crystalline domains in the active layer, and that it does not promote the formation of crystalline domains of polymer.

The AFM images recorded on active layers from each PDI are shown in Figure 4. As shown, all PDIs demonstrate a marked tendency to form very smooth surfaces. This corroborates the results from XRD, in which all PDIs were shown to form amorphous layers when deposited onto thin films. This is further exemplified by the RMS roughness values of the active layers, as well as the peak-to-peak height, both of which are below the average of standard PTB7-based OSCs (Table S3, ESI). The rather featureless phase images corroborate the lack of phase segregation which could be deduced from the topography images (Figure S8, ESI).
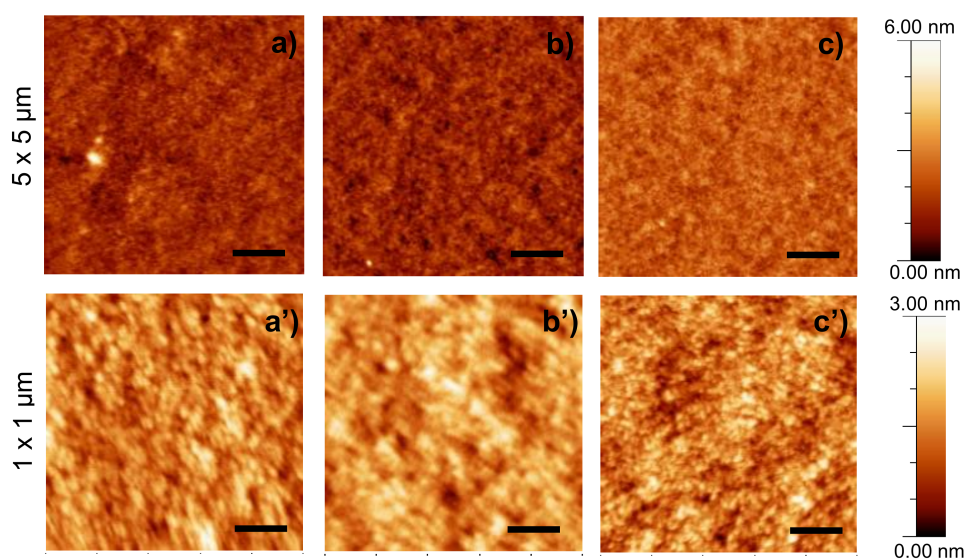
Figure 4. AFM images of the active layers made from PTB7 and PDI blends in conditions of optimized solar cell devices. (**a,a'**) PTB7:PDI 1 (1:1); (**b,b'**) PTB7:PDI 2 (1:1); (**c,c'**) PTB7:PDI 3 (1:1). Scale bar corresponds to 1 μm in the top pictures, and 200 nm in the bottom pictures.

2.4. Electrical and Photophysical Characterization

To link the morphology data with the photophysical properties of the devices, we carried out electron mobility measurements on hole-only and electron-only devices fabricated under identical conditions as those of OSC devices. We used the Mott–Gurney equation on the space charge-limited current (SCLC) region of the hole- and electron-only devices. The *J–V* characteristics were measured in the dark to calculate the zero-field electron mobility of the devices (see ESI) [45,46]. Our analysis shows that hole mobility is very similar in devices made from any of the PDIs ranging from 3.4 to 4.3×10^{-4} cm^2/V·s. However, electron mobility is up to three orders of magnitude lower that of hole mobility in all cases, creating a strong imbalance in carrier mobility. The effect on devices' characteristics is expounded in the section below.

The large difference in V_{OC} between PDI 1 and the other two PDIs cannot be attributed solely to frontier energy orbital energetics (the difference between the LUMO energy level of the acceptor and the HOMO level of the donor). However, as previously shown with similar devices, the experimental difference in V_{OC} is more likely to be attributable to non-geminate recombination kinetics [47–49]. In order to identify how the latter contributes to V_{OC}, and to some extent to the shape of the *J–V* characteristics, a qualitative recombination study was carried out using a well-established charge extraction and transient photovoltage method (see ESI for experimental details). We used CE measurements to estimate the average charge density under open circuit conditions. Figure 5a shows the plot of the charge density (n) vs. open circuit voltage obtained from CE for all the devices, where n was corrected for electrode capacitance. The data is consistent with a charge density of similar magnitude in all measurements, reaching about 2×10^{16} charges per cm^3, similar to what was reported earlier for such devices. [50–53] The total charge is seen to increase exponentially with the applied bias, a feature linked to an accumulation of charges in the bulk of the device. The plots were fitted to single exponentials according to Equation (1), and were analogous to the splitting of the quasi-Fermi levels in intrinsic semiconductors, where the value of γ (see Table 2) is indicative of an exponential tail of trap states extending into the band gap of the active layer [54–57].

$$n = n_0 e^{\gamma V_{oc}} \tag{1}$$

$$\frac{dn}{dt} = -kn^\phi \tag{2}$$

$$\tau_{\Delta n} = \tau_{\Delta n_0} n^{-\lambda} \tag{3}$$

The plots in Figure 5a and Figure S14 were combined, as shown in Figure 5b, and used to determine the overall order of recombination, defined by Equation (2); this can be approximated to $\varphi = \lambda + 1$ under our TPV experimental conditions ($\Delta n << n$) [58]. The parameter λ is obtained experimentally by fitting the curve of the small perturbation carrier life time $\tau \Delta n$ vs. n to a power law according to Equation (3).

Interestingly, the recombination order is seen to vary very significantly from device to device. For PDI 1 in particular, it shows an extremely high value ($\varphi = 16.5$). Such values, as opposed to a value of 2 (which would be expected in a strictly bimolecular recombination process), have been measured several times in earlier studies [56–64]. Importantly, recombination life times measured through CE/TPV correspond to total charge carrier recombination; therefore, it is difficult to attribute the experimental reaction order (φ), obtained using this method, to a specific recombination mechanism. Indeed, it has been shown that, especially in thin active layers as in our case, surface recombination or doping can have a very significant influence on the apparent recombination order [65].

Table 2. Values of recombination parameters and hole and electron mobility derived from charge extraction/transient photovoltage (CE/TPV) measurements and SCLC.

Acceptor	n_0	γ	β	φ	µh (cm^2/V)	µe (cm^2/Vs)	R_S (Ω/cm^2)	R_{shunt} (Ω/cm^2)
PDI 1	5.7×10^{15}	1.47	25.7	16.4	3.4×10^{-4}	2.75×10^{-7}	28.3	311.6
PDI 2	3.0×10^{15}	2.21	13.7	8.8	4.3×10^{-4}	6.02×10^{-7}	7.5	255.7
PDI 3	3.8×10^{14}	2.14	5.2	4.0	4.1×10^{-4}	9.53×10^{-7}	7.05	327.9
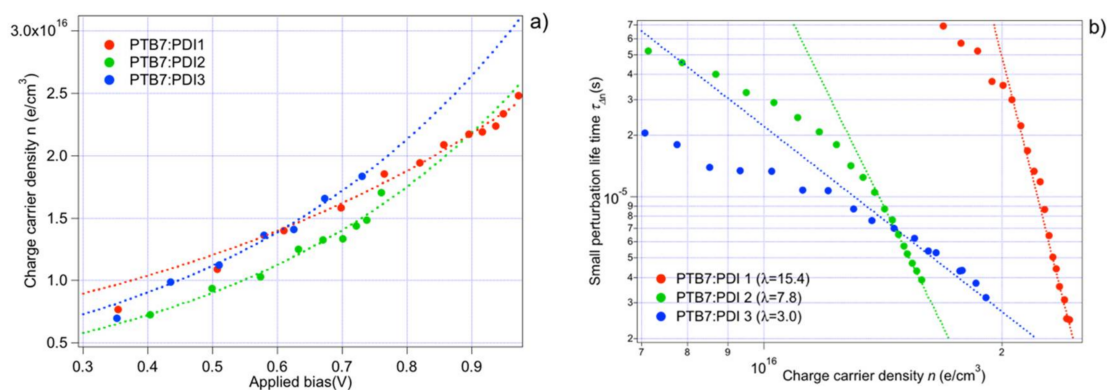
Figure 5. (**a**) Charge density (n) as a function of the open circuit voltage determined from CE measurement. The curves are fitted to an exponential growth of the form $n = n_0 e^{(\gamma V_{oc})}$ (dotted line) whose parameters are reported in Table 2; (**b**) Carriers' lifetime measured using TPV as a function of device open circuit voltage. The curves are fitted to a power decay of the form $\tau \Delta n = \tau \Delta n_0 \cdot n^{-\lambda}$ (dotted line), whose parameters are reported in Table 2.

To gain more insight into this matter, we calculated the ideality factor (n_{id}) of all devices by fitting the V_{OC} vs. light bias plot to a logarithmic function as depicted in Figure 6a. The data for n_{id} is in the range of expected values for thin devices (thickness < 100 nm) where surface recombination is significant. This is consistent with the rather high recombination orders observed experimentally. The case of the extremely high recombination order in PDI 1 is consistent with the presence of a stronger inhomogeneity of carrier concentration across the thickness of the active layer [65]. This is confirmed both by the lower n_{id} than the other two PDIs, and the J_{SC} vs. Light intensity plots (Figure 6b), which shows a sub-unity power law dependency for PDI 1.
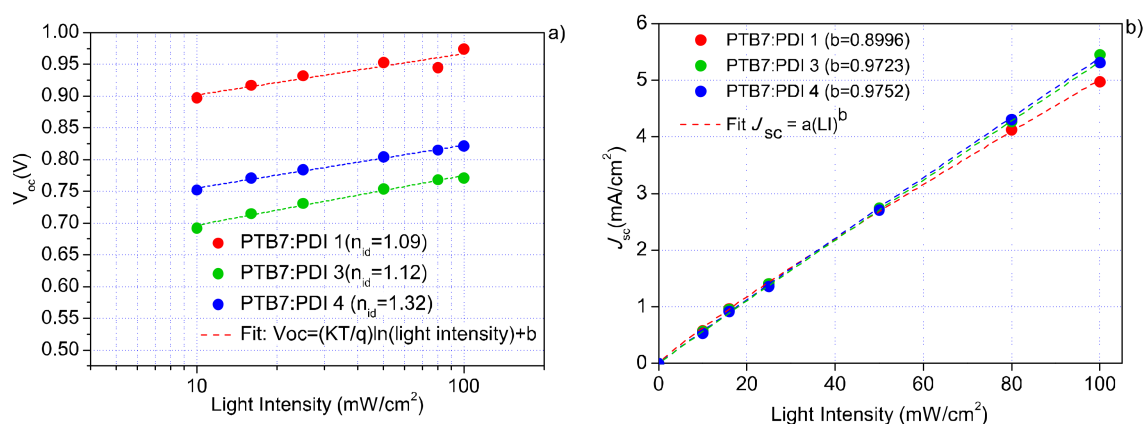
Figure 6. (**a**) Open circuit voltage vs. light intensity plot for all PDIs; (**b**) Short circuit current density vs. light intensity plot for all PDIs.

This non-linear behavior is indicative of the formation of a space charge region which is consistent with carrier dynamics dominated by surface recombination. This space charge region likely originates from the carrier mobility imbalance to a large extent, as well as from the sub-optimum HOMO energy level of PDI 1, -3.5 eV vs. -3.7 eV for PCBM, which creates a barrier to electron extraction at the cathode. Finally, despite these additional losses, the recombination coefficient K_{rec}, corresponding to a charge-dependent non-geminate recombination coefficient as defined by Equations (4) and (5) [47,54,58], follows the trend observed with the V_{OC}, indicating that non-geminate recombination plays a major role in determining the V_{OC} of the devices (Figure 7).
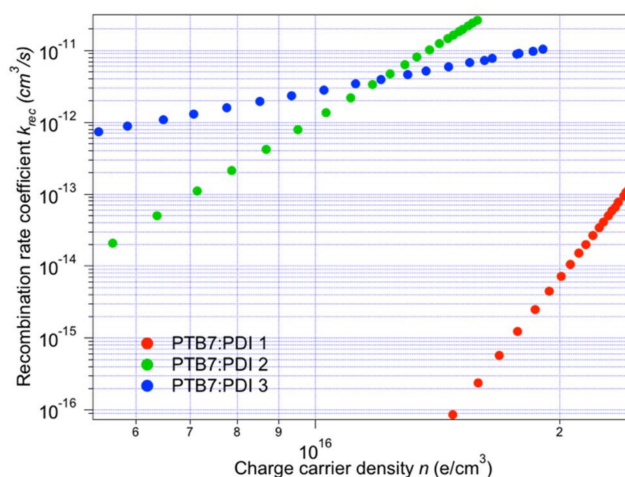
Figure 7. Recombination coefficient, K_{rec}, as a function of charge density.

$$\frac{dn}{dt} = -k_{rec}(n)n^2 \tag{4}$$

$$k_{rec}(n) = \frac{n^{\lambda-1}}{(\lambda+1)\tau_{\Delta n_0}n_0^\lambda} \tag{5}$$

The small perturbations in recombination kinetics exhibited by devices made from our PDIs are seen to be up to one order of magnitude slower than those reported for similar devices made from PCBM as an acceptor [43,50,53]. As a result, in devices made from PDIs, the V_{OC} reached a value up to 250 mV higher than that of devices made from $PC_{70}BM$, despite the fact that the latter has an almost identical LUMO energy level to that of PDI 2 and PDI 3.

Despite the fact that PDIs lead to higher V_{OC} than state-of-the-art devices, the J_{SC} and shunt resistance are lower than average (Table 2). It is likely that the amorphous nature of the active layers induces the formation of highly mixed D/A domains with poor phase segregation. This, in turn, presumably results in a high rate of geminate recombination limiting the J_{SC}, and a slow rate of charge transport (as seen by the low electron mobility), resulting in a low shunt resistance.

3. Conclusions

In the present study, we have demonstrated that the functionalization of PDI cores at the bay position with diphenylphenoxy groups leads to completely amorphous active layers when blended with PTB7. The perpendicular arrangement of the diphenylphenoxy groups with respect to the perylenediimide's plane likely impedes intermolecular π–π stacking between the conjugated cores to such an extent that the formation of crystalline domains in the solid state is suppressed. This results in devices with lower-than-average electron mobility when PDIs are used as acceptors instead of $PC_{70}BM$, as well as to significantly slower recombination kinetics. Consequently, these devices exhibit a significantly higher V_{OC} than PCBM-based devices. However, additional losses occur due to the lack of

phase segregation between donor and acceptor phases. Surface recombination becomes significant and the electron and hole mobility imbalance induce a decrease in charge extraction efficiency. This leads to *J–V* characteristics with moderate J_{SC}, and a typically low fill factor. Work is underway involving the substitution of the diphenylphenoxy at bay position for less sterically demanding groups.

Supplementary Materials: Detailed experimental procedures and additional characterization data are available online at http://www.mdpi.com/2079-4991/8/4/211/s1.

Author Contributions: A.V., A.S. and L.F.M. conceived and designed the experiments; C.S., D.M., M.P.M.-R., S.P., F.F., W.C. performed the experiments; A.V. analyzed the data; E.P. contributed to providing materials and analysis tools; A.V. wrote the paper.

Conflicts of Interest: The authors declare no conflict of interest.

References

1. Zhao, C.X.; Wang, X.; Zeng, W.; Chen, Z.K.; Ong, B.S.; Wang, K.; Deng, L.; Xu, G. Organic photovoltaic power conversion efficiency improved by AC electric field alignment during fabrication. *Appl. Phys. Lett.* **2011**, *99*, 053305. [CrossRef]

2. Chen, J.-D.; Cui, C.; Li, Y.-Q.; Zhou, L.; Ou, Q.-D.; Li, C.; Li, Y.; Tang, J.-X. Single-Junction Polymer Solar Cells Exceeding 10% Power Conversion Efficiency. *Adv. Mater.* **2015**, *27*, 1035–1041. [CrossRef] [PubMed]

3. Liao, S.-H.; Jhuo, H.-J.; Yeh, P.-N.; Cheng, Y.-S.; Li, Y.-L.; Lee, Y.-H.; Sharma, S.; Chen, S.-A. Single Junction Inverted Polymer Solar Cell Reaching Power Conversion Efficiency 10.31% by Employing Dual-Doped Zinc Oxide Nano-Film as Cathode Interlayer. *Sci. Rep.* **2014**, *4*, 6813. [CrossRef] [PubMed]

4. Kan, B.; Zhang, Q.; Li, M.; Wan, X.; Ni, W.; Long, G.; Wang, Y.; Yang, X.; Feng, H.; Chen, Y. Solution-Processed Organic Solar Cells Based on Dialkylthiol-Substituted Benzodithiophene Unit with Efficiency near 10%. *J. Am. Chem. Soc.* **2014**, *136*, 15529–15532. [CrossRef] [PubMed]

5. Zhang, Q.; Kan, B.; Liu, F.; Long, G.; Wan, X.; Chen, X.; Zuo, Y.; Ni, W.; Zhang, H.; Li, M.; et al. Small-molecule solar cells with efficiency over 9%. *Nat. Photonics* **2015**, *9*, 35–41. [CrossRef]

6. Facchetti, A. Polymer donor–polymer acceptor (all-polymer) solar cells. *Mater. Today* **2013**, *16*, 123–132. [CrossRef]

7. Guo, X.; Tu, D.; Liu, X. Recent advances in rylene diimide polymer acceptors for all-polymer solar cells. *J. Energy Chem.* **2015**, *24*, 675–685. [CrossRef]

8. Kang, H.; Lee, W.; Oh, J.; Kim, T.; Lee, C.; Kim, B.J. From Fullerene-Polymer to All-Polymer Solar Cells: The Importance of Molecular Packing, Orientation, and Morphology Control. *Acc. Chem. Res.* **2016**, *49*, 2424–2434. [CrossRef] [PubMed]

9. Kim, Y.; Lim, E. Development of Polymer Acceptors for Organic Photovoltaic Cells. *Polymers* **2014**, *6*, 382–407. [CrossRef]

10. Chen, W.; Zhang, Q. Recent progress in non-fullerene small molecule acceptors in organic solar cells (OSCs). *J. Mater. Chem. C* **2017**, *5*, 1275–1302. [CrossRef]

11. Fernandez-Lazaro, F.; Zink-Lorre, N.; Sastre-Santos, A. Perylenediimides as non-fullerene acceptors in bulk-heterojunction solar cells (BHJSCs). *J. Mater. Chem. A* **2016**, *4*, 9336–9346. [CrossRef]

12. Kozma, E.; Catellani, M. Perylene diimides based materials for organic solar cells. *Dyes Pigment.* **2013**, *98*, 160–179. [CrossRef]

13. Lin, Y.; Zhan, X. Non-fullerene acceptors for organic photovoltaics: An emerging horizon. *Mater. Horiz.* **2014**, *1*, 470–488. [CrossRef]

14. McAfee, S.M.; Topple, J.M.; Hill, I.G.; Welch, G.C. Key components to the recent performance increases of solution processed non-fullerene small molecule acceptors. *J. Mater. Chem. A* **2015**, *3*, 16393–16408. [CrossRef]

15. Nielsen, C.B.; Holliday, S.; Chen, H.-Y.; Cryer, S.J.; McCulloch, I. Non-Fullerene Electron Acceptors for Use in Organic Solar Cells. *Acc. Chem. Res.* **2015**, *48*, 2803–2812. [CrossRef] [PubMed]

16. Sonar, P.; Lim, J.P.F.; Chan, K.L. Organic non-fullerene acceptors for organic photovoltaics. *Energy Environ. Sci.* **2011**, *4*, 1558–1574. [CrossRef]

17. Zhang, S.; Ye, L.; Hou, J. Breaking the 10% Efficiency Barrier in Organic Photovoltaics: Morphology and Device Optimization of Well-Known PBDTTT Polymers. *Adv. Energy Mater.* **2016**, *6*. [CrossRef]

18. Liu, T.; Guo, Y.; Yi, Y.; Huo, L.; Xue, X.; Sun, X.; Fu, H.; Xiong, W.; Meng, D.; Wang, Z.; et al. Ternary Organic Solar Cells Based on Two Compatible Nonfullerene Acceptors with Power Conversion Efficiency >10%. *Adv. Mater.* **2016**, *28*, 10008–10015. [CrossRef] [PubMed]

19. Yang, Y.; Zhang, Z.-G.; Bin, H.; Chen, S.; Gao, L.; Xue, L.; Yang, C.; Li, Y. Side-Chain Isomerization on an n-type Organic Semiconductor ITIC Acceptor Makes 11.77% High Efficiency Polymer Solar Cells. *J. Am. Chem. Soc.* **2016**, *138*, 15011–15018. [CrossRef] [PubMed]

20. Zhao, F.; Dai, S.; Wu, Y.; Zhang, Q.; Wang, J.; Jiang, L.; Ling, Q.; Wei, Z.; Ma, W.; You, W.; et al. Single-Junction Binary-Blend Nonfullerene Polymer Solar Cells with 12.1% Efficiency. *Adv. Mater.* **2017**, *29*. [CrossRef] [PubMed]

21. Zhao, W.; Qian, D.; Zhang, S.; Li, S.; Inganas, O.; Gao, F.; Hou, J. Fullerene-Free Polymer Solar Cells with over 11% Efficiency and Excellent Thermal Stability. *Adv. Mater.* **2016**, *28*, 4734–4739. [CrossRef] [PubMed]

22. Bin, H.; Zhang, Z.-G.; Gao, L.; Chen, S.; Zhong, L.; Xue, L.; Yang, C.; Li, Y. Non-Fullerene Polymer Solar Cells Based on Alkylthio and Fluorine Substituted 2D-Conjugated Polymers Reach 9.5% Efficiency. *J. Am. Chem. Soc.* **2016**, *138*, 4657–4664. [CrossRef] [PubMed]

23. Li, S.; Ye, L.; Zhao, W.; Zhang, S.; Mukherjee, S.; Ade, H.; Hou, J. Energy-Level Modulation of Small-Molecule Electron Acceptors to Achieve over 12% Efficiency in Polymer Solar Cells. *Adv. Mater.* **2016**, *28*, 9423–9429. [CrossRef] [PubMed]

24. Zhao, W.; Li, S.; Yao, H.; Zhang, S.; Zhang, Y.; Yang, B.; Hou, J. Molecular Optimization Enables over 13% Efficiency in Organic Solar Cells. *J. Am. Chem. Soc.* **2017**, *139*, 7148–7151. [CrossRef] [PubMed]

25. Li, H.; Hwang, Y.-J.; Courtright, B.A.E.; Eberle, F.N.; Subramaniyan, S.; Jenekhe, S.A. Fine-Tuning the 3D Structure of Nonfullerene Electron Acceptors Toward High-Performance Polymer Solar Cells. *Adv. Mater.* **2015**, *27*, 3266–3272. [CrossRef] [PubMed]

26. Liu, Y.; Mu, C.; Jiang, K.; Zhao, J.; Li, Y.; Zhang, L.; Li, Z.; Lai, J.Y.L.; Hu, H.; Ma, T.; et al. A Tetraphenylethylene Core-Based 3D Structure Small Molecular Acceptor Enabling Efficient Non-Fullerene Organic Solar Cells. *Adv. Mater.* **2015**, *27*, 1015–1020. [CrossRef] [PubMed]

27. Sun, D.; Meng, D.; Cai, Y.; Fan, B.; Li, Y.; Jiang, W.; Huo, L.; Sun, Y.; Wang, Z. Non-Fullerene-Acceptor-Based Bulk-Heterojunction Organic Solar Cells with Efficiency over 7%. *J. Am. Chem. Soc.* **2015**, *137*, 11156–11162. [CrossRef] [PubMed]

28. Ye, L.; Sun, K.; Jiang, W.; Zhang, S.; Zhao, W.; Yao, H.; Wang, Z.; Hou, J. Enhanced Efficiency in Fullerene-Free Polymer Solar Cell by Incorporating Fine-designed Donor and Acceptor Materials. *ACS Appl. Mater. Interfaces* **2015**, *7*, 9274–9280. [CrossRef] [PubMed]

29. Zang, Y.; Li, C.-Z.; Chueh, C.-C.; Williams, S.T.; Jiang, W.; Wang, Z.-H.; Yu, J.-S.; Jen, A.K.Y. Integrated Molecular, Interfacial, and Device Engineering towards High-Performance Non-Fullerene Based Organic Solar Cells. *Adv. Mater.* **2014**, *26*, 5708–5714. [CrossRef] [PubMed]

30. Zhang, X.; Zhan, C.; Yao, J. Non-Fullerene Organic Solar Cells with 6.1% Efficiency through Fine-Tuning Parameters of the Film-Forming Process. *Chem. Mater.* **2015**, *27*, 166–173. [CrossRef]

31. Zhao, J.; Li, Y.; Lin, H.; Liu, Y.; Jiang, K.; Mu, C.; Ma, T.; Lin Lai, J.Y.; Hu, H.; Yu, D.; et al. High-efficiency non-fullerene organic solar cells enabled by a difluorobenzothiadiazole-based donor polymer combined with a properly matched small molecule acceptor. *Energy Environ. Sci.* **2015**, *8*, 520–525. [CrossRef]

32. Zhong, Y.; Trinh, M.T.; Chen, R.; Wang, W.; Khlyabich, P.P.; Kumar, B.; Xu, Q.; Nam, C.-Y.; Sfeir, M.Y.; Black, C.; et al. Efficient Organic Solar Cells with Helical Perylene Diimide Electron Acceptors. *J. Am. Chem. Soc.* **2014**, *136*, 15215–15221. [CrossRef] [PubMed]

33. Meng, D.; Sun, D.; Zhong, C.; Liu, T.; Fan, B.; Huo, L.; Li, Y.; Jiang, W.; Choi, H.; Kim, T.; et al. High-Performance Solution-Processed Non-Fullerene Organic Solar Cells Based on Selenophene-Containing Perylene Bisimide Acceptor. *J. Am. Chem. Soc.* **2016**, *138*, 375–380. [CrossRef] [PubMed]

34. Li, H.; Earmme, T.; Ren, G.; Saeki, A.; Yoshikawa, S.; Murari, N.M.; Subramaniyan, S.; Crane, M.J.; Seki, S.; Jenekhe, S.A. Beyond Fullerenes: Design of Nonfullerene Acceptors for Efficient Organic Photovoltaics. *J. Am. Chem. Soc.* **2014**, *136*, 14589–14597. [CrossRef] [PubMed]

35. Yan, Q.; Zhou, Y.; Zheng, Y.-Q.; Pei, J.; Zhao, D. Towards rational design of organic electron acceptors for photovoltaics: A study based on perylenediimide derivatives. *Chem. Sci.* **2013**, *4*, 4389–4394. [CrossRef]

36. Margulies, E.A.; Shoer, L.E.; Eaton, S.W.; Wasielewski, M.R. Excimer formation in cofacial and slip-stacked perylene-3,4:9,10-bis(dicarboximide) dimers on a redox-inactive triptycene scaffold. *Phys. Chem. Chem. Phys.* **2014**, *16*, 23735–23742. [CrossRef] [PubMed]

37. Hartnett, P.E.; Timalsina, A.; Matte, H.S.S.R.; Zhou, N.; Guo, X.; Zhao, W.; Facchetti, A.; Chang, R.P.H.; Hersam, M.C.; Wasielewski, M.R.; et al. Slip-Stacked Perylenediimides as an Alternative Strategy for High Efficiency Nonfullerene Acceptors in Organic Photovoltaics. *J. Am. Chem. Soc.* **2014**, *136*, 16345–16356. [CrossRef] [PubMed]

38. Liu, S.-Y.; Wu, C.-H.; Li, C.-Z.; Liu, S.-Q.; Wei, K.-H.; Chen, H.-Z.; Jen, A.K.Y. A Tetraperylene Diimides Based 3D Nonfullerene Acceptor for Efficient Organic Photovoltaics. *Adv. Sci.* **2015**, *2*, 1500014. [CrossRef] [PubMed]

39. Shivanna, R.; Shoaee, S.; Dimitrov, S.; Kandappa, S.K.; Rajaram, S.; Durrant, J.R.; Narayan, K.S. Charge generation and transport in efficient organic bulk heterojunction solar cells with a perylene acceptor. *Energy Environ. Sci.* **2014**, *7*, 435–441. [CrossRef]

40. Zhang, X.; Lu, Z.; Ye, L.; Zhan, C.; Hou, J.; Zhang, S.; Jiang, B.; Zhao, Y.; Huang, J.; Zhang, S.; et al. A Potential Perylene Diimide Dimer-Based Acceptor Material for Highly Efficient Solution-Processed Non-Fullerene Organic Solar Cells with 4.03% Efficiency. *Adv. Mater.* **2013**, *25*, 5791–5797. [CrossRef] [PubMed]

41. Lin, M.-J.; Jimenez, A.J.; Burschka, C.; Wurthner, F. Bay-substituted perylene bisimide dye with an undistorted planar scaffold and outstanding solid state fluorescence properties. *Chem. Commun.* **2012**, *48*, 12050–12052. [CrossRef] [PubMed]

42. Ramirez, M.G.; Pla, S.; Boj, P.G.; Villalvilla, J.M.; Quintana, J.A.; Diaz-Garcia, M.A.; Fernandez-Lazaro, F.; Sastre-Santos, A. 1,7-Bay-Substituted Perylenediimide Derivative with Outstanding Laser Performance. *Adv Opt. Mater.* **2013**, *1*, 933–938. [CrossRef]

43. Han, P.L.; Viterisi, A.; Ferre-Borrull, J.; Pallares, J.; Marsal, L.F. Morphology-driven photocurrent enhancement in PTB7/PC71BM bulk heterojunction solar cells via the use of ternary solvent processing blends. *Org. Electron.* **2017**, *41*, 229–236. [CrossRef]

44. Deng, L.; Wang, K.; Zhao, C.X.; Yan, H.; Britten, J.F.; Xu, G. Phase and Texture of Solution-Processed Copper Phthalocyanine Thin Films Investigated by Two-Dimensional Grazing Incidence X-ray Diffraction. *Crystals* **2011**, *1*, 112–119. [CrossRef]

45. Blom, P.W.M.; Mihailetchi, V.D.; Koster, L.J.A.; Markov, D.E. Device Physics of Polymer:Fullerene Bulk Heterojunction Solar Cells. *Adv. Mater.* **2007**, *19*, 1551–1566. [CrossRef]

46. Mihailetchi, V.D.; van Duren, J.K.J.; Blom, P.W.M.; Hummelen, J.C.; Janssen, R.A.J.; Kroon, J.M.; Rispens, M.T.; Verhees, W.J.H.; Wienk, M.M. Electron Transport in a Methanofullerene. *Adv. Funct. Mater.* **2003**, *13*, 43–46. [CrossRef]

47. Credgington, D.; Durrant, J.R. Insights from Transient Optoelectronic Analyses on the Open-Circuit Voltage of Organic Solar Cells. *J. Phys. Chem. Lett.* **2012**, *3*, 1465–1478. [CrossRef] [PubMed]

48. Maurano, A.; Hamilton, R.; Shuttle, C.G.; Ballantyne, A.M.; Nelson, J.; O'Regan, B.; Zhang, W.M.; McCulloch, I.; Azimi, H.; Morana, M.; et al. Recombination Dynamics as a Key Determinant of Open Circuit Voltage in Organic Bulk Heterojunction Solar Cells: A Comparison of Four Different Donor Polymers. *Adv. Mater.* **2010**, *22*, 4987–4992. [CrossRef] [PubMed]

49. Garcia-Belmonte, G.; Bisquert, J. Open-circuit voltage limit caused by recombination through tail states in bulk heterojunction polymer-fullerene solar cells. *Appl. Phys. Lett.* **2010**, *96*, 113301–113303. [CrossRef]

50. Etxebarria, I.; Guerrero, A.; Albero, J.; Garcia-Belmonte, G.; Palomares, E.; Pacios, R. Inverted vs standard PTB7:PC70BM organic photovoltaic devices. The benefit of highly selective and extracting contacts in device performance. *Org. Electron.* **2014**, *15*, 2756–2762. [CrossRef]

51. Foertig, A.; Kniepert, J.; Gluecker, M.; Brenner, T.; Dyakonov, V.; Neher, D.; Deibel, C. Nongeminate and Geminate Recombination in PTB7: PCBM Solar Cells. *Adv. Funct. Mater.* **2014**, *24*, 1306–1311. [CrossRef]

52. Rauh, D.; Deibel, C.; Dyakonov, V. Charge Density Dependent Nongeminate Recombination in Organic Bulk Heterojunction Solar Cells. *Adv. Funct. Mater.* **2012**, *22*, 3371–3377. [CrossRef]

53. Guerrero, A.; Montcada, N.F.; Ajuria, J.; Etxebarria, I.; Pacios, R.; Garcia-Belmonte, G.; Palomares, E. Charge carrier transport and contact selectivity limit the operation of PTB7-based organic solar cells of varying active layer thickness. *J. Mater. Chem. A* **2013**, *1*, 12345–12354. [CrossRef]

54. Eng, M.P.; Barnes, P.R.F.; Durrant, J.R. Concentration-Dependent Hole Mobility and Recombination Coefficient in Bulk Heterojunctions Determined from Transient Absorption Spectroscopy. *J. Phys. Chem. Lett.* **2010**, *1*, 3096–3100. [CrossRef]

55. Shuttle, C.G.; Hamilton, R.; Nelson, J.; O'Regan, B.C.; Durrant, J.R. Measurement of Charge-Density Dependence of Carrier Mobility in an Organic Semiconductor Blend. *Adv. Funct. Mater.* **2010**, *20*, 698–702. [CrossRef]

56. Shuttle, C.G.; Hamilton, R.; O'Regan, B.C.; Nelson, J.; Durrant, J.R. Charge-density-based analysis of the current–voltage response of polythiophene/fullerene photovoltaic devices. *Proc. Natl. Acad. Sci. USA* **2010**, *107*, 16448–16452. [CrossRef] [PubMed]

57. Spoltore, D.; Oosterbaan, W.D.; Khelifi, S.; Clifford, J.N.; Viterisi, A.; Palomares, E.; Burgelman, M.; Lutsen, L.; Vanderzande, D.; Manca, J. Effect of Polymer Crystallinity in P3HT:PCBM Solar Cells on Band Gap Trap States and Apparent Recombination Order. *Adv. Energy Mater.* **2013**, *3*, 466–471. [CrossRef]

58. Maurano, A.; Shuttle, C.C.; Hamilton, R.; Ballantyne, A.M.; Nelson, J.; Zhang, W.; Heeney, M.; Durrant, J.R. Transient Optoelectronic Analysis of Charge Carrier Losses in a Selenophene/Fullerene Blend Solar Cell. *J. Phys. Chem. C* **2011**, *115*, 5947–5957. [CrossRef]

59. Fernandez, D.; Viterisi, A.; Challuri, V.; Ryan, J.W.; Martinez-Ferrero, E.; Gispert-Guirado, F.; Martinez, M.; Escudero, E.; Stenta, C.; Marsal, L.F.; et al. Understanding the Limiting Factors of Solvent-Annealed Small-Molecule Bulk-Heterojunction Organic Solar Cells from a Chemical Perspective. *Chemsuschem* **2017**, *10*, 3118–3134. [CrossRef] [PubMed]

60. Fernandez, D.; Viterisi, A.; William Ryan, J.; Gispert-Guirado, F.; Vidal, S.; Filippone, S.; Martin, N.; Palomares, E. Small molecule BHJ solar cells based on DPP(TBFu)(2) and diphenylmethanofullerenes (DPM): Linking morphology, transport, recombination and crystallinity. *Nanoscale* **2014**, *6*, 5871–5878. [CrossRef] [PubMed]

61. Ryan, J.W.; Kirchartz, T.; Viterisi, A.; Nelson, J.; Palomares, E. Understanding the Effect of Donor Layer Thickness and a MoO_3 Hole Transport Layer on the Open-Circuit Voltage in Squaraine/C-60 Bilayer Solar Cells. *J. Phys. Chem. C* **2013**, *117*, 19866–19874. [CrossRef]

62. Montcada, N.F.; Pelado, B.; Viterisi, A.; Albero, J.; Coro, J.; de la Cruz, P.; Langa, F.; Palomares, E. High open circuit voltage in efficient thiophene-based small molecule solution processed organic solar cells. *Org. Electron.* **2013**, *14*, 2826–2832. [CrossRef]

63. MacKenzie, R.C.I.; Kirchartz, T.; Dibb, G.F.A.; Nelson, J. Modeling Nongeminate Recombination in P3HT:PCBM Solar Cells. *J. Phys. Chem. C* **2011**, *115*, 9806–9813. [CrossRef]

64. Kirchartz, T.; Pieters, B.E.; Kirkpatrick, J.; Rau, U.; Nelson, J. Recombination via tail states in polythiophene:fullerene solar cells. *Phys. Rev. B Condens. Matter Mater. Phys.* **2011**, *83*, 115209. [CrossRef]

65. Kirchartz, T.; Nelson, J. Meaning of reaction orders in polymer:fullerene solar cells. *Phys. Rev. B Condens. Matter Mater. Phys.* **2012**, *86*, 165201. [CrossRef]

Supporting Information

Diphenylphenoxy-Thiophene-PDIs acceptors for OPV applications with open circuit voltage approaching 1 volt.

Caterina Stenta, Desiré Molina, Aurelien Viterisi, María Pilar Montero-Rama, Sara Pla, Werther Cambarau, Fernando Fernández-Lázaro, Emilio Palomares, Lluis F. Marsal,* Ángela Sastre-Santos *

Supporting Information

General Remarks on Experimental Data

Synthetic Procedures: All chemicals were reagent-grade, purchased from commercial sources, and used as received, unless otherwise specified. Column chromatography: SiO_2 (40-63 μm) TLC plates coated with SiO_2 60F254 were visualized by UV light. NMR spectra were measured with a Bruker AC 300. UV-vis spectra were recorded with a Helios Gamma spectometer at 298 K in $CHCl_3$, and IR spectra and a Nicolet Impact 400D spectrophotomete in a KI matrix. Fluorescence spectra were recorded with a Perkin Elmer LS 55. Mass spectra were obtained from a Bruker Microflex matrix-assisted laserdesorption/ionization time of flight (MALDI-TOF).

Synthesis Procedures and Characterisation Data

PDI 2: In a 100 ml round-bottom flask were introduced PDI 4 (513 mg, 0.60 mmol), bis(4,4,5,5-tetramethyl-1,3,2-dioxaborolan-2-yl)thiophene (124 mg, 0.37 mmol), $Pd_2(dba)_3$ (36 g, 0.04 mmol) and tetraoctylammonium bromide (21 mg, 0.04 mmol). Then the solvents were added subsequently, THF (40 mL) and K_2CO_3 2M (2 ml). The reaction mixture was stirred for 3 h at 80 ºC under argon atmosphere. After cooling to room temperature, the crude was extracted with dichloromethane and washed with water. The solvent was removed under reduced pressure and the crude product was purified by silica gel column chromatography (SiO_2, dichloromethane:acetone 25:1) to yield **PDI 2** (398 mg, 66 %) as a purple solid. ^{1}H NMR (300 MHz, $CDCl_3$, 300 K, δ): δ = 9.11 (2H, d, J=8.4 Hz, 2xPDI-H), 8.74 (2H, s, 2xPDI-H), 8.59 (2H, d, J=8.4 Hz, 2xPDI-H), 8.42 (2H, d, J=8.1 Hz, 2xPDI-H), 8.13 (2H, d, J=8.1 Hz, 1xPDI-H), 7.86 (2H, s, 2xPDI-H), 7.50 (6H, s, 6xAr-H), 7.39-7.35 (10H, m, 8xAr-H+2xthiophene-H), 6.99-6.88 (12H, m, 12xAr-H), 5.17-5.06 (2H, m, 2xPDI-CH(CH$_2$CH$_3$)$_2$), 4.87-4.77 (2H, m, 2xPDI-CH(CH$_2$CH$_3$)$_2$), 2.39-

2.24 (4H, m, 2xPDI-CH(C*H*HCH$_3$)$_2$), 2.11-1.92 (8H, m, 4xPDI-CH(CH*H*CH$_3$)$_2$), 1.84-1.73 (4H, m, 2xPDI-CH(C*H*HCH$_3$)$_2$), 0.97 (12H, t, J=7.5 Hz, 2xPDI-CH(CH$_2$C*H$_3$*)$_2$), 0.73 ppm (12H, t, J=7.5 Hz, 2xPDI-CH(CH$_2$C*H$_3$*)$_2$); ^{13}C NMR (75 MHz, CDCl$_2$-CDCl$_2$): δ = 164.0, 163.9, 163.6, 163.2, 155.7, 148.0, 146.5, 137.2, 135.8, 135.1, 133.7, 133.3, 132.6, 131.2, 131.0, 129.8, 128.8, 128.7, 128.4, 128.3, 128.0, 127.8, 127.3, 126.4, 123.9, 123.3, 122.4, 122.2, 121.8, 121.0, 120.7, 57.7, 57.5, 25.0, 24.8, 11.4, 11.1 ppm; IR (KBr) v: 3442, 3056, 2961, 2874, 1698, 1658, 1589, 1505, 1458, 1405, 1327, 1261, 1191, 1073, 903, 859, 811, 754, 699, 582, 408 cm^{-1}; UV/Vis (chloroform), λ_{max} (log ε): 408 (4.22), 562 nm (4.64); MS (MALDI-TOF): m/z: calcd for C$_{108}$H$_{84}$N$_4$O$_{10}$S: 1626.591 [M]$^-$; found: m/z: 1628.543 [M]$^-$.

PDI 3: In a dry 25 ml round-bottom flask were introduced PDI 4 (100 mg, 0.12 mmol), 5,5′-bis(tributylstannyl)-2,2′-bithiophene (36 mg, 0.05 mmol), tris(dibenzylideneacetone)dipalladium(0) (Pd$_2$(dba)$_3$) (4.3 mg, 4.7x10^{-3} mmol) and tris(2-methoxyphenyl)phosphine ((o-MeOPh)$_3$P) (6.6 mg, 0.02 mmol) was stirred in dry toluene (1 mL) under argon for 48 h at 110 ºC. The solvent was removed under reduced pressure and the crude product was purified by silica gel column chromatography (SiO$_2$, chloroform) to yield **PDI 3** (60 mg, 70 %) as a shiny purple solid. ^{1}H NMR (300 MHz, CDCl$_3$, 300 K, δ): δ = 9.16 (2H, d, J=8.4 Hz, 2xPDI-*H*), 8.70 (2H, s, 2xPDI-*H*), 8.58 (2H, d, J=8.4 Hz, 2xPDI-*H*), 8.35 (2H, d, J=8.2 Hz, 2xPDI-*H*), 8.14 (2H, d, J=8.2 Hz, 1xPDI-*H*), 7.92 (2H, s, 2xPDI-*H*), 7.55-7.52 (6H, m, 6xAr-*H*), 7.45-7.42 (8H, m, 8xAr-*H*), 7.21 (2H, d, J=3.7 Hz, 2xthiophene-*H*), 7.16 (2H, d, J=3.7 Hz, 2xthiophene-*H*), 7.09-7.01 (12H, m, 12xAr-*H*), 5.14-5.04 (2H, m, 2xPDI-C*H*(CH$_2$CH$_3$)$_2$), 4.98-4.87 (2H, m, 2xPDI-C*H*(CH$_2$CH$_3$)$_2$), 2.37-2.22 (4H, m, 2xPDI-CH(C*H*HCH$_3$)$_2$), 2.20-2.07 (4H, m, 2xPDI-CH(CH*H*CH$_3$)$_2$), 2.03-1.79 (8H, m, 2xPDI-CH(C*H*HCH$_3$)$_2$), 0.95 (12H, t, J=7.4 Hz, 2xPDI-CH(CH$_2$C*H$_3$*)$_2$), 0.86 ppm (12H, t, J=7.4 Hz, 2xPDI-CH(CH$_2$C*H$_3$*)$_2$).; ^{13}C NMR (75 MHz, CDCl$_2$-CDCl$_2$): δ = 164.3, 164.2, 164.0, 163.5,

155.9, 148.0, 143.9, 139.0, 137.5, 136.0, 134.0, 133.7, 133.1, 131.7, 131.3, 129.9, 129.1, 128.6, 128.4, 128.1, 127.5, 126.7, 125.9, 124.2, 123.5, 122.4, 122.2, 122.0, 121.0, 120.9, 57.9, 57.7, 25.2, 25.1, 11.6, 11.4 ppm; IR (KBr) v: 3432, 2961, 2928, 2874, 1698, 1659, 1596, 1505, 1459, 1405, 1327, 1261, 1193, 1074, 903, 860, 812, 754, 700, 408 cm^{-1}; UV/Vis (chloroform), λ_{max} (log ε): 358 (4.48), 392 (4.48), 514 (4.62), 562 nm (4.62); MS (MALDI-TOF): m/z: calcd for $C_{112}H_{86}N_4O_{10}S_2$: 1709.571 [M-H]$^-$; found: m/z: 1709.524 [M-H]$^-$.
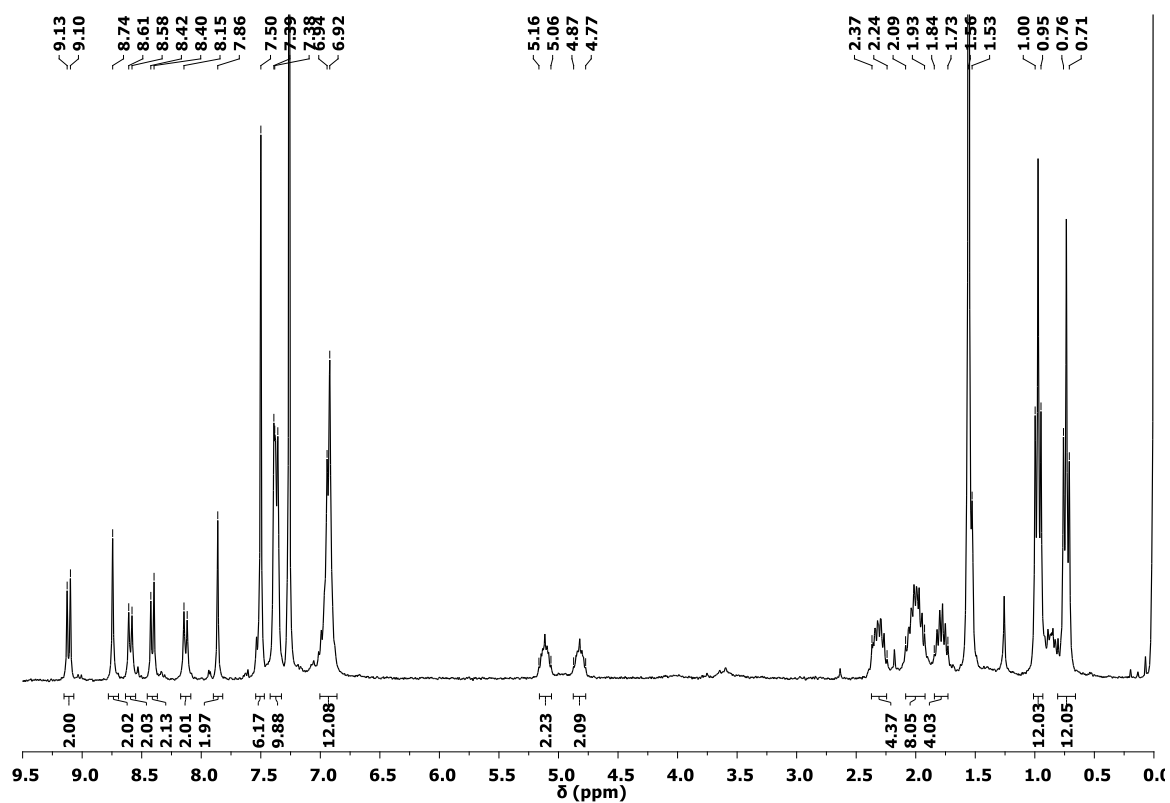
Figure S1. ^{1}H-RMN (CHCl$_3$, 25°C) spectrum for **PDI 2**.
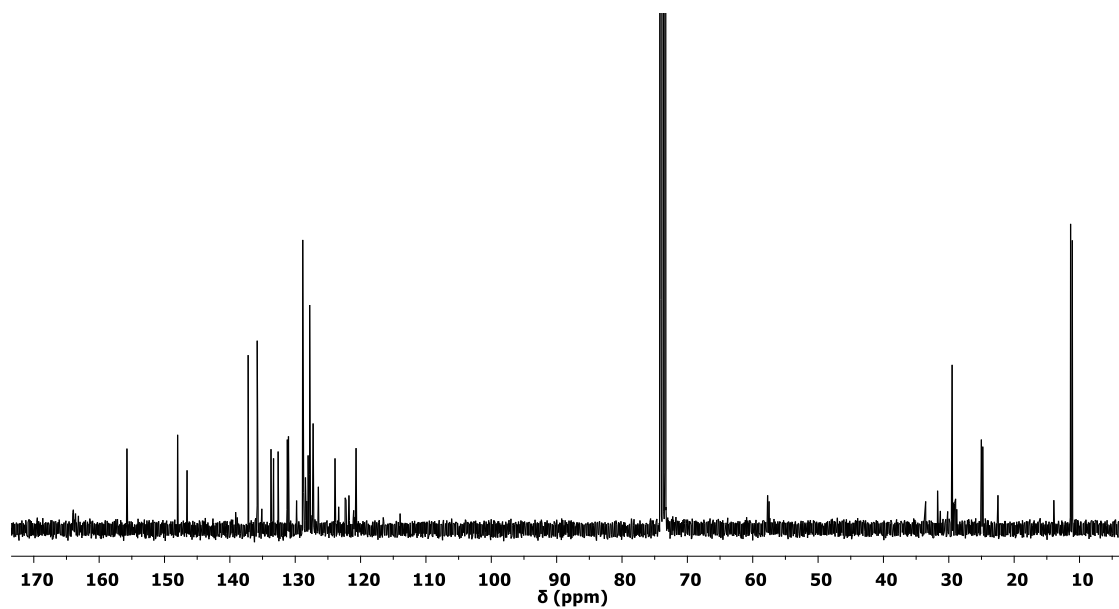
Figure S2. ^{13}C-RMN (CDCl$_2$-CDCl$_2$, 25°C) spectrum for **PDI 2**.
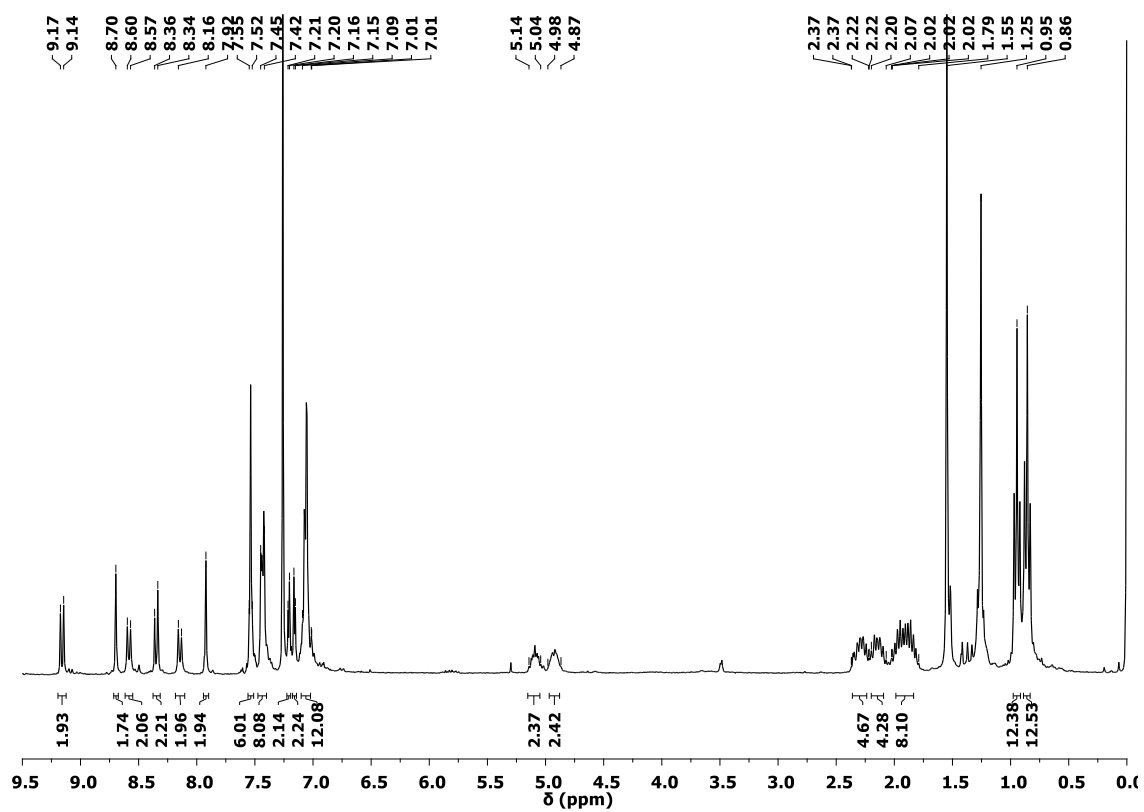
Figure S3. ^{1}H-RMN (CHCl$_3$, 25°C) spectrum for **PDI 3**.
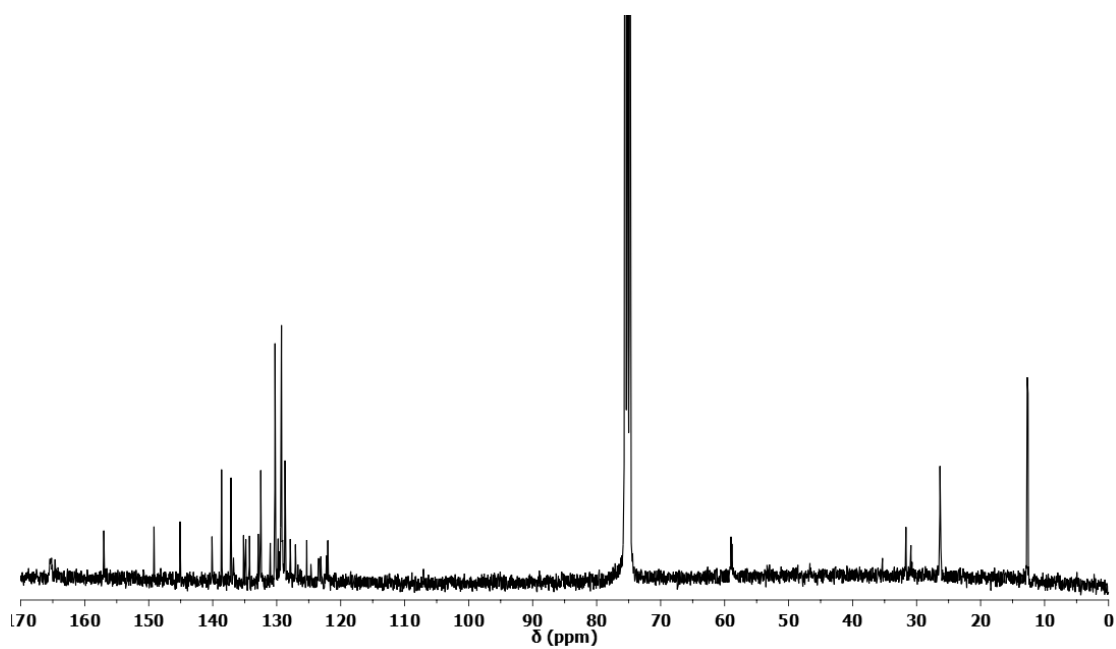
Figure S4. ^{13}C-RMN (CDCl$_2$-CDCl$_2$, 50°C) spectrum for **PDI 3.**
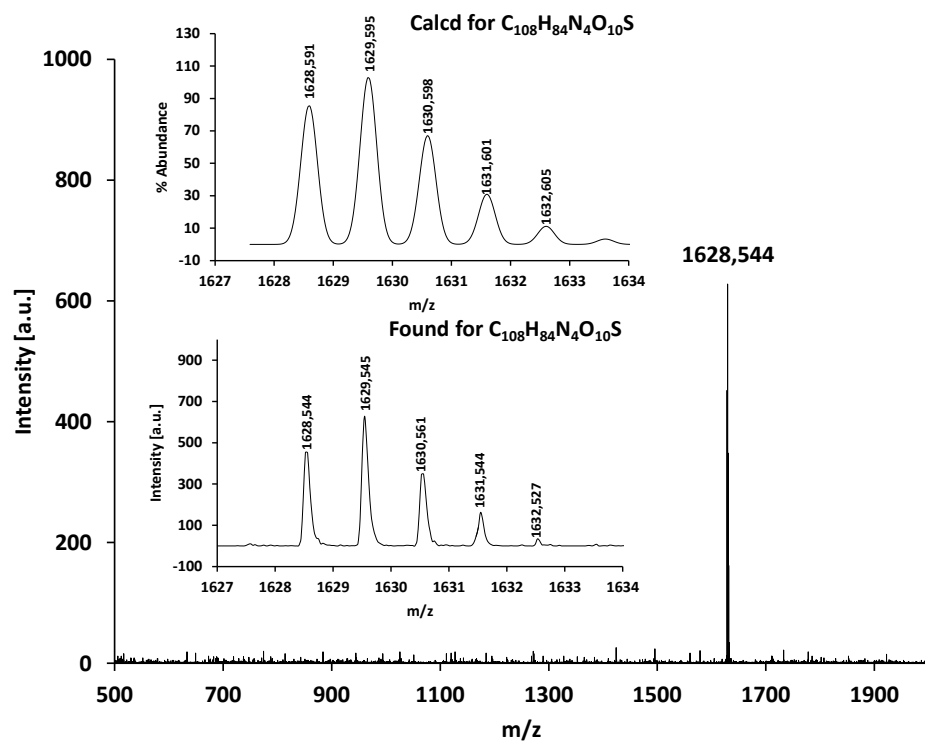
Figure S5. MALDI-TOF spectrum of **PDI 2**.
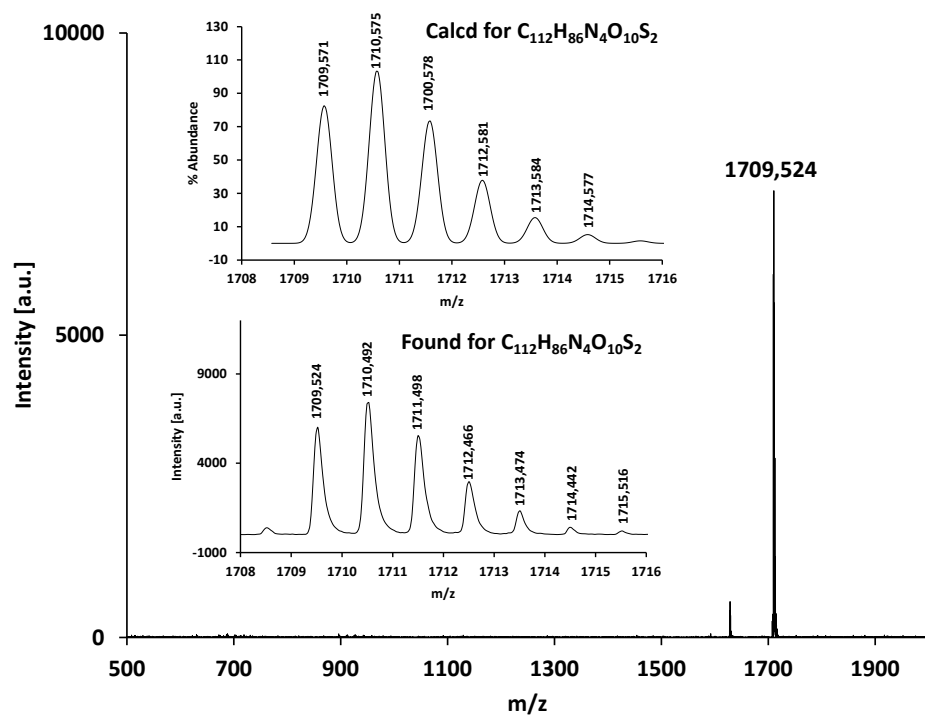
Figure S6. MALDI-TOF spectrum of **PDI 3**.

Solar cell fabrication

$PC_{71}BM$ was purchased from Solenne (Solenne BV, the Netherlands). High purity (HPLC gradient grade, 99.9 %) $CHCl_3$ was used for the active layer deposition. The solvent was dried with activated molecular sieves and kept in a sealed bottle with silver foil prior to use. Aluminium (99.999 %) and LiF (99.995 %) were purchased from Sigma-Aldrich.

Prepatterned Indium Tin Oxide (ITO) 5 Ohm/square (PSiOTec, Ltd., UK) sodalime glass substrates were first rinsed with acetone to remove the residual photoresist layer. The substrates were placed in a teflon holder and sequentially sonicated in acetone (1 × 10 min) and isopropanol (2 × 10 min), and finally dryed under flow of Nitrogen. The ITO substrates where ozone-treated in a UV-ozone cleaner for 30 min in ambient atmosphere, and subsequently coated in air with a layer of filtered (0.45 μm, cellulose acetate) solution of Poly(3,4-ethylenedioxythiophene) : poly(styrenesulfonate) (PEDOT:PSS, HC Starck Baytron P) (4500 rpm 30 seconds followed by 3500 rpm 30 seconds). The PEDOT:PSS film was dried at 120 ºC under inert atmosphere for 15 min. Active layers were spin-coated (1900 to 2600 rpm) in air over the PEDOT:PSS layer from a 25 or 15 mg/ml (total concentration) solution of the PTB7 and the corresponding PDI. The ratio between Donor and acceptor is reported in table S1. The cathode layer was deposited by thermal evaporation in an ultra high vacuum chamber ($1\cdot10^{-6}$ mbar). Metals were evaporated through a shadow mask leading to devices with an area of 9 mm^2. LiF (0.6 nm) and Al (100 nm) were deposited at a rate of 0.1 Å/s and 0.5-1 Å/s respectively.

Following fabrication, the films were maintained under a Nitrogen atmosphere and stored in the dark until used.

Table S1. Active layers deposition parameters

Device active layer	Ratio	Solvent	Conc. (total)	speed (rpm)	DIO (%)
PTB7:PDI 1	1:1	Chloroform	15	1900	0
PTB7:PDI 2	1:1	Chloroform	25	2200	0
PTB7:PDI 3	1:1	Chloroform	25	2600	0

Differential pulse voltammetry

DPV measurements were performed in a conventional three-electrode cell using a µ-AUTOLAB type III potentiostat/galvanostat at 298 K, over $CHCl_3$ and deaerated sample solutions (~0.5 mM), containing 0.10 M tetrabutylammonium hexafluorophosphate (TBAPF$_6$) as supporting electrolyte. A carbon working electrode, Ag/AgNO$_3$ reference electrode and a platinum wire counter electrode were employed. Ferrocene/ferrocenium couple was used as an internal standard for all measurements.
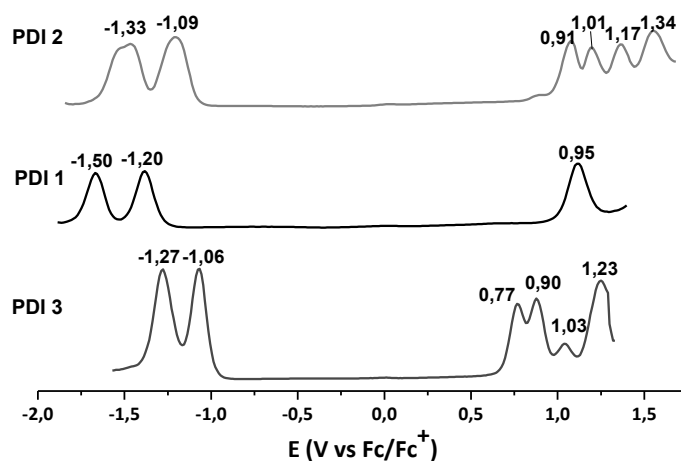
Figure S7. Differential pulse voltammetry of the PDI derivatives, recorded in Chloroform with Ferrocene as internal standard.

Table S2. Summary of the optical features derived from Absorption-emission spectroscopy and cyclic voltammetry.

Derivative	PDI 1	PDI 2	PDI 3
E_{HOMO} (eV)	-5.75	-5.71	-5.57
E_{LUMO} (eV)	-3.55	-3.71	-3.74
Band gap (eV)	2.20	2.00	1.83

Film and device characterisation

The UV-Vis absorption of films was measured using a Shimadzu UV-1700 spectrophotometer. The *J-V* characteristics of the devices were measured in a sealed capsule under inert atmosphere using a Sun 2000 Solar Simulator (150 W, ABET Technologies). The appropriate filters were utilised to faithfully simulate the AM 1.5G spectrum. The illumination intensity was measured to be 100 mW m^2 with a calibrated silicon photodiode (NREL). The applied potential and cell current were measured with a Keithley 2400 digital source meter. The current to voltage (*J–V* curve) was ploted automatically with a home-built Labview© software. The IPCE (Incident Photon to Current conversion Efficiency) was measured using a home made set up consisting of a 150 W Oriel Xenon lamp, a motorized monochromator and a Keithley 2400 digital source meter. The photocurrent and irradiated light intensity were measured simultaneously and processed with a home-built Labview© software.

The thickness of the films was measured with a stylus profilometer Ambios Tech. XP-1, from a scratch made on the film.

AFM and X-Ray diffraction

AFM:

Atomic Force Microscopy (AFM) of the samples was performed in tapping mode on a Molecular Imaging model Pico SPM II (pico +). Images were collected in air using silicon probes with a typical spring constant of 1–5 nN/m and at resonant frequency of 75 kHz.

Table S3. Summary of the roughness values from the AFM topography micrographs from Figure 4.

Image size	PDI1		PDI2		PDI3	
	PEAK TO PEAK	*RMS*	*PEAK TO PEAK*	*RMS*	*PEAK TO PEAK*	*RMS*
1x1 μm	2,86	0,38	3,01	0,39	3,20	0,42
5x5 μm	6,52	0,44	8,38	0,43	4,72	0,44
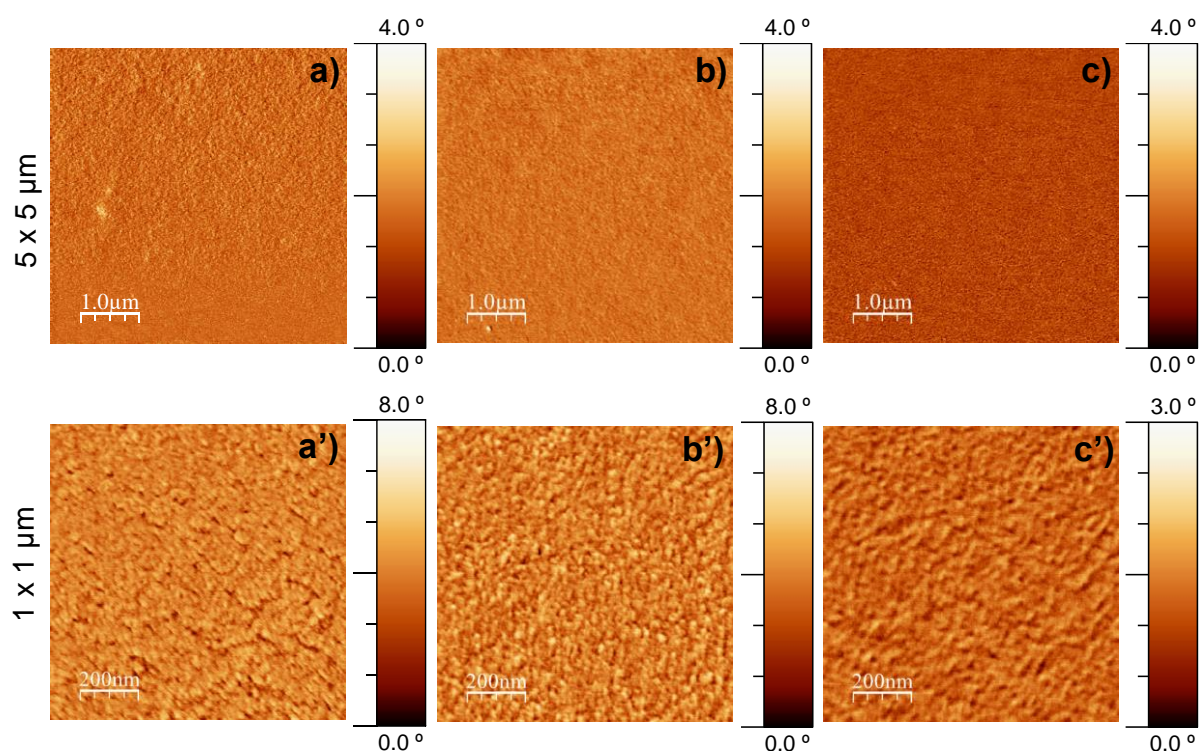
Figure S8. AFM phase images of the active layers made from PTB7 and PDI blends in conditions of optimized solar cell devices. a) and a') PTB7:PDI 1 (1:1); b) and b') PTB7:PDI 2 (1:1); c) and c') PTB7:PDI 3 (1:1).

XRD:

Conventional XRD measurements on thin films were carried out on a Bruker-AXS D8-Discover diffractometer with parallel incident beam (Göbel mirror), a vertical theta-theta goniometer, a XYZ motorized stage mounted on an Eulerian cradle, an incident and diffracted beam Soller slits, a 0.02° receiving slit and a scintillation counter as a detector. Diffraction pattern were recorded over an angular 2theta range of 1° to 15°. The data were collected with an angular step of 0.05° at 10 sec per step. Cuk$_\alpha$ radiation was obtained from a copper X-ray tube operated at 40 kV and 40 mA.

2D XRD measurements were performed with the same diffractometer equipped with an HI-STAR area detector (multiwire proportional counter of 30x30 cm with 1024x1024 pixel) and GADDS software (General Area Diffraction System). Samples were placed directly on the sample holder and the area of interest was selected with the aid of a video-laser focusing system. An X-ray collimator system allows to analyze areas of 500 μm wide. 2D XRD patterns (one frame) were collected covering 1.2-22.3° 2θ from at a distance of 15 cm from the sample. The exposition time was 600 sec per frame.

Figure S9. a) Bragg-Brentano point detector diffractograms of active layers deposited in identical conditions as in optimized OSC devices. Bragg-Brentano point detector diffractograms of of thin films of pristine PDIs acceptors deposited from chloroform (15mL/mg).
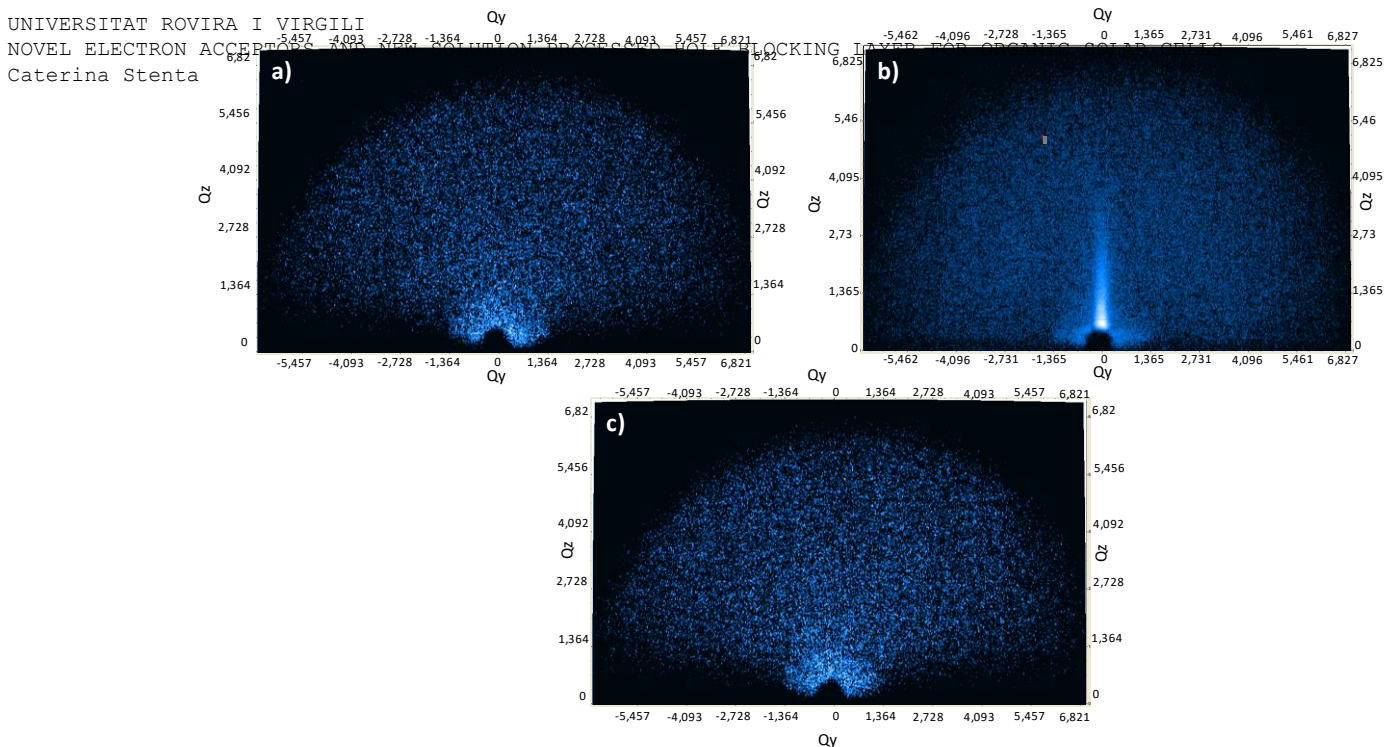
Figure S10. Out of plane GIXRD images of active layers. Recorded at a 30 cm distance from the samples with ω =0.5°, the incident beam angle with respect to the substrate, a) PTB7:PDI 1 b) PTB7:PDI 2 c) PTB7:PDI 3.

Hole and electron mobility:

Mobility measurements were performed using electron only devices which had an ITO/ZnO/PTB7:Azafullerene/Al structure (Figure S11). Thicker metal cathodes (150 nm) were used to aid in cooling to prevent damage associated with device heating when measuring at high voltages. Mobility values were obtained by fitting the obtained J-V plots in the SCLC region to a Mott-Gurney as in equation (1) with the static permittivity of the active layer (ε) fixed to 3, μ_0 being the zero-field mobility.

$$J=9/8 \ (\varepsilon\mu_0)/L^3 \ x \ V^2 \tag{1}$$

Mobility measurements were repeated at least three times (using different devices) to confirm the reproducibility of the results. High electron mobility Zinc Oxide was deposited *via* a sol-gel.
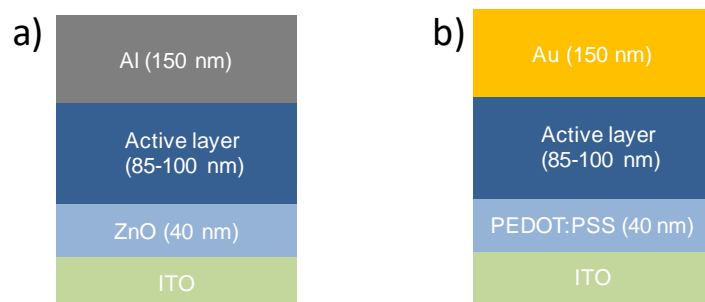
Figure S11. Device architecture used for the electron-only devices.
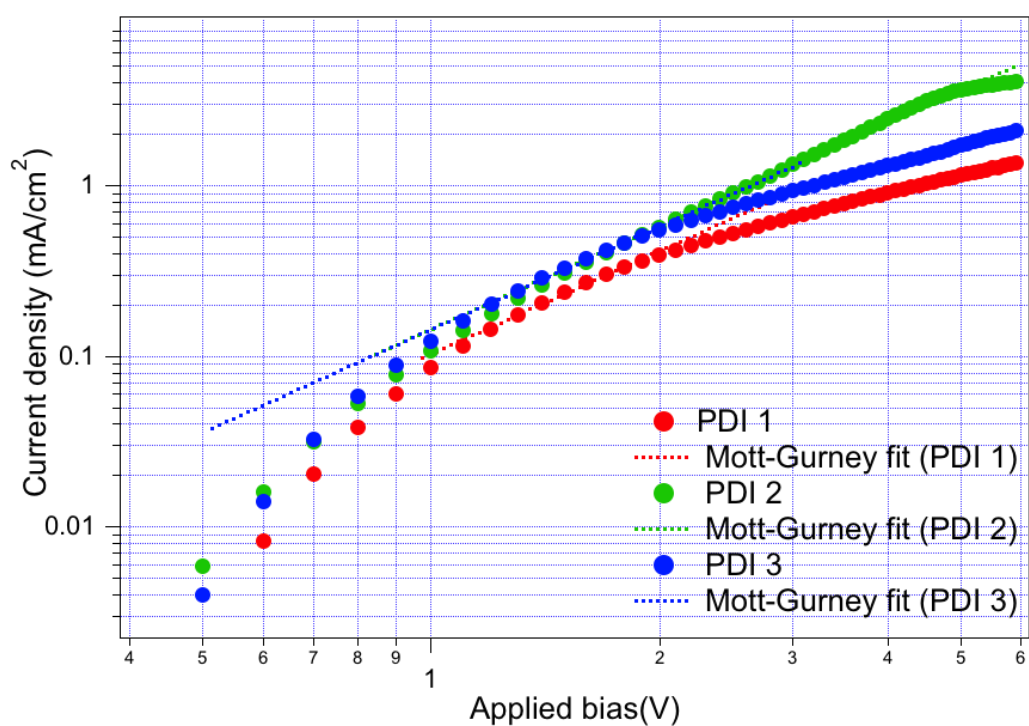
Figure S12. Hole-only devices *J-V* characteristics measured in the dark.
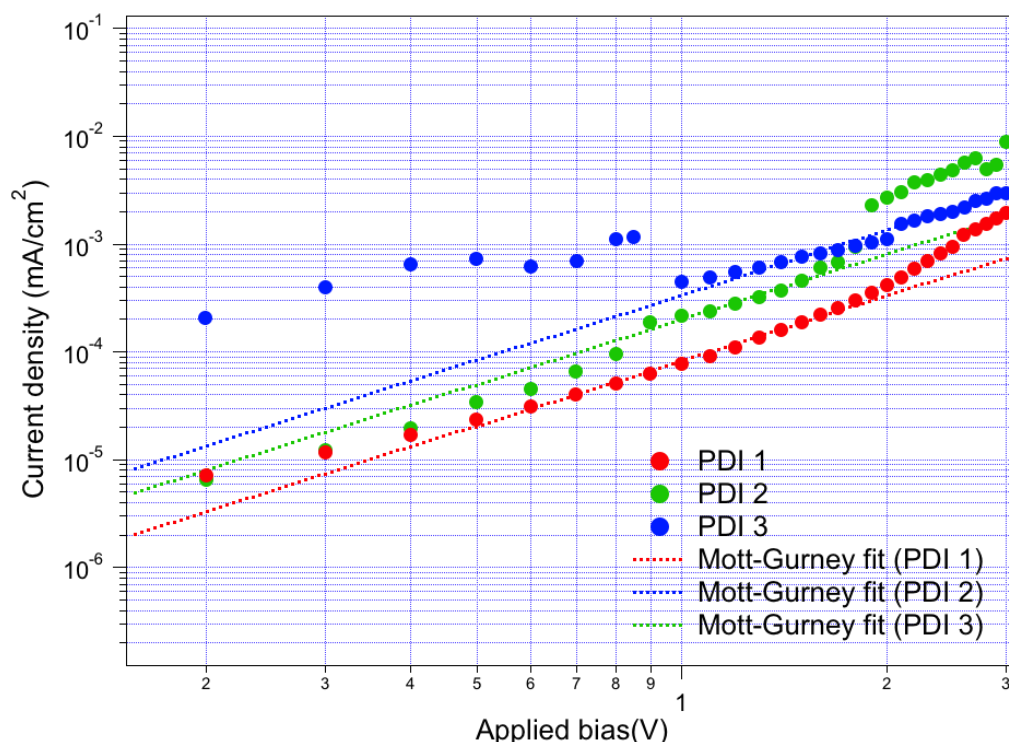
Figure S13. Electron-only devices *J-V* characteristics measured in the dark.

CE/TPV analysis

Charge extraction (CE) was employed to probe the charge density within the active layer of the device under working conditions using a homebuilt system. Devices were held at open circuit by applying bias from a focused array of LEDs. Once the device reached steady state it was then short-circuited with the LEDs switched off simultaneously (switch-off time / relay = 300 ns), leaving the charge stored in the active layer to decay through a small $50 \, \Omega$ resistor. A Yokogawa 2052 digital oscilloscope was used to record the voltage decay across the resistor. Using Ohm's law the voltage transient could be turned into a current transient, which was subsequently integrated to calculate the total charge in the active layer at each light applied bias. In general the device is measured from open circuit voltage values corresponding to >1 Sun conditions to 0 V.

Transient photovoltage (TPV) measurements were carried out on working devices through applying a light bias (the same ring of LEDs used in CE) and holding the device at steady state in open circuit conditions. Once the device reached steady state conditions, a low-

intensity laser pulse (PTI GL-3300 Nitrogen Laser) irradiated the sample to allow a small excess number of charge carriers to be generated. As the device is being held at open-circuit, the excess charge generated has no choice but to recombine. The transient decay of the charge carriers is recorded using a Yokogawa 2052 digital oscilloscope. Sweeping from high-applied bias (high illumination) to low-applied bias (low illumination) allows a correlation between charge carrier lifetime and voltage to be made. The irradiation wavelength was chosen to be close to but not at the maximum of the donor absorption spectrum. A graded neutral density filter was used to control the intensity of the small perturbation, usually keeping the value between 5 and 10 mV.
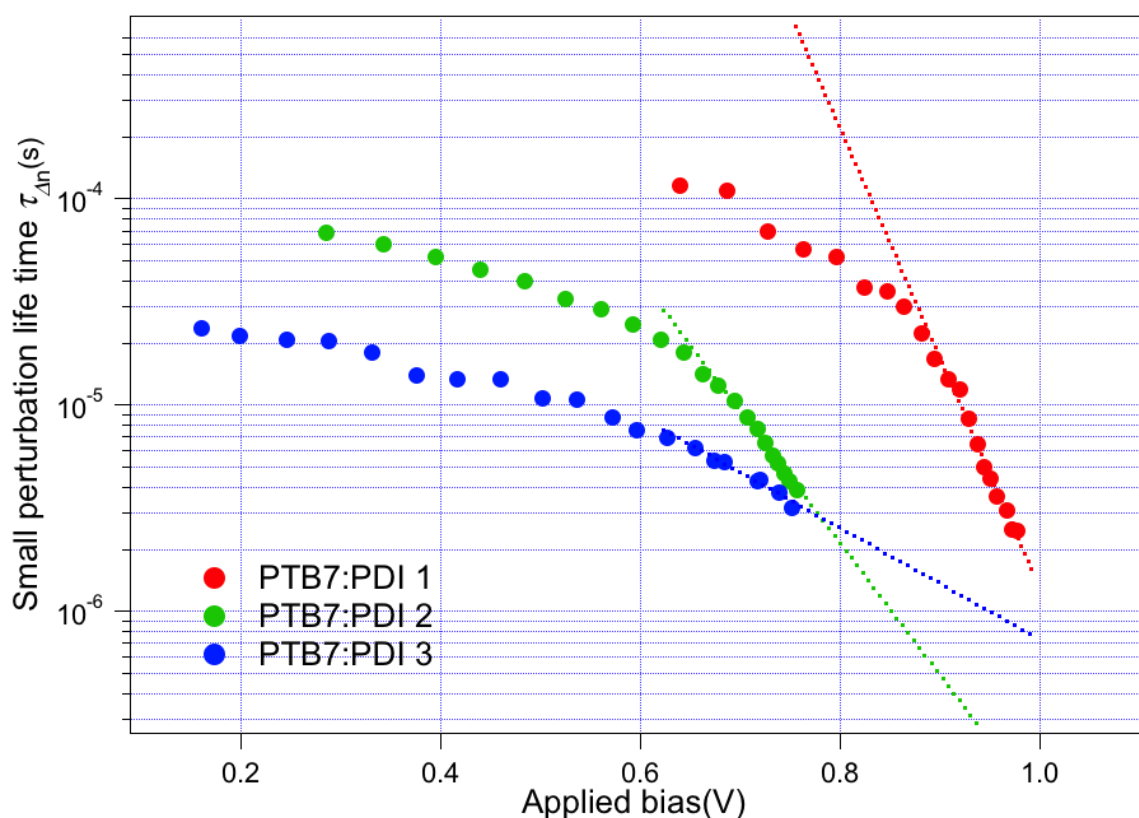
Figure S14. Carriers life time ($\tau\Delta n$) versus open circuit voltage (V_{OC}) plot. Curves are fitted to exponential decays of the form $\tau\Delta n = e^{-\beta V_{oc}}$.

PTB7/PC70BM solar cell
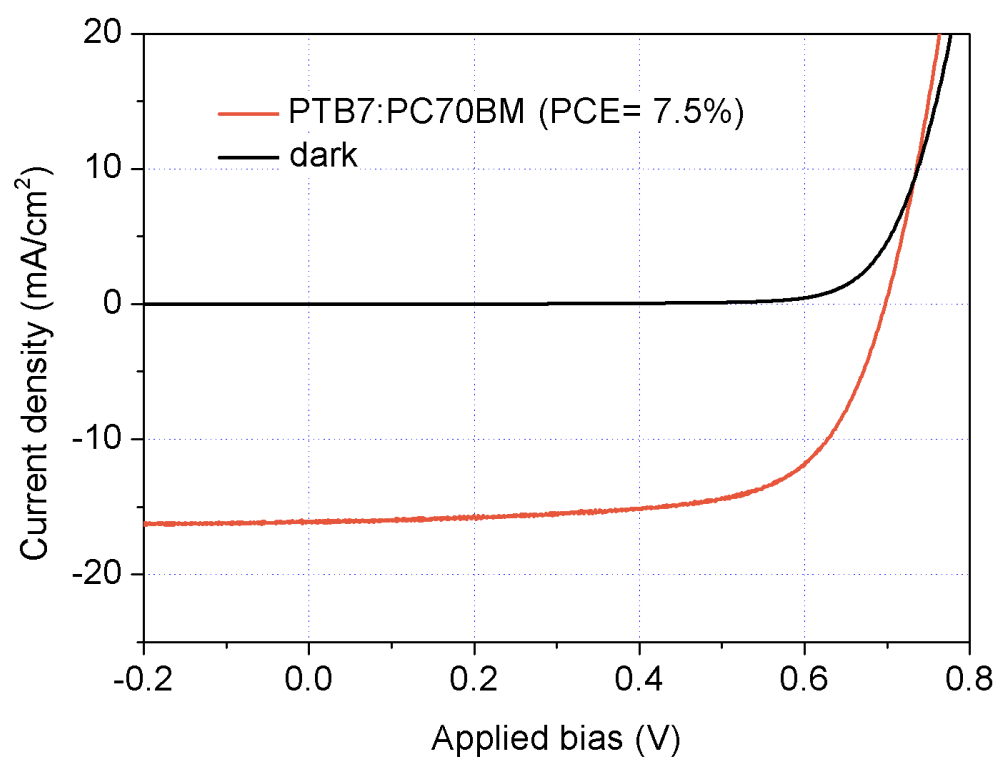
Figure S15: *J-V* characteristics of a typical PTB7:PC70BM solar cells fabricated in identical conditions as those used for PDI-based devices (ITO/PEDOT:PSS/PTB7:PC70BM/Ca/Ag).

Appendix 3

Reproduction of the article

"Understanding the Limiting Factors of Solvent-Annealed Small-Molecule Bulk-Heterojunction Organic Solar Cells from a Chemical Perspective" Daniel Fernandez, Aurelien Viterisi, Vijay Challuri, James W. Ryan, Eugenia Martinez- Ferrero,Francesc Gispert-Guirado, Marta Martinez, Eduardo Escudero, Caterina Stenta,Lluis F. Marsal, Emilio Palomares

Understanding the Limiting Factors of Solvent-Annealed Small-Molecule Bulk-Heterojunction Organic Solar Cells from a Chemical Perspective

Daniel Fernandez,[a] Aurelien Viterisi,*[b] Vijay Challuri,[a] James W. Ryan,[c] Eugenia Martinez-Ferrero,[d] Francesc Gispert-Guirado,[e] Marta Martinez,[a] Eduardo Escudero,[a] Caterina Stenta,[b] Lluis F. Marsal,[b] and Emilio Palomares*[a]

A detailed account of the limiting factors of solvent-annealed bulk-heterojunction small-molecule organic solar cells is given. This account is based on the extensive characterisation of solar cell devices made from a library of five diketopyrolopyrole (DPP) donor dyes. Their chemical structure is designed in such a way as to provide insights into the energetics of solar cell active layer micro-structure formation. Numerous chemical and physical properties of the active layers are assessed and inter-related such as light absorption, molecular packing in the solid state, crystal-forming properties in thin films, charge carrier mobility and charge carrier recombination kinetics. A myriad of characterisation techniques are used such as UV/Vis absorption spectroscopy, photoluminescence spectroscopy, XRD, AFM and photo-induced transient measurements, which provide information on the optical properties of the active layers, morphology and recombination kinetics. Consequently, a mechanism for the solvent-vapour-annealing-assisted formation of crystalline domains of donor molecules in the active layer is proposed, and the micro-structural features are related to the *J*–*V* characteristics of the devices. According to this model, the crystalline phase in which the donor crystallise in the active layer is the key determinant to direct the formation of the micro-structure.

Introduction

Small-molecule semiconductors have attracted increasing interest for bulk-heterojunction (BHJ) solar cell devices. Recent records of power conversion efficiency (PCE) values of over 10% have demonstrated that small molecules (SMs), if designed suitably, can match and even exceed the performance of polymer-based BHJ organic solar cells (OSCs).[1] This is of paramount importance as SMs have the advantage over polymers in that they can be synthesised easily and isolated as discrete entities rather than as poly-disperse mixtures of molecules with various chain lengths. However, the extensive use of polymers in OSCs until recently lies in that they benefit from their long conjugated backbone to pack in an ordered manner, which enhances carrier transport. SMs, however, can only rely on weak inter-molecular interactions to produce highly crystalline active layers. As such, it has been widely demonstrated that even the subtlest change in the molecular structure of a SM donor can influence the performance of SM-BHJ devices greatly, and thus donors with very similar photophysical properties often show very different photovoltaic conversion characteristics.[2–5] Several studies have attempted to draw a trend between the molecular structure of the donor and device characteristics by varying the chemical structure of the donor. Although the change in structure has generally be shown to affect the overall crystallinity of the active layer,[2,5] little is known about the mechanisms that govern crystallite growth in the active layers of SM-BHJ devices and how the resulting nano-/micro-structure limits the overall efficiency of the devices. Consequently, to date, SMs have shown mixed results, and highly efficient SM donors are often discovered serendipitously rather than through rational design. Despite considerable work published on SM-BHJs, no precise relationship has been established between the donor structure and the *J*–*V* characteristics.[6]

[a] Dr. D. Fernandez, Dr. V. Challuri, Dr. M. Martinez, E. Escudero, E. Palomares
Institute of Chemical Research of Catalonia (ICIQ)
Av. Països Catalans, 16, 43007, Tarragona (Spain)
E-mail: epalomares@iciq.es

[b] Dr. A. Viterisi, C. Stenta, Prof. L. F. Marsal
Departament d'Enginyeria Electrònica, Elèctrica i Automàtica
Universitat Rovira i Virgili
Avda. Països Catalans 26, 43007 Tarragona (Spain)
E-mail: aurelien.viterisi@urv.cat

[c] Dr. J. W. Ryan
International Center for Young Scientists (ICYS)
National Institute for Materials Science (NIMS)
1-1 Namiki, Tsukuba, Ibaraki, 305-0044 (Japan)

[d] Dr. E. Martinez-Ferrero
Eurecat Technological Centre
Av. Ernest Lluch, 36, 08302 Mataró (Spain)

[e] Dr. F. Gispert-Guirado
Scientific Resources Service
Universitat Rovira I Virgili
Avda. Països Catalans 26, 43007 Tarragona (Spain)

  Supporting Information and the ORCID identification number(s) for the author(s) of this article can be found under https://doi.org/10.1002/cssc.201700440.

UNIVERSITAT ROVIRA I VIRGILI
NOVEL ELECTRON ACCEPTORS AND NEW SOLUTION PROCESSED HOLE BLOCKING LAYER FOR ORGANIC SOLAR CELLS
Caterina S...

ChemPubSoc
Europe

CHEMSUSCHEM
Full Papers

Therefore, the aim of this study is to design a small library of diketopyrrolopyrole (DPP) derivatives rationally to shine a light on the energetics of micro-structure formation and to demonstrate how the changes induced by the chemical structure of the donor impact all aspects of the *J*–*V* characteristics indirectly in a very significant manner. The donors employed in this study were designed in such way as to induce changes in the morphology of the active layer and to induce as little change as possible in the optical properties [i.e., frontier orbitals (HOMO–LUMO) and band gap energies]. To obtain a better understanding of the key parameters responsible for the device performance and of the evolution of the *J*–*V* characteristics of SM-BHJ devices, the largest possible variables were taken into account. Amongst these variables, band gaps, HOMO–LUMO levels, light absorption, molecular packing in the solid state, crystal-forming properties in thin films, charge carrier mobility and charge carrier recombination kinetics were assessed and inter-related. To provide for the best comparison possible, we based our study on the benchmark 3,6-bis[5-(benzofuran-2-yl)thiophen-2-yl]-2,5-bis(2-ethylhexyl)pyrrolo[3,4-c]pyrrole-1,4(2*H*,5*H*)-dione (DPP(TBFu)$_2$) donor, first described by Walker et al.,[7] which has been characterised extensively previously. The library of donors includes five close parents of the original molecule that comprise the main diketopyrrolopyrrole (DPP) core in their structure with different end groups.

The devices were fabricated as a standard structure; however, a post-active layer deposition solvent vapour annealing (SVA) procedure was applied instead of the common thermal annealing procedure, as SVA provides a better control of the crystallinity of the active layer. In the first instance, the short-circuit current density (J_{SC}) evolution of the devices upon the modification of the chemical structure was related to the absorption properties of the active layer, using the original DPP(TBFu)$_2$ as a reference. This highlighted how parameters, such as the molecular weight, absorption coefficient and active layer thickness, are the major limiters of the J_{SC} (with respect to that of the DPP(TBFu)$_2$ reference).

The open-circuit voltage (V_{OC}) and fill factor (FF) of the devices, and their deviation from the theoretical values expected from the frontier orbital energy levels, were linked to recombination kinetics using a well-established methodology described by Clarke and Durrant in which the V_{OC} is described as a combination of frontier orbital energies and the quasi-Fermi level splitting magnitude that results from non-geminate recombination kinetics.[8]

Finally, all the physical properties of the devices were linked ultimately to the nano-/micro-structure of the active layers and to the arrangement of the molecules in the solid state. XRD, both in Bragg–Brentano and grazing-incidence configurations, is the method of choice to investigate this structure as it provides extensive information on the key parameters that govern device function such as phase segregation, crystalline volume, crystallite size and molecular packing. The results obtained by using XRD and additional microscopy techniques allow us to propose a mechanism for the SVA-assisted formation of crystalline domains of donor molecules in the active layer and to relate these features with the *J*–*V* characteristics of the devices.

Results

The five derivatives were designed as follows: subtle structural changes were introduced in the original DPP(TBFu)$_2$ structure, by first removing the phenyl group of the benzofuran moiety (structure **1**) and substituting the O atom for S (structure **2**)[4, 5] to assess the effect of conjugation length and weak interactions on the solid-state packing. Derivative **3** incorporates a large tetragonal triarylamine group with long alkyl chains with the aim to disrupt π–π stacking interactions in the solid state and to assess their effect on the morphology. Finally, a third class of derivatives incorporate electron-withdrawing groups (**4** and **5**) to assess the effect of weakly polarisable atoms on crystalline growth in the active layers (Figure 1a).

The derivatives were synthesised by two different methods. Compounds **3**, **4** and **5** were synthesised by the Pd-mediated Suzuki coupling of a commercially available dibrominated DPP intermediate, and **1** and **2** were synthesised by the direct alkylation of the respective DPP cores (see the Supporting Information). Importantly, all the derivatives were purified extensively though repeated column chromatography and at least two recrystallisation processes.

Solar cell devices were fabricated using a reported structure (Figure 1b).[9] The active layer was made of a blend of donor derivative and [6,6]-phenyl-C$_{71}$-butyric acid methyl ester (PC$_{70}$BM) dissolved in CHCl$_3$. The active layer of each donor:PC$_{70}$BM blend was deposited by spin coating from CHCl$_3$ and submitted subsequently to a SVA step in CH$_2$Cl$_2$ before the deposition of the cathode (LiF/Al). SVA was chosen over thermal annealing as it has demonstrated a superior ability to control the crystallisation process of these types of donor molecules in SM-BHJ-based devices.[9–13] Devices were optimised with regard to the PC$_{70}$BM:donor ratio, active layer thickness and SVA time (see the Supporting Information).

Photophysical properties

The optical properties of all the donors were characterised by using UV/Vis absorption and emission spectroscopy. HOMO and LUMO energy levels were calculated from the cyclic voltammetry results (see the Supporting Information). The HOMO–LUMO energy levels of each DPP derivative and PC$_{70}$BM are shown in Figure 1a. The donors have a similar band gap of (2.0 ± 0.1) eV. The UV/Vis absorption spectra of all the derivatives show very similar features with maximum absorption in the range of $\lambda = 590$ and 650 nm and onsets of absorption located at approximately $\lambda = 700$ nm, except for **3** the absorption onset of which extends slightly towards the infrared (see Figure S4 for the UV/Vis spectra of all derivatives in solution).

Interestingly, the active layers of all the derivatives show similar features to the original DPP(TBFu)$_2$ donor, that is, three well-defined absorption bands of different relative intensities with the middle band centred at approximately $\lambda = 600$ nm (Figure 2a). The relative intensity of these bands changes significantly upon SVA for DPP(TBFu)$_2$, a trend attributed previously to an increase in aggregation that is followed by all de-
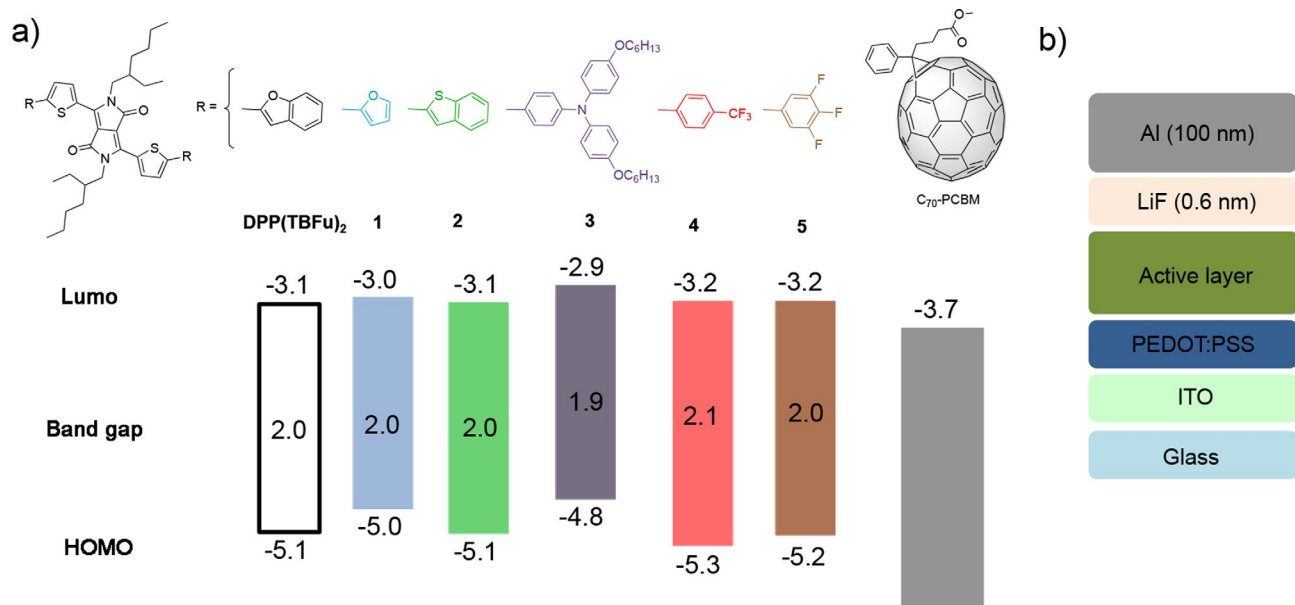
Figure 1. a) Chemical structure of DPP derivatives and their HOMO–LUMO and band gap energy derived from cyclic voltammetry measurements and UV/Vis/emission measurements. The LUMO and band gap of PC$_{70}$BM measured under the same conditions is shown for comparison. b) Solar cell architecture used in this study.

rivatives (Figure 2b).[9] Derivatives **1** and **4** show a similar increase of the blue-shifted bands, presumably caused by the formation of a similar type of aggregates. Derivatives **2**, **3** and **4** display less significant changes upon annealing. Contrary to the other derivatives, the intensity of the absorption band in the annealed active layer films remains similar to but significantly sharper than that of the non-annealed films. Such changes in the absorption properties in the films induce a noticeable colour change particularly for derivatives **2**, **4** and **5**. It is important to note the very significant change in the absorption intensity between the active layers, the effect of which is of importance to limit the J_{SC} of the working devices. A quantification of the effect of the absorption of the active layer on the J_{SC} of the devices is provided in the next section.

Photovoltaic properties

Solar cell devices were fabricated in an identical structure for all the DPP derivatives (ITO/PEDOT:PSS/DPP:PC$_{70}$BMLiF/Al; Figure 1b). The donor/acceptor (D/A) ratio, active layer thickness and solvent annealing time were optimised for each device. The evolution of the J–V characteristics of the devices upon solvent annealing follows a similar trend as observed previously with DPP(TBFu)$_2$, in which J_{SC} increases with the annealing time up to a maximum value and decreases with a longer annealing time.[9,12] Concomitant with this decrease of J_{SC}, an increase in the FF is usually observed. Notably, the FFs are fairly low in all of the optimised devices with values of 40–55%. However, devices made from derivative **2**, similar to DPP(TBFu)$_2$,[9] show an improvement of the FF to 66% if longer
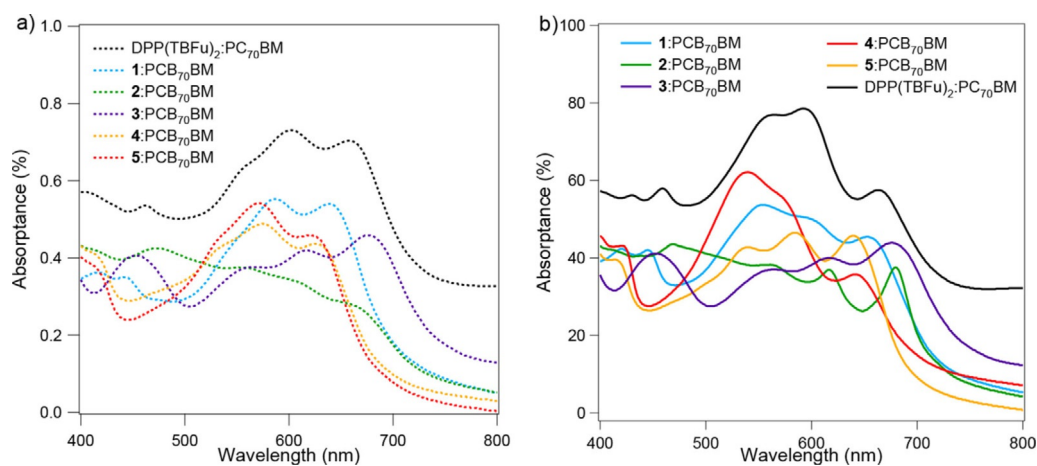
Figure 2. UV/Vis absorption spectra of active layers made of the DPP derivative and PC$_{70}$BM blends under optimum device conditions. a) Non-annealed films, b) CH$_2$Cl$_2$-SVA films.

UNIVERSITAT ROVIRA I VIRGILI
NOVEL ELECTRON ACCEPTORS AND NEW SOLUTION PROCESSED HOLE BLOCKING LAYER FOR ORGANIC SOLAR CELLS
Caterina Stenta

ChemPubSoc
Europe

CHEMSUSCHEM
Full Papers

annealing times were applied. This is not without a very significant decrease in J_{SC}, which brings the overall efficiency well below 1%. Interestingly, the V_{OC} of the devices does not follow a trend and does not relate accurately to the HOMO levels of the derivatives (see Table 3 for experimental and theoretical V_{OC} values).[14] The J_{SC} values range from 1 to almost 5 mA cm^{-2} for the new derivatives, which is lower than the 9 mA cm^{-2} obtained with the commercial DPP(TBFu)$_2$ reference donor. The J_{SC} values are corroborated by the external quantum efficiency (EQE) measurements (Figure 3).

A comparison of the optical parameters of the active layers is presented in Table 1. This provides an estimation of the fraction of the losses in J_{SC} that are related directly to the absorption of the active layers.

On the basis of a seminal study from Heeger and co-workers,[15] we reasoned that if the active layers experience similar D/A electron transfer kinetics and geminate recombination kinetics (the dominant loss mechanisms at short circuit) to the reference DPP(TBFu)$_2$ blend, the J_{SC} would be proportional to the fraction of the active layer absorption integral in the visible range. To test this, the absorptance[16] spectra of all the active layers were integrated with respect to the wavelength (400–900 nm). Accordingly, the integrated value of the absorptance for optimised active layers (column 6) and their percentage value with respect to the DPP(TBFu)$_2$ reference active layer (column 7) are shown in Table . The theoretical J_{SC}, which corre-

sponds to the highest attainable J_{SC} based on the absorption capacity of the active layers, is equivalent to the percentage fraction of the J_{SC} of the DPP(TBu)$_2$ device (column 9). Consequently, the experimental J_{SC} values of devices made from derivatives **1** and **3** are consistent with that calculated from the absorption integral of their respective active layers. The J_{SC} values of devices of derivatives **2**, **4** and **5** are, however, not consistent with the calculated value.

To understand the origin of such a discrepancy, relative internal quantum efficiency (rIQE) values were measured to approximate the efficiency with which each active layer converts photons into electrical charges.[17] Devices of derivatives **1** and **3** show a similar overall value of rIQE to that of the reference DPP(TBFu)$_2$ device ($\approx 70\%$ on average), which implies that all three active layers convert photons to free charge carriers with comparable efficiencies (Figure 4). This confirms that the J_{SC} produced by derivatives **1** and **3** is limited mostly by the absorption ability of the active layers relative to the DPP(TBFu)$_2$ reference. The difference between the calculated and experimental J_{SC} could be attributed to a slight difference in geminate recombination kinetics and exciton diffusion length with respect to the reference DPP(TBFu)$_2$ device. However, derivatives **4** and **5** show a much lower rIQE than the other derivatives, which corroborates the larger differences in the experimental and theoretical J_{SC} values (Table 1). Additional losses must be responsible for the lower experimental J_{SC} than ex-
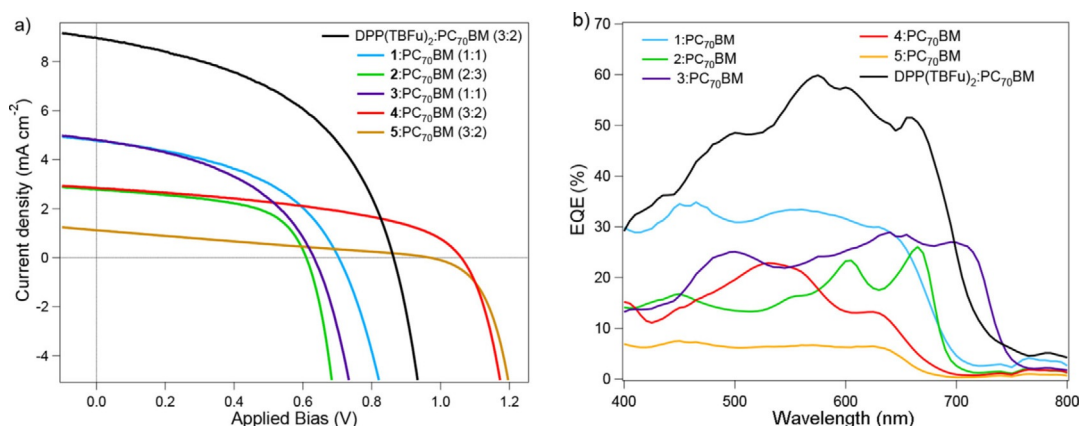
Figure 3. a) *J–V* characteristics of solar cell devices fabricated with DPP-series donors and PC$_{70}$BM. These curves represent the average performance of devices made under the optimised conditions. b) Corresponding EQE spectra.

Table 1. Properties of DPP derivatives in solution, properties of the active layers made from derivative:PC$_{70}$BM blends under conditions optimised for the solar cell devices. <

Derivative	D/A ratio	Annealing time [min]	Absorption coefficient [L mol^{-1} cm^{-1}]	Active layer thickness [nm]	Integrated area[a] (absorptance)	Percentage[b] with respect to DPP	J_{SC} [mA cm^{-2}] theoretical	experimental
1	**1:1**	1	55 220 ± 394	110	138	63	5.7	4.8
2	**2:3**	1.25	49 825 ± 625	85	120	55	4.9	2.8
3	**1:1**	4	96 617 ± 717	95	129	59	5.3	4.8
4	**3:2**	6	49 240 ± 315	95	130	60	5.3	2.8
5	**3:2**	1.5	20 869 ± 305	80	110	50	4.5	1.1
DPP(TBFu)2	**3:2**	1	65 964 ± 301	75	218	100	9.0	9.0

[a] Integrated area of the absorptance spectra. [b] Percentage fraction of the absorptance spectra's integrated area with respect to that of DPP(TBFu)$_2$.

ChemPubSoc
Europe

CHEMSUSCHEM
Full Papers
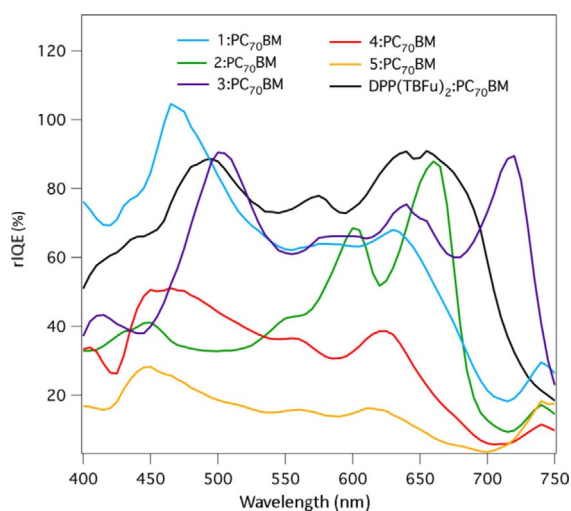
Figure 4. rIQE spectra of devices made with the DPP derivatives. The rIQE spectra were calculated from the EQE and absorptance spectra of the devices as rIQE = EQE/absorptance.

pected from the absorption properties of the active layer. Derivative **2** shows an intermediate behaviour in which the rIQE reaches that of the reference DPP(TBFu)$_2$ device at two wavelengths (600 and 660 nm) but decreases below 50% rIQE for the rest of the spectrum.

Consequently, these results indicate that a large part of the losses in J_{SC} compared to that of DPP(TBFu)$_2$ are caused by the poorer absorption capability of the active layers. However, the absorption of the active layers cannot be related directly to the chemical structure of the donors. Indeed, the absorption coefficients (molar absorptivity) of donors **1**, **2** and **4** are situated in a similar range to that of DPP(TBFu)$_2$, which gives these donors an almost identical absorption capability as the reference DPP(TBFu)$_2$ in solar cell devices. The absorbance of the active layer is limited, to a significant extent, by the active layer thickness (Table 1)[18] and, indirectly, by the molar ratio in the blend composition. The latter statement is exemplified by donor **3**, which has a molecular weight that is approximately double that of DPP(TBFu)$_2$. Indeed, despite its higher absorption coefficient, **3** makes up a smaller percentage of the blend composition compared to DPP(TBFu)$_2$ as seen by the D/A molar ratio, which shows that **3** provides less absorption in the active layer than DPP(TBFu)$_2$.

Morphological characterisation

The optimum active layer thickness relies on obtaining the best trade off between charge generation (maximisation of the thickness for complete photon absorption) and charge extraction (to ensure all charges generated percolate to the contacts). Although these two parameters are often seen as two separate physical properties, we demonstrate herein that they are inter-related. That is, if the charge extraction properties are determined by morphological parameters (phase segregation, D–A interfacial area and crystallinity of the active layer in a broad sense), the resulting morphology will lead indirectly to

a limit of the active layer thickness. The molecular structure of the donor and the manner of which it arranges in the solid state will dictate the morphology of the active layer. These features will be described in the sections below, however, the formation of the D–A interface is a parameter that can be monitored qualitatively by using photoluminescence (PL) spectroscopy.[8] The PL spectra of active layer films of the donor:PC$_{70}$BM blends deposited on quartz substrates using the same conditions as those used for the fabrication of OSC devices are shown in Figure 5. A relative increase in emission is observed
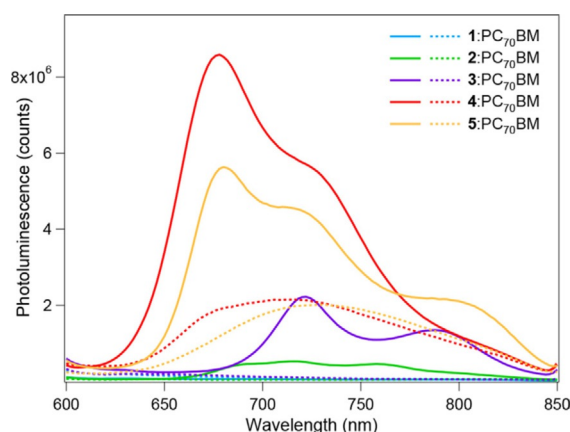
Figure 5. PL spectra of active layers made of DPP derivatives and PC$_{70}$BM. The spectra of the non-annealed layers are shown in dotted lines, and those of the annealed active layers are in solid lines.

in most cases upon annealing, which is indicative of the formation of segregated donor and acceptor domains and, therefore, of a modification of the D–A interfacial area. Although quantification between blends is not possible, both fluorinated derivatives **4** and **5** show a significant PL intensity even if the layers are not annealed, which indicates that there is some type of segregation present in the non-annealed state. Importantly, the very significant increase in the PL of the active layers of derivatives **4** and **5** is consistent with the lower than expected J_{SC} (vide supra) in working devices. Indeed, the extent of phase segregation is presumably overwhelming and diminishes the exciton separation yield (excitons do no reach the interface; see the Discussion).

In SM-BHJ, phase segregation, and therefore, the formation of the D/A area, results from the growth of crystallites of donors in the active layers. The extent of crystalline growth (size, shape and quantity of crystallites) determines the performance of the devices strongly. To measure the values of these parameters, we performed an extensive crystallographic characterisation. As such, conventional XRD and grazing-incidence X-ray diffraction (GIXRD) measurements were performed on the active layers of each donor:PC$_{70}$BM blend. First, conventional diffractograms in the Bragg–Brentano configuration were recorded in the out-of-plane direction. The diffractograms of each DPP:PCBM active layer with a) no annealing, b) solvent annealed using the same conditions as their respective device and c) solvent annealed for 10 min (considerably longer than

the optimum annealing time) are presented in Figure 6. All donors show a propensity to form crystalline domains upon annealing, as seen by the presence of a diffraction peak at a low 2θ angle for all the annealed layers and an additional weak peak from the same family of diffraction plane in the case of derivative **3**. These peaks at small 2θ values are characteristic of pure DPP donor crystallites and,[2f,5,9,19] as demonstrated previously, cannot be attributed to $PC_{70}BM$ crystallites. Although PCBM has been shown to form crystalline domains in some solvent-annealed active layers,[13] those domains were extremely small (<2 nm) and PCBM generally remains amorphous in blends of SM-BHJ solvent-annealed active layers, at least under our measurement conditions (low-energy X-ray incident beam).[9] The shape and size of the diffraction peaks, however, indicate different crystallisation kinetics between the donors. Scherer analysis (see Supporting Information for details) of the full width at half maximum (FWHM) of the peaks revealed that donors **3** and **4** have the ability to grow crystallites of a considerably greater size, at least in the out-of-plane direction, with respect to the other derivatives. The greatest at-

tainable crystallite size (after 10 min annealing) in the active layers of **3** and **4** is in the same range as the layer thickness (67 and 90 nm, respectively), whereas it is in the range of 10 nm for derivatives **1**, **2** and **5**. In most cases both the size of the crystallites (given by the FWHM) and the total crystalline volume (given by the integral area of the peak) is seen to increase with annealing time as observed previously in SM-BHJ devices.[9, 12] However, the increase is almost insignificant in the case of derivatives **2** and **5**. Derivative **1** is the only derivative that shows the opposite trend on the size evolution of the crystallites over the annealing time,[20] however, the crystalline volume is seen to increase greatly upon longer annealing times.

Additional 2 D diffraction patterns recorded in GIXRD mode reveal that the crystallites have a high degree of orientation with respect to the substrate surface as seen by the presence of very narrow diffraction rings (Figure 7). Derivative **3** shows the lowest degree of texture, whereas all the other derivatives are highly oriented. Additionally, we can extrapolate that crystallites of derivatives **2** and **4** have an extremely high degree
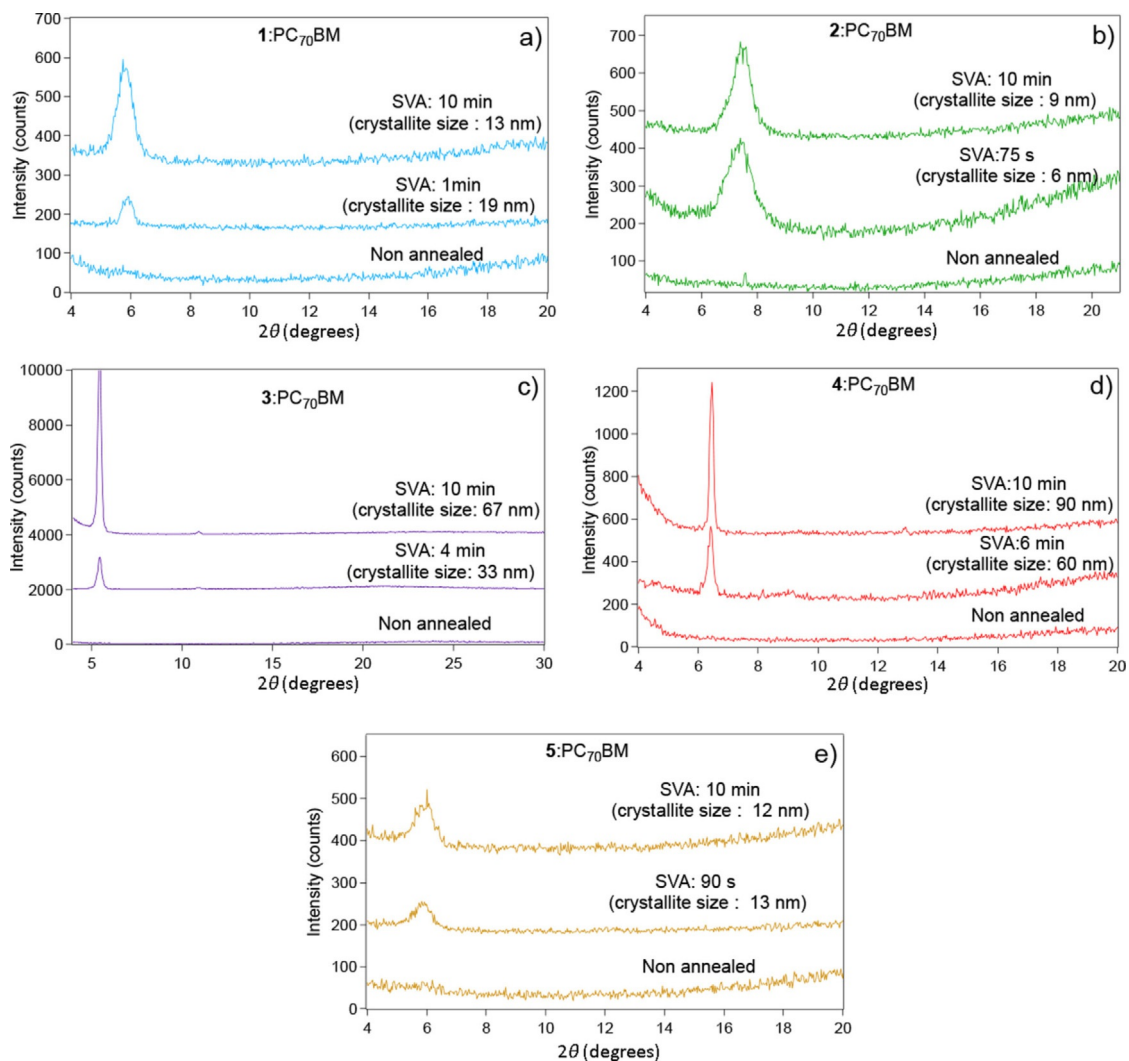
Figure 6. Bragg–Brentano point detector diffractograms of SVA (CH_2Cl_2) and non-annealed active layers.
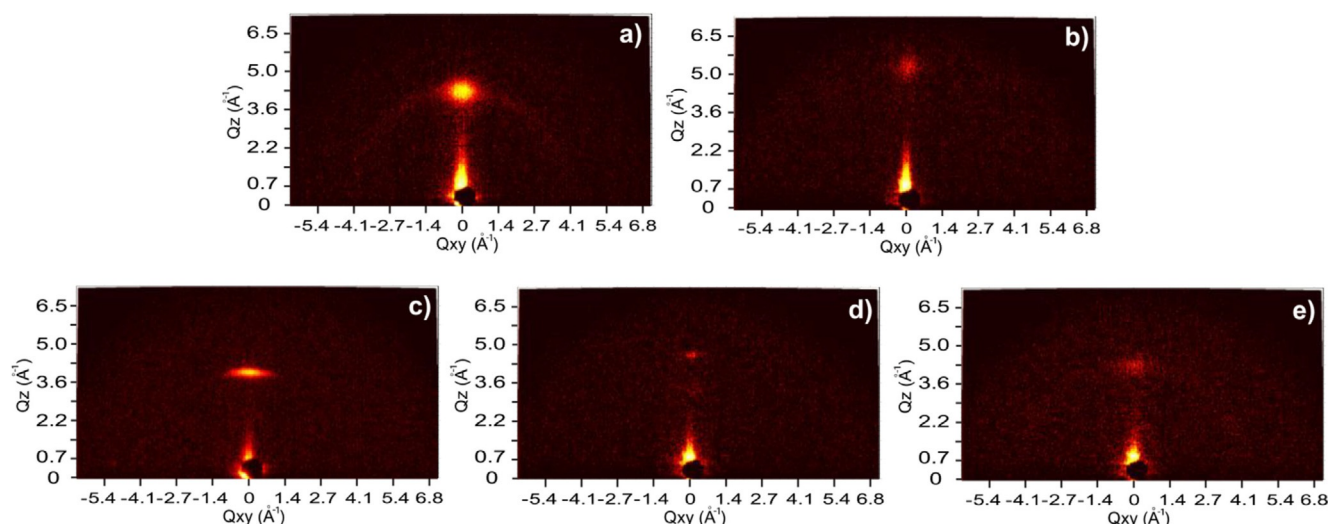
Figure 7. Out-of-plane GIXRD images of active layers. Recorded at a 30 cm distance from the sample with $\omega = 0.5°$ as the incident beam angle with respect to the substrate: a) **1**:PC$_{70}$BM, b) **2**:PC$_{70}$BM, c) **3**:PC$_{70}$BM, d) **4**:PC$_{70}$BM, e) **5**:PC$_{70}$BM.

of orientation, in the out-of-plane direction (Q_z) as well, as seen by the apparent weak signal intensity at lower grazing angles compared to that of the specular (θ–θ) 1D diffracto-grams. Additional GIXRD patterns (Figure S11) further demonstrate this as the intensity of the diffraction spot increases sharply at higher grazing angles.[21]

To gain additional evidence on the distribution and shape of the crystallites, AFM analysis of the active layers was performed. Images were recorded of as-cast and of annealed active layers from optimised devices. First, the change of morphology, derived from the root mean squared (RMS) roughness between the non-annealed and annealed devices confirms the trend observed by using XRD. That is, an increase in roughness upon SVA, characteristic of crystallite growth within the active layer,[9,11,12] is observed for active layers of derivatives **1**, **2** and **3** (Figures 8 and 9). In the case of derivatives **4** and **5**, the non-annealed active layers show an unexpectedly high overall roughness value and a granular relief pattern, which likely stem from the fast drying conditions of the spin coating pro-

cess. The domains remain amorphous as seen in the XRD diffractograms, however, the strong contrast difference in the phase images (Figure 8 i and j) suggests that the granular pattern is consistent with segregated domains of donor and acceptor materials. This further confirms the unusually high PL emission intensity of non-annealed active layers of **4** and **5** (Figure 4).

Upon the exposure of the active layers to solvent vapour of CH_2Cl_2, a clear change is noticed in the topography images consistent with the XRD measurements in which donor molecules are seen to rearrange into pure crystalline donor domains.

This rearrangement of donor molecules into crystalline domains is seen to occur in most active layers but leads to very different morphologies. Notably, derivatives **4** and **5**, although they have similar chemical structures, have a very different impact on crystal growth. The unusual formation of micrometre-size sheet-like domains attributed to crystalline domains of pristine donor can be seen in Figure 9 d. The crystalline nature
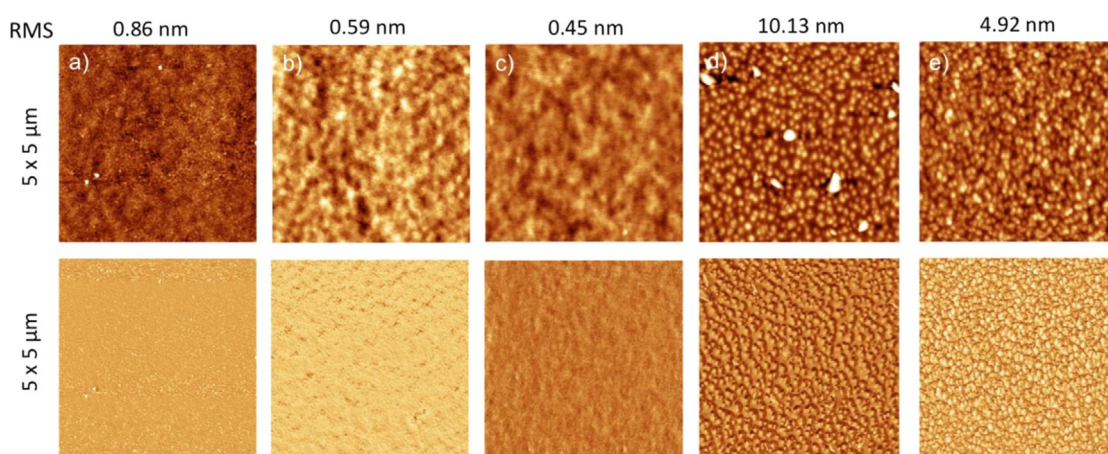
Figure 8. AFM topography (top) and phase (bottom) images of non-annealed active layers of devices made from each donor derivative: a) **1**:PC$_{70}$BM, b) **2**:PC$_{70}$BM, c) **3**:PC$_{70}$BM, d) **4**:PC$_{70}$BM, e) **5**:PC$_{70}$BM. The RMS roughness value for each film is given above its respective topography.

ChemPubSoc
Europe

CHEM**SUS**CHEM
Full Papers
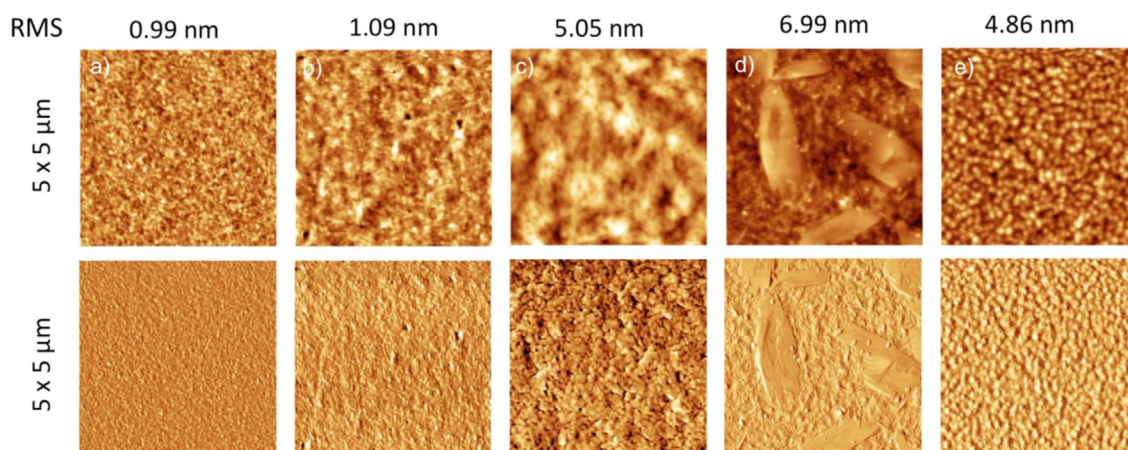
Figure 9. AFM topography (top) and phase (bottom) images of annealed active layers of devices made from each donor derivative: a) **1**:PC$_{70}$BM, b) **2**:PC$_{70}$BM, c) **3**:PC$_{70}$BM, d) **4**:PC$_{70}$BM, e) **5**:PC$_{70}$BM. The RMS roughness values for each film are given above its respective topography.

of the domains is deduced from the XRD data, whereas the size of the crystallites observed on the micrographs is consistent with the size calculated by using XRD in the out-of-plane direction (in the order of magnitude of the active layer's thickness). The contrast difference in the AFM phase image confirms the pristine nature of the crystallites (Figure 9d, bottom image). Moreover, the orientation of the crystallites with respect to the substrate normal is consistent with the low intensity of the diffraction spot in the GIXRD images at lower grazing angles (Figure 7d). Conversely, the fluorinated analogue **5** shows no clear morphological change upon SVA, neither by using AFM or XRD, and shows a very limited crystalline volume as seen by the weak diffraction peak in Figure 6e. The case of derivatives **1**, **2** and **3** is rather different from that of the fluorinated derivatives. Derivatives **1** and **2**, although they form crystallites of a moderate size, as seen by using XRD, show a homogenous distribution within the active layer. Crystallites are presumably embedded in the donor/PC$_{70}$BM amorphous fraction as demonstrated by the featureless phase images (Figure 9a and b, bottom images). Films of derivative **3** show a much higher roughness than films of **1** and **2** consistent with the presence of larger crystallites as measured by using XRD. The difference in behaviour towards crystallite growth between the different derivatives is rationalised in the section on crystallite growth and in the Discussion.

Molecular packing in donor crystallites

If we used conventional XRD and GIXRD measurements in combination with AFM images we could obtain a detailed understanding of the active layer morphology at the nanoscopic scale and gain some insights into the kinetics of SM donor crystallisation in the blended films. Although the above morphological features are important to understand the formation of the D–A interface and charge transport, the actual arrangement of the donor molecules in the crystallite is determinant to enhance the hole mobility. The characterisation of such an arrangement (the crystalline phase in which the donor packs)

has been performed rarely because of the limitation imposed by the nanoscopic scale of the crystallites. Previously, we reported a method that allows for the accurate characterisation of the crystalline phase of crystallites that form the active layer. It relies on the comparison of diffractograms of "powdered" active layers with single-crystal structures obtained from their respective donor.[22] The powdered active layer method consists of the deposition of active layers on large-area glass substrates, annealing them for an extended period of time to promote crystalline growth and recording a powder diffractogram (transmission Bragg–Brentano geometry) of the solid that results from scrapping off the film, hence a powdered film. This allows us to determine the crystalline phase in which the donors are packed in thin films accurately because of the higher amount of peaks present in the diffractogram with respect to that if a diffractogram is recorded directly from the film on the substrate. The lack of diffraction peaks in the latter case is both the result of the limited crystallite size and the high degree of texture (orientated crystalline domains). The crystalline phase assignment, which relies on diffractogram comparison using least-square profile refinement routines, confirmed that molecules of derivatives **1** and **2** pack in crystalline domains of active layers in the same crystalline phases as that of their respective single crystals. The calculated diffractograms of the corresponding single-crystal structures fit well to allow unambiguous phase assignment (Figures 10 and 11).

Contrary to that of **1** and **2**, the diffractograms of powdered active layers of derivatives **3**, **4** and **5** did not match those calculated from their respective single-crystal data. This confirms that, in active layers, the donors crystallise in a different phase than that of the single crystal (Figure S14). Although single crystals of each donor were grown under a range of different conditions to obtain as many polymorphic structures as possible for each derivative, no additional polymorph that could provide for a better match was obtained. Nonetheless, the above analysis for derivatives **1** and **2** combined with the GIXRD data led to the deduction that crystallites of derivative **1** are oriented with their (0 0 1) diffraction plane (from the $P\bar{1}$
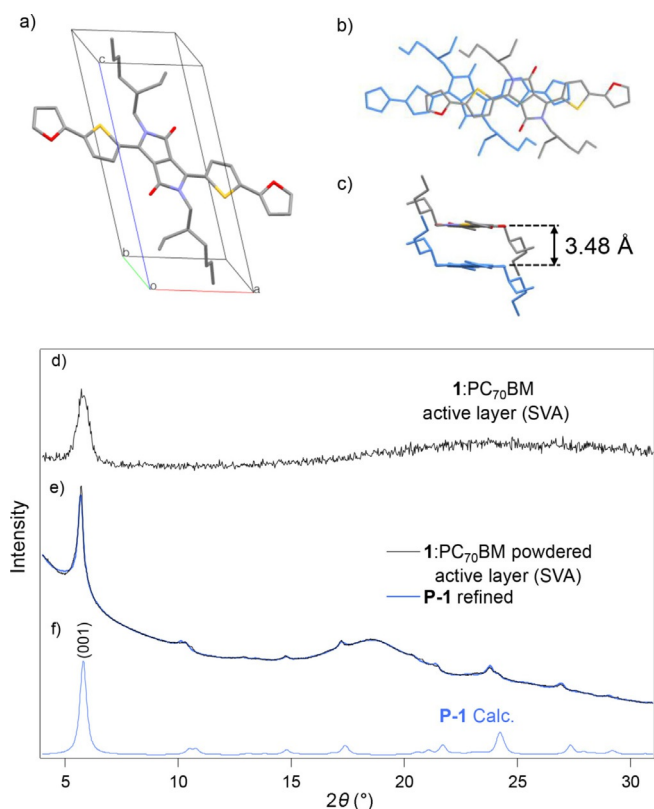
Figure 10. X-ray crystal structure of **1**; Space group $P\bar{1}$. a) Unit cell depicted for the side view of the (001) plane. b) Top and c) side view of the molecule stacks. d) active layer point detector diffractogram, e) diffractogram of the powdered active layer and superimposed refined diffractogram from the single-crystal XRD structure, f) calculated diffractogram (at 100 K) from the single-crystal XRD structure.

Figure 11. X-ray crystal structure of **2** (H atoms omitted for clarity); Space group $P2_1/c$. a) Unit cell depicted for the side view of the (020) plane. b) Top and c) side view of the molecule stacks. d) active layer point detector diffractogram, e) diffractogram of the powdered active layer and superimposed refined diffractogram from the single-crystal XRD structure, f) calculated diffractogram (at 100 K) from the single-crystal XRD structure.

phase) parallel to the substrate surface (Figure 10 a). The same analysis applies to derivative **2**, which is oriented with its (020) plane parallel to the substrate surface (Figure 11 a). Importantly, the profile refinement of diffractograms from the powdered film of derivative **2** required the addition of anisotropic peak broadening parameters to provide a better profile shape refinement (see the Supporting Information for details). This resulted in the assumption that the crystallites of **2** grow with unit cell parameters *b* and *c* that are significantly larger than *a*. The implications of this feature will be expanded on in the Discussion. The main morphological features derived from the XRD and AFM measurements are illustrated in Figure 12.

Crystallite growth

The mechanism of crystal formation in SM-BHJ has, to the best of our knowledge, not yet been studied in detail. Although some studies have drawn parallels between polymers and SMs it is very unlikely that crystallites form by similar mechanisms. Indeed, phase segregation in some polymer-PC$_{70}$BM has been suggested to occur through a spinodal decomposition (demixing) mechanism;[24–27] however, the poorly inter-mixed morphologies (largely segregated) formed in some of our solvent-vapour-annealed SM-PCBM active layers (especially **3** and **4**)

suggest a different crystallite growth mechanism. Spinodal decomposition may occur with SM-based blends in the early stages of active layer drying during spin coating to result in uniformly segregated but amorphous domains of the donor and acceptor, as exemplified by non-annealed active layers of **4** and **5** (see AFM images in Figure 8).[27,28] The low miscibility of the donors with the fullerene is presumably enhanced by the F atoms of **4** and **5** and allow the system to enter a spinodal region under the fast drying conditions of the spin coating process. In the subsequent SVA step, the crystallisation of donor molecules from the amorphous active layer would then occur by a homogeneous or heterogeneous[29,30] nucleation and growth mechanism as suggested previously.[25]

The free energy change for a homogenous process that implies spherical nuclei of radius *r* is described by Equation (1).

$$\Delta G(r) = \frac{1}{3}\pi r^3 \Delta G_V + \frac{4}{3}\pi r^3 \Delta G_E + 4\pi r^2 \gamma \tag{1}$$

Accordingly, $\Delta G(r)$ depends on three energy parameters: ΔG_V, which corresponds to the bulk free energy difference of crystal formation [energy/unit volume] intrinsic to each polymorphic crystalline phase, γ, which corresponds to the interfacial energy (i.e., the energy that arises from the interface between the nucleus composed of pure donor molecules and

CHEM**SUS**CHEM
Full Papers
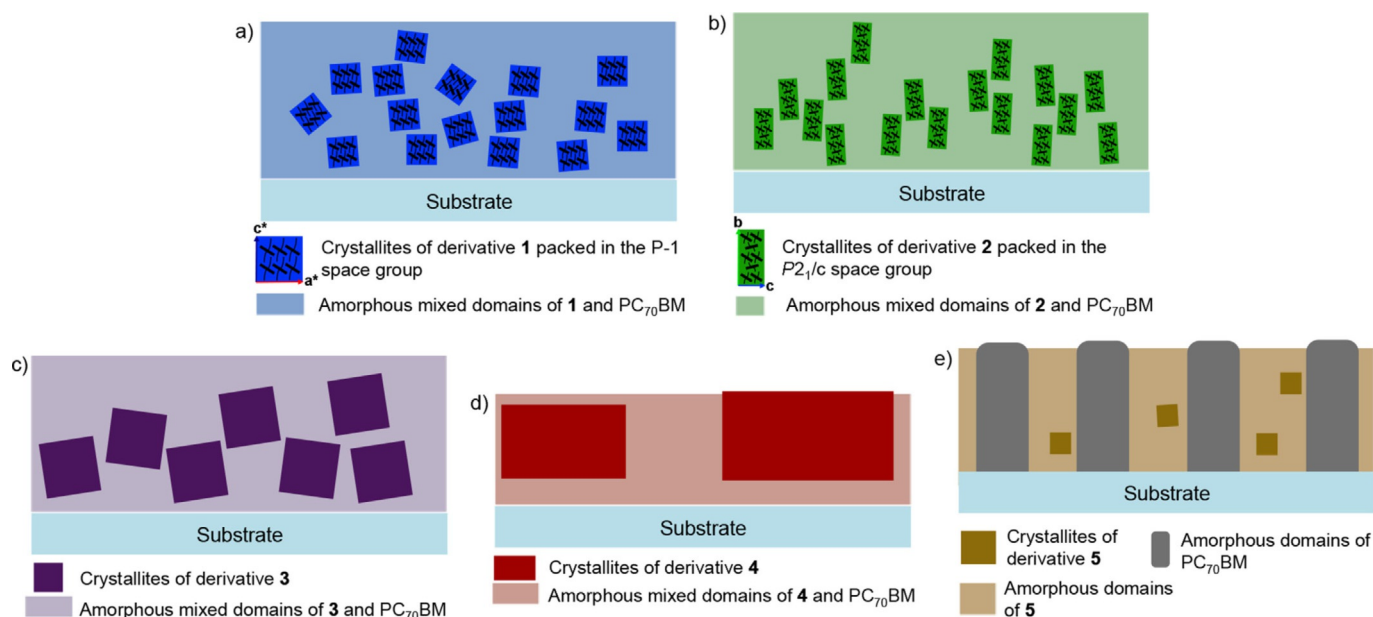
Figure 12. Schematic representation of active layers cross-sections under optimised conditions (side view) of a) **1** that shows partially oriented crystallites of **1** in the $P\bar{1}$ phase (the direction of the arrangement is represented with respect to the reciprocal lattice the a^* and c^* direction of which are represented by the red and blue arrows), b) **2** that shows uniformly oriented with anisotropic dimensions crystallites of **2** in the $P2_1/c$ phase (the direction of the arrangement is represented with respect to the crystal lattice the b and c directions of which are represented by the green and blue arrows), c) **3** that shows partially oriented large crystallites of **3**, d) **4** that shows highly oriented out-sized crystallites of **4** and e) **5** that shows scarce oriented crystallites of **5** embedded in a segregated amorphous region of **5** resulting from spin-coating-induced demixing.[23].

the D/A amorphous matrix that the nucleus grows from), and ΔG_E, which is the elastic free energy change caused by the strain that arises from the growth of a particle in the solid matrix. The latter two energy terms act as a barrier to nucleation. The profile shape of the free energy change of the transformation for a given system proceeds through a maximum value (activation energy) that determines the critical nucleus size (r^*) to be achieved for crystallite growth to become favourable (if $d\Delta G(r)/dr = 0$; ΔG^*).[31]

Consequently, for a given active layer, r^* and ΔG^* will be determined by the intrinsic ability of the donor molecule to arrange in a thermodynamically stable crystalline phase (which maximises ΔG_C and minimises γ) in the amorphous D/A blend. The interfacial contribution to nucleus growth dominates at small nucleus sizes, whereas the volumetric ones ($\Delta G_V + \Delta G_E$) dominate at a large nucleus size. It is suggested that SVA decreases the G_E contribution to result presumably in a lower G^* than that obtained by thermal annealing methods. This is supported by the fact that crystallisation occurs at low temperatures (typically room temperature) as opposed to the thermal annealing process and that crystals of a macroscopic size are grown commonly from thin layers through SVA;[32] the solvent-saturated atmosphere allows molecule dislocation over macroscopic distances (which implies a negligible strain contribution).

Once nuclei with a size larger than r^* have formed, the rate of crystallite growth is limited by the diffusion of donor molecules from the bulk (the mixed D/A amorphous phase) to the interface and transfer of a donor molecule from the vicinity of the nucleus to the interface.[33]

To provide an insight into the energetics of crystallite growth, we first measured the surface free energy (SFE) of non-annealed active layers made from each derivative under identical conditions of OSC device fabrication. To determine the SFE, we employed the Owens–Wendt–Rabel–Kaelble (OWRK) method by measuring the contact angle between three solvents of different polarity and the active layer surface (see the Supporting Information for details). The SFE measured by using this technique provides a relative quantification of the interfacial energy γ of the amorphous fraction of the active layers in the early stage of crystalline growth ($r = 0$; Figure 13). The polar and dispersive fractions of the SFE are reported in Table 2. As expected, the polar fraction shows a very similar contribution for all derivatives because of the highly apolar nature of the components of the active layer. However, the dispersive component of the SFE, which is assumed to model the interaction between the amorphous active layer matrix and the donor molecules satisfactorily, varies significantly between the derivatives. Active layers of **2** display the highest value of SFE, and that of **4** displays the lowest value.

Thereafter, to provide a qualitative analysis of the ΔG_V contribution, we derived the free energy change of crystallisation $\Delta_{crys}G$ for **1** and **2** from the enthalpy of fusion ($\Delta_{fus}H$) of crystalline powder samples of **1** and **2**, which could be isolated as pure $P\bar{1}$ and $P2_1/c$ phases, respectively. The $\Delta_{fus}H$ of the powders was derived from the specific heat capacity of the materials measured by using differential scanning calorimetry (DSC; see the Supporting Information for powder characterisation, DSC curves and $\Delta_{fus}H$ and ΔG_V calculation). The calculated values of $\Delta_{crys}G$ show that the formation of crystallites of **2** in

ChemPubSoc
Europe

CHEMSUSCHEM
Full Papers
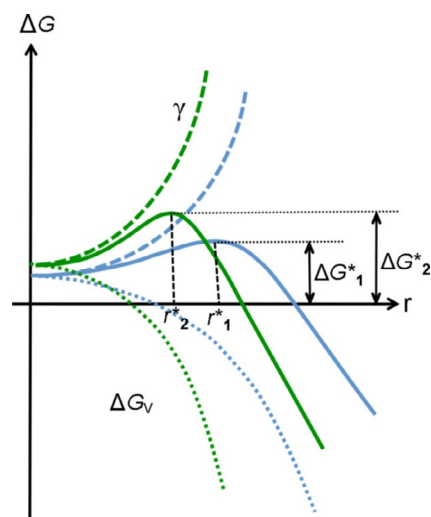
Figure 13. Hypothetical energy profile of donor nucleation in active layers of **1** and **2**.

Table 2. Average surface free energy of the non-annealed active layers and crystallisation free energy change of powders of **1** ($P\bar{1}$) and **2** ($P2_1/c$). The blend composition of the active layers and the deposition conditions of the active layer are identical to those of optimised devices (see Table 1 and the Supporting Information).

Derivative	Surface free energy [J]			Free-energy change (crystalline phase)	
	average disperse	average polar	total average	$\Delta_{crys}G$ [kJ mol^{-1}]	ΔG_V [J cm^{-3}]
1	20.8	3.4	24.2	−23.6	−46.6
2	29.2	1.7	30.9	−42.9	−72.7
3	22.7	1.9	24.6	–	–
4	16.1	1.8	18.0	–	–
5	24.2	1.1	25.3	–	–

the $P2_1/c$ phase is thermodynamically more favourable [($\Delta_{crys}G$(**2**-$P2_1/c$) < $\Delta_{crys}G$(**1**-$P\bar{1}$)] than the formation of crystallites of **1** in a $P\bar{1}$ phase (Table 2). However, the values of $\Delta_{crys}G$ must be converted to their volumetric counterpart (ΔG_V) to have a sensible meaning for our crystallite growth analysis. To do this, the unit cell volume calculated from each of the crystalline phases from the single-crystal XRD structure is used (see Supporting Information for details). The volumetric values of the free energies are reported in Table 2.

We then use these values as a relative indicator to draw a hypothetical energy profile of the nucleation process. That is, if we neglect the ΔG_E contribution, the experimental SFE and ΔG_V show that the interfacial energy (γ) for nuclei formation in an active layer of **1** and **2** and their associated bulk crystalline free energy change profile (ΔG_V) are likely to adopt the shape of that in Figure 13. The higher ΔG_V contribution compensates for the higher interfacial energy experienced by nuclei of **2** during crystalline growth in the amorphous matrix of the active layer. As a result, $r*_2$ is inferior to $r*_1$ and the formation of nuclei of **1** is favoured kinetically over that of **2** ($\Delta G*_1 < \Delta G*_2$).

This model is in good agreement with the experimental evidence obtained by using XRD (Figure 6). First, the rate of nucleation is relatively slow for **2**, for which there is virtually no increase in overall crystalline volume (peak integral) after 10 min of SVA, whereas nucleation proceeds faster in the case of **1** to show a great increase in crystalline volume after 10 min of SVA (Figure 6a and b). This increase in the crystalline volume is almost exclusively the result of a predominant rate of nucleation with respect to growth as no concomitant increase in crystallite size is observed.[34] The opposite trend is seen for **2**. Consequently, in active layers of **1** growth is the rate-limiting step, whereas in active layers of **2** nucleation is the rate-limiting step, although the rate of growth is relatively slow in this case as well. The fact that small crystallites are produced in active layers of **2** and larger ones in the case of **1** follows the assumption of $r*_2 < r*_1$ and further corroborates that the rate of growth is relatively slow (with respect to nucleation) in both cases.

Unfortunately, the energy profile of crystallite formation in active layers of **3**, **4** and **5** was not obtainable because the crystalline phase of the donor crystallites in the case of **3**, **4** and **5** is not known. However, following the above observations, it can be estimated by using XRD and AFM (vide supra) that the rates of nucleation and growth are rather balanced in the case of **3**. That is, the observed increase in the crystalline volume and crystallite size confirms that both nucleation and growth are favoured kinetically.

The case of derivative **4** exemplifies the trend in which, contrary to that of **1**, the growth rate is faster than the nucleation rate as seen by the presence of a small number of very large crystallites. However, derivative **5** shows slow rates of both nucleation and growth. The rather extreme difference in behaviour between derivatives **1** and **5** is most probably because of the bulk free energy change (ΔG_V) dissimilarity between **4** and **5**. That is, it is very likely that the solid-state packing energetics of **5** will be affected greatly by the presence of six very weakly polarisable atoms distributed homogeneously around its conjugated core to lead to a lower free energy change of crystallisation unable to cope with the higher interfacial free energy contribution in the nucleation process. Additionally, the behaviour of **1** and **5** indicates the impact of the donor chemical structure on the initial demixing step to provide active layers with different SFEs. The low SFE inherited from the spin-coating parameters (speed, spinning time and acceleration) as well as the D/A ratio are both accountable in the case of **4** for the growth of extremely large crystallites.

In addition to the influence of the interface energy on the crystallite growth, there is a propensity for crystallites to grow along a specific crystallographic direction. This is exemplified by **2** the powdered layer diffractogram of which advocates that the growth occurs preferentially along the (0 1 0) direction, which implies that the largest side of the crystallites is oriented perpendicularly to the substrate surface as demonstrated by using GIXRD.

ChemPubSoc
Europe

CHEMSUSCHEM
Full Papers

Non-geminate recombination

A previous study showed unambiguously that the V_{OC} of devices can differ greatly from the expected V_{OC} calculated from the frontier orbital energies. This has been attributed to the impact of morphological features on non-geminate recombination. Indeed, the D–A interfacial area and carrier mobility govern the kinetics of non-geminate recombination and, consequently, the quasi-Fermi level energetics. Durrant et al. quantified with great accuracy the extent to which non-geminate recombination induces a voltage drop with respect to that calculated theoretically on both polymer- and SM-based solar cells.[8, 35, 36] To identify how the morphological features contribute to the V_{OC}, and to some extent to the shape of the J–V characteristics, a qualitative recombination study was performed using transient optoelectronic methods, namely, charge extraction (CE) and transient photovoltage (TPV), popularised by Durrant and co-workers (see the Supporting Information for experimental details).[37–40] The link between recombination kinetics and morphology will be discussed below. To probe the recombination dynamics in OSCs it is important to measure the charge carrier dynamics of devices under working conditions. CE can be used to measure the average charge density at open circuit in the devices from light intensities >1 Sun to dark conditions. The corresponding plots of the charge density (n) versus V_{OC} of all the devices are shown in Figure 14 a. The data are in good agreement with a charge density of similar magnitude in all measurements, which reaches approximately 2×10^{16} charges cm^{-3} at values close to V_{OC}, similar to that reported earlier for such types of devices.[40] For all the devices, the total charge fits an exponential increase, which is evidence of charge accumulation in the bulk of the device (as opposed to at the contacts). The plots of n versus V_{OC} were fitted to single exponentials [Eq. (2)] consistent with an exponential tail of trap states that extends into the band gap of the active layer.[41, 42]

$$n = n_0 e^{\gamma V_{OC}} \tag{2}$$

$$\tau_{\Delta n} = \tau_0 e^{\beta V_{OC}} \tag{3}$$

The carrier lifetime ($\tau_{\Delta n}$) versus V_{OC} plot for all the devices is shown in Figure S24, and the the curves were fitted to single exponential decays in the form of Equation (3). The overall order of recombination ϕ [Eq. (4)] can be approximated to $\phi = \lambda + 1$ in our TPV experimental conditions ($\Delta n \ll n$).[39] The parameter λ is obtained experimentally by fitting the curve of the small perturbation carrier lifetime $\tau_{\Delta n}$ versus n to a power law in the form of Equation (5).

$$\frac{dn}{dt} = -kn^{\phi} \tag{4}$$

$$\tau_{\Delta n} = \tau_{\Delta n_0} n^{-\lambda} \tag{5}$$

First, the overall small perturbation life times are in good agreement with the trend of experimental V_{OC} for all devices. That is, devices from 4 and 5 have a higher V_{OC} and display an overall longer carrier lifetime, whereas devices from 1, 2 and 3 show much shorter lifetimes. The lifetimes of devices from 2 are the shortest, which follows the trend of the V_{OC}.

Interestingly, the recombination order (ϕ) varies significantly from device to device, with unexpectedly high values (ϕ = 11.8). High values of ϕ, as opposed to a value of 2, which is to be expected in a strictly bimolecular recombination process in the case of Langevin-type recombination, have been recorded several times in earlier studies[39, 42, 43] and were attributed to recombination through trap states in the band gap of the active layer materials.[43] Therefore, the non-geminate recombination process is described as an essentially bimolecular process in which the recombination coefficient is allowed to be charge dependent according to the presence of trap states in the band gap.[38, 39] Recently, it has been demonstrated that extremely high values of ϕ are likely the result of predominant
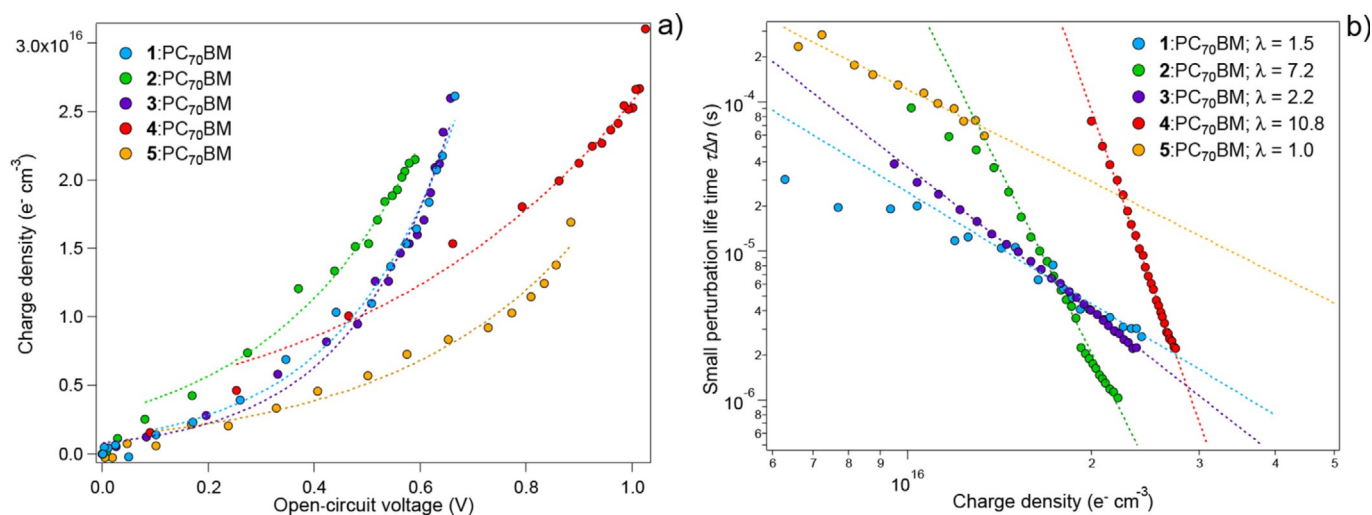
Figure 14. a) Comparison of the charge density (n) as a function of V_{OC} determined by using CE. The curves are fitted to an exponential growth of the form $N = N_0 e^{(\gamma V_{OC})}$ (dotted line) the parameters of which are reported in Table 3. b) Small perturbation carrier lifetime versus charge carrier density plot. The charge carrier density was calculated from the exponential fitting of a. Curves are fitted to power law decays of the form $\tau_{\Delta n} = \tau_{\Delta n0} n^{-\lambda}$ the parameters of which are reported in Table 3.

UNIVERSITAT ROVIRA I VIRGILI
NOVEL ELECTRON ACCEPTORS AND NEW SOLUTION PROCESSED HOLE BLOCKING LAYER FOR ORGANIC SOLAR CELLS
Caterina Stenta

ChemPubSoc
Europe

CHEMSUSCHEM
Full Papers

surface recombination as expected for very thin (<100 nm) active layers.[44] This is in very good agreement with the morphological data expounded above, whereby devices made out of derivative **4**, which display an abnormally high recombination order, have extremely large domains of pure donor in direct contact with the top metal cathode that induces increased surface recombination kinetics. The consequence of the morphology-induced high recombination order is further illustrated in Figure S9, in which the V_{OC} of the device is practically independent of light illumination. Hence, the fast decrease in charge carrier lifetime with respect to charge carrier density (i.e., light illumination), expressed by ϕ, is consistent with a limited hole and electron quasi-Fermi level splitting at stronger light biases. A high recombination order is observed for **2**, although to a lesser magnitude than for **4**. However, in this case, rather than being caused by donor domains in direct contact with the cathode, it may be the result of an inhomogeneity of the electrons and holes concentration along the active layer thickness[44] as crystallites of donors in devices of **2** have grown preferentially along the surface normal.

Devices made of **1** and **3** show a similar recombination order, whereas devices of **5** show a much lower recombination order of 2, consistent with very-low-mobility semiconductors in which recombination is limited by the probability of the encounter of electrons and holes. Importantly, the recombination data are in good agreement with the trend of V_{OC}, whereby the experimental V_{OC} in each device is decreased with respect to the theoretical value from a magnitude roughly proportional to the mean recombination lifetimes around 1 Sun illumination light bias. That is, devices in which charge carrier lifetimes are shorter at a high charge carrier density (which corresponds to $\approx$1 Sun illumination) show the smallest difference between their theoretical V_{OC} and the experimental value (ΔV_{OC} [%]; Table 3) and vice versa. Accordingly, devices made of **2**, which display the fastest kinetics under 1 Sun illumination bias as a result of the high recombination order, show the largest ΔV_{OC}. However, devices made of **4** and **5** show the opposite trend for which ΔV_{OC} is the smallest although devices made of **4** have a very high recombination order.

Overall, the mean small perturbation lifetime at low light bias is consistent with the trend of the D–A interfacial area derived from the crystallite size and hole mobility values. That is, charge carriers in devices made of **2** exhibit a significantly longer lifetime at low illumination biases than devices made of **1**, although **1** and **2** have similar morphological features (similar crystallite size). The difference in the mean lifetime at a low

bias may then be related to the difference in hole mobility, which is more than one order of magnitude higher in devices made of **1**. Conversely, the extremely low mobility in devices made of **5** is responsible for the slow recombination lifetimes at low light bias regardless of the presence of fairly intermixed D/A domains. The slow recombination lifetimes at low light bias of devices made of **4** could, on the contrary, be attributed to the reduced D–A interfacial area occasioned by the extremely large crystallites of donor.

The case for **3** is rather difficult to rationalise solely by considering morphological aspects. The small ΔV_{OC} is presumably because of a narrower density of states (DoS) distribution as extrapolated from the charge extraction measurements (i.e., the position of the CE curve from devices made of **3**; Figure 14a).

Discussion

In the above sections, several key structural parameters have been related to the solar cell device performance of each derivative. First of all, a very simple quantitative analysis of the absorption properties of each derivative active layer demonstrated how thin SM-BHJ active layers limit light absorption and thus photocurrent generation. Therefore, the slight decrease in the absorption coefficient of the donor derivatives **1**, **2** and **4** with respect to the reference DPP(TBFu)$_2$ does not account for the decrease in the absorption intensity of the active layers. Instead, the active layer thickness, D/A ratio and molecular weight of the donor play a significant role to determine the absorption capability of the final active layer. The main challenge resides in the fact that none of these parameters can be controlled selectively as the optimum D/A ratio and optimum active layer thickness are found experimentally during the device optimisation process. That is, the optimum D/A ratio of each material is determined by a set of electrical properties, which will eventually limit the active layer to a thickness that provides the best compromise between strong absorption, fast transport and slow recombination kinetics. This effect is exemplified in our study in which several devices that had undergone D/A ratio and thickness optimisation resulted in a similar hole mobility although it spanned a range of different thicknesses and active layer crystallinity features. Finally, the molecular weight impacts directly on the actual quantity of donor present in the active layer. For a given weight ratio of D/A, the absorption depends directly on the molar quantity of donor with respect to that of the acceptor (and the absorption

Table 3. J–V characteristics and electrical properties of all devices. The theoretical V_{OC} is calculated from: $V_{OC} = 1/e\,[(LUMO_{donor} - HOMO_{acceptor}) - 0.3\ eV]$.

Derivative	V_{OC} (theoretical) [V]	V_{OC} (experimental) [V]	ΔV_{OC} [V]	$\Delta V_{OC,\,offset}$ [%]	J_{SC} [mA cm^{-2}]	FF [%]	PCE [%]	ϕ	Hole mobility [cm^{2}V^{-1}s^{-1}]
1	1.0	0.702	0.298	30	4.77	45	1.52	2.5	1.25×10^{-6}
2	1.1	0.608	0.492	44	2.78	55	0.93	5.8	1.28×10^{-8}
3	0.8	0.628	0.172	21	4.80	44	1.32	3.2	8.5×10^{-8}
4	1.3	1.060	0.240	18	2.84	45	1.34	11.8	6.3×10^{-8}
5	1.2	0.964	0.236	19	1.11	25	0.27	2.0	6.9×10^{-10}
DPP(TBFu)$_2$	1.1	0.858	0.242	22	8.97	48	3.64	–	5.3×10^{-4}–2×10^{-5}

UNIVERSITAT ROVIRA I VIRGILI
NOVEL ELECTRON ACCEPTORS AND NEW SOLUTION PROCESSED HOLE BLOCKING LAYER FOR ORGANIC SOLAR CELLS
Caterina S...

ChemPubSoc
Europe

ChemSusChem
Full Papers

of fullerene being negligible in the visible region). Consequently, donor **3**, the absorption coefficient of which is almost twice as high as that of donor **1**, does not provide the expected stronger absorption in active layer films (at a similar D/A ratio and a similar thickness) because the molecular weight of **3** is more than twice that of **1**.

The charge separation and charge transport properties are acquired upon the formation of crystalline domains from the amorphous D/A matrix. Therefore, the kinetics of crystallite growth is of the greatest importance to establish a link between the structure of the donor and the J–V characteristics. An insight into the thermodynamics that govern the process has been obtained. The ability of the donor to crystallise in the active layer is governed principally (at least in SVA-treated active layers) by ΔG_V and γ. Both factors are intrinsic to the structure of the donor and are affected greatly by subtle changes in its chemical structure. As such, donors with subtle differences in their structures, such as **4** and **5**, provide active layers with extremely different crystallisation energetics that impact on the overall crystallinity. In this particular case, the presence of the highly electronegative F atoms distributed in a different manner on the DPP core might induce a difference in London dispersion forces between **4** and **5**, which impacts directly on both ΔG_V and γ. Generally, any change in the donor structure will have a significant impact on ΔG_V as seen from the experimental values of $\Delta_{crys}G(\mathbf{2}\text{-}P2_1/c)$ and $\Delta_{crys}G(\mathbf{1}\text{-}P\bar{1})$, which thus induces a tremendous change in the crystallisation kinetics.

The miscibility of the donor with the acceptor in the solid state is presumably important to determine the energetics of the active layer (the interfacial energy γ) before the nucleation and growth process. That is, the magnitude of the D/A demixing that occurs in the early stages of the active layer deposition is of capital importance to the following crystallite growth that occurs during the annealing step as the latter is linked directly to the surface energy that results from the earlier D/A demixing.[25, 26] This phenomenon certainly explains the differences in the morphology and crystallinity observed upon changes in deposition conditions (spin coating solvent, speed and acceleration) in earlier studies.[22, 45] Subsequent to the deposition, the optimisation of the SVA time, which allows crystallites to grow to a determined size, establishes a trade off between high hole mobility and a high D–A interface. Importantly, the SVA, thickness and D/A ratio are related indirectly as changes in the D/A ratio will impact the energetics of crystallite growth, which in turn will impose a limitation on the maximum attainable thickness, itself determined by the maximum attainable hole mobility in a given crystalline state.

Provided that mobility is sufficiently high, the final active layer D–A interfacial area that results from these optimisation processes will further limit the device characteristics. A low interfacial area will limit the J_{SC} but provide less V_{OC} losses through reduced non-geminate recombination kinetics, as exemplified by donor **4**. Conversely, the higher interfacial area in devices of **1** corroborates the higher experimental losses in V_{OC}, whereas the J_{SC} losses (with respect to the absorption properties of the active layers) are minimal. Derivatives **2** and **3**

show a more balanced behaviour, where subtle morphological parameters (such as the crystallite shape anisotropy and presumed narrow DoS distribution) induce additional losses (high V_{OC} losses for **2**) or unexpected loss compensation (lower-than-expected V_{OC} losses from recombination kinetics for **3**). The rather low J_{SC} in **2** that arises from the low photon-to-charge conversion efficiency at lower wavelengths might stem from a low hole mobility. Derivative **5** illustrates the case for which crystallite growth is not seen to occur with sufficient magnitude and leads to very low hole mobility that limits the J_{SC} even further than that of **2**.

If the experimental lifetime correlates the loss in V_{OC} with respect to the theoretical maximum, the expected correlation between recombination and FF is not observed herein. The negligible field dependency on charge generation displayed by polymer-based devices[36, 37c,f, 39, 42a, 46] is usually not as insignificant in SM-BHJ devices[40b] because of charge delocalisation (especially holes) that occurs over short distances and mostly in crystalline domains. Thus, it makes sense to assume that the higher FF observed in devices of **2**, is the result of a larger hole delocalisation distance in the direction of charge extraction that results from donor crystallite shape anisotropy, and the non-geminate recombination kinetics have little influence on the shape of the J–V curve (FF) in this case.[40b] This is further supported by the fact that FF increases up to 66% (with no significant concomitant increase in V_{OC}) with the increasing crystallite size promoted by longer SVA times (data not shown), which favours charge extraction at a low internal field.

Finally, the packing pattern of donor molecules in the crystalline domains is expected to have a significant influence on the transport properties. The powdered layer method provided precise information on the crystalline phase of the crystalline domains for active layers of **1** and **2**. In the case of **1**, molecules pack in a low-symmetry $P\bar{1}$ space group with molecules stacked uniformly over a long range. Derivative **2** packs in the $P2_1/c$ space group in a herringbone fashion. A significantly higher transfer integral could be expected in crystals of **1** in the direction perpendicular to the π-delocalised backbone plane because of apparent greater π–π overlap and slightly shorter stacking distances than that in crystals of **2** (Figures 10 and 11). The lower-symmetry packing of **1** induces continuous stacking in the three directions of space, whereas the herringbone arrangement in the case of **2** implies a discontinuity in the arrangement.

As demonstrated previously, mobility in organic materials often displays a high degree of anisotropy, which is related directly to the packing pattern in the solid state.[47] As such, the orientation of the solid-state packing arrangement with respect to the substrate is likely to play a very important role in the hole mobility properties in the bulk. Low-symmetry "slipped stacked" patterns, such as that of **1**, lead to highly anisotropic mobility with the highest value perpendicular to the π–π stacks. Herringbone arrangements usually lead to less anisotropy as "hopping" is allowed in different directions of space. Our experimental observations are consistent with these assumptions. Indeed, derivative **1**, which forms highly oriented crystallites with respect to the out-of-plane direction with their

ChemPubSoc
Europe

CHEMSUSCHEM
Full Papers

π–π stacked backbone oriented, to a fair extent, perpendicular to the direction of charge collection, gives rise to the highest space-charge-limited current (SCLC) mobility (Table 3).

Conclusions

We employed a myriad of characterisation techniques to relate the device characteristics of small-molecule bulk-heterojunctions (SM-BHJ) with the morphological features of the active layers induced by the donor structure. We demonstrated that subtle changes in the donor structure have a significant impact on the device characteristics. As such, the prediction of the characteristics of SM-BHJ devices from the chemical structure of the donor remains a challenging task. However, our study indicated some basic requirements to be taken into account in the design of new donors for SM-BHJ. Importantly, it is imperative that the donor is able to grow numerous monodisperse nanometre-sized crystallites of donors inside the donor/acceptor amorphous matrix. Additionally, the strong propensity of small-molecule donor crystallites to adopt a uniform orientation in active layers of organic solar cell devices seen in this study and others is a key parameter to determine the transport properties in the bulk. That is, crystallites with a uniform orientation lead to a higher mobility in the organic material because of faster intra-grain charge hopping.[48] However, to have a positive impact, the orientation has to match the direction of fast transport in the crystallites. In this respect the solid-state packing of the donor molecule plays a major role. Although π–π-stacked units could provide fast charge hopping in the direction perpendicular to the stacks, it usually implies that hopping is reduced in the remaining directions of space. This anisotropy feature is usually decreased in higher-symmetry packing patterns. Consequently, if a donor is seen to pack in a low-symmetry crystalline phase, it is essential that the crystallite is oriented in the direction of higher mobility. A higher-symmetry arrangement could be more forgiving.

All these inter-related properties are extremely difficult to predict as the crystallisation of small molecules stems from weak inter-molecular interactions between donors, which are disrupted easily in the complex environment of SM-BHJ active layers (e.g., in the presence of fullerene, solvents and additives). As a first step towards the understanding of crystallite formation in small-molecule active layers, we propose that the crystalline growth through a nucleation and growth mechanism, at least if the solvent-vapour-annealing post-deposition treatment is applied, and as such a balance between the bulk energy of the growing crystallite and the interface energy is necessary to favour the growth of homogenous crystallites. According to this model, it is apparent that the crystalline phase in which the donor packs in the active layer is the key to direct the formation of the micro-structure. Such a property is challenging to predict, but advanced methods to control the packing of donor molecules could be imagined, for instance, by the use of supramolecular binding motifs[49] or through extensive computational simulations.[50,51]

Some aspects of the absorption properties of the donor have been clarified. We showed that the main factor that limits the absorption of the active layers is the active layer thickness, the maximum of which is limited indirectly by the transport and recombination properties given by the film nano-/micro-structure. Although no concrete design rules could be identified, the maximisation of the absorption coefficient of the donor as its molecular weight is kept as low as possible is a requisite to maximise the dye molar content of the active layer, and thus maximise the absorption of the latter.

Finally, it appears that the power conversion efficiency improvement in SM-BHJ from rational design is rather limited and may rely on empirical design unless some supramolecular interactions could be used to control the crystallisation of the donor in the active layers.

Acknowledgements

Conflict of interest

The authors declare no conflict of interest.

[1] a) V. Gupta, A. K. K. Kyaw, D. H. Wang, S. Chand, G. C. Bazan, A. J. Heeger, *Sci. Rep.* **2013**, *3*, 1965; b) A. K. K. Kyaw, D. H. Wang, V. Gupta, J. Zhang, S. Chand, G. C. Bazan, A. J. Heeger, *Adv. Mater.* **2013**, *25*, 2397; c) A. K. K. Kyaw, D. H. Wang, D. Wynands, J. Zhang, N. Thuc-Quyen, G. C. Bazan, A. J. Heeger, *Nano Lett.* **2013**, *13*, 3796; d) Y. Liu, C.-C. Chen, Z. Hong, J. Gao, Y. Yang, H. Zhou, L. Dou, G. Li, *Sci. Rep.* **2013**, *3*, 3356; e) D. H. Wang, A. K. K. Kyaw, V. Gupta, G. C. Bazan, A. J. Heeger, *Adv. Energy Mater.* **2013**, *3*, 1161; f) J. Zhou, J. Zuo, X. Wan, G. Long, Q. Zhang, W. Ni, Y. Liu, Z. Li, G. He, C. Li, B. Kan, M. Li, Y. Chen, *J. Am. Chem. Soc.* **2013**, *135*, 8484; g) B. Kan, M. Li, Q. Zhang, F. Liu, X. Wan, Y. Wang, W. Ni, G. Long, X. Yang, H. Feng, Y. Zuo, M. Zhang, F. Huang, Y. Cao, T. P. Russell, Y. Chen, *J. Am. Chem. Soc.* **2015**, *137*, 3886; h) W. Ni, M. Li, F. Liu, X. Wan, H. Feng, B. Kan, Q. Zhang, H. Zhang, Y. Chen, *Chem. Mater.* **2015**, *27*, 6077.

[2] a) O. P. Lee, A. T. Yiu, P. M. Beaujuge, C. H. Woo, T. W. Holcombe, J. E. Millstone, J. D. Douglas, M. S. Chen, J. M. J. Frechet, *Adv. Mater.* **2011**, *23*, 5359; b) G. He, Z. Li, X. Wan, Y. Liu, J. Zhou, G. Long, M. Zhang, Y. Chen, *J. Mater. Chem.* **2012**, *22*, 9173; c) C. J. Takacs, Y. Sun, G. C. Welch, L. A. Perez, X. Liu, W. Wen, G. C. Bazan, A. J. Heeger, *J. Am. Chem. Soc.* **2012**, *134*, 16597; d) J. Zhou, X. Wan, Y. Liu, Y. Zuo, Z. Li, G. He, G. Long, W. Ni, C. Li, X. Su, Y. Chen, *J. Am. Chem. Soc.* **2012**, *134*, 16345; e) N. D. Eisenmenger, G. M. Su, G. C. Welch, C. J. Takacs, G. C. Bazan, E. J. Kramer, M. L. Chabinyc, *Chem. Mater.* **2013**, *25*, 1688; f) V. S. Gevaerts, E. M. Herzig, M. Kirkus, K. H. Hendriks, M. M. Wienk, J. Perlich, P. Müller-Buschbaum, R. A. J. Janssen, *Chem. Mater.* **2014**, *26*, 916; g) G. He, Z. Li, X. Wan, J. Zhou, G. Long, S. Zhang, M. Zhang, Y. Chen, *J. Mater. Chem. A* **2013**, *1*, 1801; h) M. Weidelener, C. D. Wessendorf, J. Hanisch, E. Ahlswede, G. Gotz, M. Linden, G. Schulz, E. Mena-Osteritz, A. Mishra, P. Bäuerle, *Chem. Commun.* **2013**, *49*, 10865.

[3] a) X. Liu, Y. Sun, L. A. Perez, W. Wen, M. F. Toney, A. J. Heeger, G. C. Bazan, *J. Am. Chem. Soc.* **2012**, *134*, 20609; b) Y. Liu, X. Du, Z. Xiao, J. Cao, S. Tan, Q. Zuo, L. Ding, *Synth. Met.* **2012**, *162*, 1665; c) G. He, Z. Li,

X. Wan, J. Zhou, G. Long, S. Zhang, M. Zhang, Y. Chen, *J. Mater. Chem. A* **2013**, *1*, 1801; d) J.-Y. Pan, L.-J. Zuo, X.-L. Hu, W.-F. Fu, M.-R. Chen, L. Fu, X. Gu, H.-Q. Shi, M.-M. Shi, H.-Y. Li, H.-Z. Chen, *ACS Appl. Mater. Interfaces* **2013**, *5*, 972; e) G. Chen, H. Sasabe, Y. Sasaki, H. Katagiri, X.-F. Wang, T. Sano, Z. Hong, Y. Yang, J. Kido, *Chem. Mater.* **2014**, *26*, 1356; f) Y. Kim, C. E. Song, A. Cho, J. Kim, Y. Eom, J. Ahn, S.-J. Moon, E. Lim, *Mater. Chem. Phys.* **2014**, *143*, 825; g) G. D. Sharma, M. A. Reddy, K. Ganesh, S. P. Singh, M. Chandrasekharam, *RSC Adv.* **2014**, *4*, 732; h) R. Zhou, Q.-D. Li, X.-C. Li, S.-M. Lu, L.-P. Wang, C.-H. Zhang, J. Huang, P. Chen, F. Li, X.-H. Zhu, W. C. H. Choy, J. Peng, Y. Cao, X. Gong, *Dyes Pigm.* **2014**, *101*, 51.

[4] E. Ripaud, D. Demeter, T. Rousseau, E. Boucard-Cetol, M. Allain, R. Po, P. Leriche, J. Roncali, *Dyes Pigm.* **2012**, *95*, 126.

[5] J. Liu, B. Walker, A. Tamayo, Y. Zhang, T.-Q. Nguyen, *Adv. Funct. Mater.* **2013**, *23*, 47.

[6] a) Y. Li, Q. Guo, Z. Li, J. Pei, W. Tian, *Energy Environ. Sci.* **2010**, *3*, 1427; b) Y. Lin, Y. Li, X. Zhan, *Chem. Soc. Rev.* **2012**, *41*, 4245; c) A. Mishra, P. Baeuerle, *Angew. Chem. Int. Ed.* **2012**, *51*, 2020; *Angew. Chem.* **2012**, *124*, 2060; d) Q. L. Huang, H. X. Li, *Chin. Sci. Bull.* **2013**, *58*, 2677; e) Y. Chen, X. Wan, G. Long, *Acc. Chem. Res.* **2013**, *46*, 2645.

[7] B. Walker, A. Tamayo, P. Zalar, T.-Q. Nguyen, *Adv. Funct. Mater.* **2009**, *19*, 3063.

[8] T. M. Clarke, J. R. Durrant, *Chem. Rev.* **2010**, *110*, 6736.

[9] A. Viterisi, F. Gispert-Guirado, J. W. Ryan, E. Palomares, *J. Mater. Chem.* **2012**, *22*, 15175.

[10] a) G. Li, Y. Yao, H. Yang, V. Shrotriya, G. Yang, Y. Yang, *Adv. Funct. Mater.* **2007**, *17*, 1636; b) H. Park, R. B. Ambade, S.-H. Lee, *J. Nanosci. Nanotechnol.* **2013**, *13*, 7975; c) B. Qu, D. Tian, Z. Cong, W. Wang, Z. An, C. Gao, Z. Gao, H. Yang, L. Zhang, L. Xiao, Z. Chen, Q. Gong, *J. Phys. Chem. C* **2013**, *117*, 3272.

[11] a) F.-C. Chen, C.-J. Ko, J.-L. Wu, W.-C. Chen, *Sol. Energy Mater. Sol. Cells* **2010**, *94*, 2426; b) R. Hegde, N. Henry, B. Whittle, H. Zang, B. Hu, J. Chen, K. Xiao, M. Dadmun, *Sol. Energy Mater. Sol. Cells* **2012**, *107*, 112.

[12] G. Wei, S. Wang, K. Sun, M. E. Thompson, S. R. Forrest, *Adv. Energy Mater.* **2011**, *1*, 184.

[13] E. Verploegen, C. E. Miller, K. Schmidt, Z. Bao, M. F. Toney, *Chem. Mater.* **2012**, *24*, 3923.

[14] The V_{OC} is often described to be proportional to the difference between the donor HOMO energy and the acceptor LUMO energy.

[15] M. C. Scharber, D. Mühlbacher, M. Koppe, P. Denk, C. Waldauf, A. J. Heeger, C. J. Brabec *Adv. Mater.* **2006**, *18*, 789.

[16] Absorptance, as opposed to absorbance, refers to the ratio of the light that passes through the sample over the incident light ($1-$Transmittance). The absorbance is used to describe the logarithm of that ratio. See IUPAC definitions: http://goldbook.iupac.org/A00035.htmland http://goldbook.iupac.org/A00028.html.

[17] J. Ajuria, S. Chavhan, R. N. Tena-Zaera, J. Chen, A. J. Rondinone, P. Sonar, A. Dodabalapur, R. Pacios, *Org. Electron.* **2013**, *14*, 326.

[18] The optimum thickness and D/A ratio were established experimentally and correspond to the value that provides the optimum compromise between strong absorption, fast carrier transport and slow recombination kinetics that leads to the overall highest power conversion efficiency for a given system.

[19] W. Shin, T. Yasuda, G. Watanabe, Y. S. Yang, C. Adachi, *Chem. Mater.* **2013**, *25*, 2549.

[20] The apparent decrease in the crystallite size in active layers of **1** upon longer annealing is not deemed to be significant as the uncertainty of the crystallite size measurement is fairly high at (13 ± 3) nm, and 19 ($\pm$ 3) nm signifies that the size difference between the crystallites is insignificant.

[21] a) D. M. DeLongchamp, R. J. Kline, D. A. Fischer, L. J. Richter, M. F. Toney, *Adv. Mater.* **2011**, *23*, 319; b) W. Chen, M. P. Nikiforov, S. B. Darling, *Energy Environ. Sci.* **2012**, *5*, 8045; c) J. Rivnay, S. C. B. Mannsfeld, C. E. Miller, A. Salleo, M. F. Toney, *Chem. Rev.* **2012**, *112*, 5488.

[22] A. Viterisi, N. F. Montcada, C. V. Kumar, F. Gispert-Guirado, E. Martin, E. Escudero, E. Palomares, *J. Mater. Chem. A* **2014**, *2*, 3536.

[23] The packing of the donor molecules inside the crystallites is symbolised by the black lines. The orientation of the crystallites is depicted with the (00 $\bar{1}$) and (0 $\bar{1}$ 0) (for the *P* $\bar{1}$ and *P*21/*c* phases, respectively) planes parallel to the substrates as deduced by using GIXRD. The crystallites are shown embedded in an amorphous matrix of mixed donor and PC$_{70}$BM molecules; however, the ratio between the amorphous and crystalline phases represented here only corresponds to a broad trend. The shape of the crystallites of **2** and **4** was deduced by using XRD and AFM, whereas that of **1**, **3** and **5** is not known.

[24] a) D. S. Germack, A. Checco, B. M. Ocko, *ACS Nano* **2013**, *7*, 1990; b) B. Ray, M. A. Alam, *Appl. Phys. Lett.* **2011**, *99*, 033303; c) G. Ruani, C. Fontanini, M. Murgia, C. Taliani, *J. Chem. Phys.* **2002**, *116*, 1713; d) M. A. Alam, B. Ray, M. R. Khan, S. Dongaonkar, *J. Mater. Res.* **2013**, *28*, 541; e) B. Ray, M. A. Alam, *Sol. Energy Mater. Sol. Cells* **2012**, *99*, 204.

[25] Y. Vaynzof, D. Kabra, L. Zhao, L. L. Chua, U. Steiner, R. H. Friend, *ACS Nano* **2011**, *5*, 329.

[26] W. Hu, D. Frenkel in *Interphases and Mesophases in Polymer Crystallization III, Vol. 191* (Ed.: G. Allegra), Springer, Berlin, Heidelberg, **2005**, 1.

[27] D. T. W. Toolan, A. J. Parnell, P. D. Topham, J. R. Howse, *J. Mater. Chem. A* **2013**, *1*, 3587.

[28] R. H. Gee, N. Lacevic, L. E. Fried, *Nat. Mater.* **2006**, *5*, 39.

[29] The experimental conditions would provide sufficient under-cooling for the homogeneous nucleation process to be favoured kinetically as the SVA is performed at room temperature (i.e., well below the melting temperature of the blend). However, it is very likely that heterogeneous nucleation dominates the process. This is supported by the fact that the crystallinity of the active layer (the total crystalline volume) has been shown previously to be highly dependent on the type and roughness of the substrate the active layer is deposited onto (see Ref [22] and D. Motaung, G. Malgas, S. Nkosi, G. Mhlongo, B. Mwakikunga, T. Malwela, C. Arendse, T. G. Muller, F. Cummings, *J. Mater. Sci.* **2013**, *48*, 1763; G. Fang, S. Wu, Z. Xie, Y. Geng, L. Wang, *Macromol. Chem. Phys.* **2011**, *212*, 1846; D. E. Motaung, G. F. Malgas, C. J. Arendse, T. Malwela, *Mater. Chem. Phys.* **2010**, *124*, 208; S. O. Jeon, K. S. Yook, J. Y. Lee, *Org. Electron.* **2009**, *10*, 1583).

[30] In the heterogeneous nucleation mechanism the free energy change of the transformation is simply a linear scaling of the free energy change of the homogenous nucleation process as follows: $\Delta G_{Hetero} = \Delta G_{Homo} f(\theta)$. The scaling factor, which depends on the contact angle (θ) between the nucleus and the surface from which the crystal is grown, is in our case deemed to be similar for all the active layers as they were deposited on the same indium tin oxide (ITO)/poly(3,4-ethylenedioxythiophene) (PEDOT):poly(styrenesulfonate) (PSS) substrate. It is thus omitted in this study.

[31] R. W. Balluffi, S. Allen, W. C. Carter, *Kinetics of Materials*, Wiley, **2005**.

[32] a) G. De Luca, A. Liscio, P. Maccagnani, F. Nolde, V. Palermo, K. Müllen, P. Samorì, *Adv. Funct. Mater.* **2007**, *17*, 3791; b) G. De Luca, A. Liscio, F. Nolde, L. M. Scolaro, V. Palermo, K. Mullen, P. Samori, *Soft Matter* **2008**, *4*, 2064; c) E. Treossi, A. Liscio, X. Feng, V. Palermo, K. Müllen, P. Samorì, *Small* **2009**, *5*, 112; d) G. De Luca, A. Liscio, M. Melucci, T. Schnitzler, W. Pisula, C. G. Clark, L. M. Scolaro, V. Palermo, K. Mullen, P. Samori, *J. Mater. Chem.* **2010**, *20*, 71; e) G. De Luca, E. Treossi, A. Liscio, J. M. Mativetsky, L. M. Scolaro, V. Palermo, P. Samori, *J. Mater. Chem.* **2010**, *20*, 2493.

[33] The formation of one preferential polymorphic structure is, to some extent, explained on the grounds of the change in free energy of crystal formation (ΔG_V), which is expected to vary from one crystalline phase to the other. However, the formation of the final crystalline phase in the active layer could proceed through a complex energetic path, which includes the formation of intermediate polymorphic nuclei to account for a greater ΔG_V and rearrangement towards a less energetically favoured crystalline phase that provides a lower interfacial energy able to compensate the lower ΔG_V of the new hypothetic polymorph (see: L. A. Perez, K. W. Chou, J. A. Love, T. S. van der Poll, D.-M. Smilgies, T.-Q. Nguyen, E. J. Kramer, A. Amassian, G. C. Bazan, *Adv. Mater.* **2013**, *25*, 6380). This implies that the resultant crystalline phase is not necessarily the most thermodynamically stable, that is, the one that leads to a larger difference in the crystal formation free energy.

[34] The apparent decrease in the crystallite size in active layers of **1** upon longer annealing is not deemed significant as the uncertainty of the crystallite size measurement is fairly high at (13 ± 3) nm, and ($19\pm$ 3) nm signifies that the size difference between the crystallites is insignificant.

[35] a) G. Lakhwani, A. Rao, R. H. Friend, *Annu. Rev. Phys. Chem.* **2014**, *65*, 557; b) J. Bisquert, G. Garcia-Belmonte, *J. Phys. Chem. Lett.* **2011**, *2*, 1950; c) G. Garcia-Belmonte, A. Guerrero, J. Bisquert, *J. Phys. Chem. Lett.*

CHEMSUSCHEM
Full Papers

2013, *4*, 877; d) A. Pivrikas, N. S. Sariciftci, G. Juška, R. Österbacka, *Prog. Photovoltaics* **2007**, *15*, 677; e) C. M. Proctor, M. Kuik, T.-Q. Nguyen, *Prog. Polym. Sci.* **2013**, *38*, 1941; f) J. W. Ryan, E. Palomares, *Adv. Energy. Mater.* **2016**, 1601509.

[36] A. Baumann, T. J. Savenije, D. H. K. Murthy, M. Heeney, V. Dyakonov, C. Deibel, *Adv. Funct. Mater.* **2011**, *21*, 1687.

[37] a) C. G. Shuttle, A. Maurano, R. Hamilton, B. O'Regan, J. C. de Mello, J. R. Durrant, *Appl. Phys. Lett.* **2008**, *93*, 183501; b) C. G. Shuttle, B. O'Regan, A. M. Ballantyne, J. Nelson, D. D. C. Bradley, J. R. Durrant, *Phys. Rev. B* **2008**, *78*, 113201; c) F. C. Jamieson, T. Agostinelli, H. Azimi, J. Nelson, J. R. Durrant, *J. Phys. Chem. Lett.* **2010**, *1*, 3306; d) D. Credgington, R. Hamilton, P. Atienzar, J. Nelson, J. R. Durrant, *Adv. Funct. Mater.* **2011**, *21*, 2744; e) D. Credgington, Y. Kim, J. Labram, T. D. Anthopoulos, J. R. Durrant, *J. Phys. Chem. Lett.* **2011**, *2*, 2759; f) G. F. A. Dibb, F. C. Jamieson, A. Maurano, J. Nelson, J. R. Durrant, *J. Phys. Chem. Lett.* **2013**, *4*, 803.

[38] a) R. Hamilton, C. G. Shuttle, B. O'Regan, T. C. Hammant, J. Nelson, J. R. Durrant, *J. Phys. Chem. Lett.* **2010**, *1*, 1432; b) A. Maurano, R. Hamilton, C. G. Shuttle, A. M. Ballantyne, J. Nelson, B. O'Regan, W. Zhang, I. McCulloch, H. Azimi, M. Morana, C. J. Brabec, J. R. Durrant, *Adv. Mater.* **2010**, *22*, 4987.

[39] A. Maurano, C. C. Shuttle, R. Hamilton, A. M. Ballantyne, J. Nelson, W. Zhang, M. Heeney, J. R. Durrant, *J. Phys. Chem. C* **2011**, *115*, 5947.

[40] a) D. Credgington, J. R. Durrant, *J. Phys. Chem. Lett.* **2012**, *3*, 1465; b) D. Credgington, F. C. Jamieson, B. Walker, N. Thuc-Quyen, J. R. Durrant, *Adv. Mater.* **2012**, *24*, 2135.

[41] a) M. P. Eng, P. R. F. Barnes, J. R. Durrant, *J. Phys. Chem. Lett.* **2010**, *1*, 3096; b) C. G. Shuttle, R. Hamilton, J. Nelson, B. C. O'Regan, J. R. Durrant, *Adv. Funct. Mater.* **2010**, *20*, 698.

[42] a) C. G. Shuttle, R. Hamilton, B. C. O'Regan, J. Nelson, J. R. Durrant, *Proc. Natl. Acad. Sci. USA* **2010**, *107*, 16448; b) D. Spoltore, W. D. Oosterbaan, S. Khelifi, J. N. Clifford, A. Viterisi, E. Palomares, M. Burgelman, L. Lutsen, D. Vanderzande, J. Manca, *Adv. Energy Mater.* **2013**, *3*, 466.

[43] a) R. C. I. MacKenzie, T. Kirchartz, G. F. A. Dibb, J. Nelson, *J. Phys. Chem. C* **2011**, *115*, 9806; b) T. Kirchartz, B. E. Pieters, J. Kirkpatrick, U. Rau, J. Nelson, *Phys. Rev. B* **2011**, *83*, 115209.

[44] T. Kirchartz, J. Nelson, *Phys. Rev. B* **2012**, *86*, 165201.

[45] a) S. Ferdous, F. Liu, D. Wang, T. P. Russell, *Adv. Energy Mater.* **2014**, *4*, 1300834; b) B. Walker, A. Tamayo, D. T. Duong, X.-D. Dang, C. Kim, J. Granstrom, T.-Q. Nguyen, *Adv. Energy Mater.* **2011**, *1*, 221; c) D. T. Duong, B. Walker, J. Lin, C. Kim, J. Love, B. Purushothaman, J. E. Anthony, T.-Q. Nguyen, *J. Polym. Sci. Part B* **2012**, *50*, 1405; d) M. A. Ruderer, P. Müller-Buschbaum in *Polymers for Energy Storage and Conversion*, Wiley, Weinheim, **2013**, p. 137.

[46] a) S. A. Hawks, F. Deledalle, J. Yao, D. G. Rebois, G. Li, J. Nelson, Y. Yang, T. Kirchartz, J. R. Durrant, *Adv. Energy Mater.* **2013**, *3*, 1201; b) C. Deibel, T. Strobel, V. Dyakonov, *Phys. Rev. Lett.* **2009**, *103*, 036402

[47] a) V. Coropceanu, J. Cornil, D. A. da Silva Filho, Y. Olivier, R. Silbey, J.-L. Brédas, *Chem. Rev.* **2007**, *107*, 926; b) H. Dong, X. Fu, J. Liu, Z. Wang, W. Hu, *Adv. Mater.* **2013**, *25*, 6158; c) M. Mas-Torrent, C. Rovira, *Chem. Rev.* **2011**, *111*, 4833.

[48] J. Rivnay, L. H. Jimison, J. E. Northrup, M. F. Toney, R. Noriega, S. Lu, T. J. Marks, A. Facchetti, A. Salleo, *Nat. Mater.* **2009**, *8*, 952.

[49] a) S. J. Kang, S. Ahn, J. B. Kim, C. Schenck, A. M. Hiszpanski, S. Oh, T. Schiros, Y.-L. Loo, C. Nuckolls, *J. Am. Chem. Soc.* **2013**, *135*, 2207; b) A. M. Haruk, J. M. Mativetsky, *Int. J. Mol. Sci.* **2015**, *16*, 13381.

[50] P. Clancy, *Chem. Mater.* **2011**, *23*, 522.

[51] X.-X. Shen, G.-C. Han, Y.-P. Yi, *Chin. Chem. Lett.* **2016**, *27*, 1453.

Appendix 4

Reproduction of the article

"Second-Generation Azafullerene Monoadducts as Electron Acceptors in Bulk Heterojunction Solar Cells" María Pilar Montero-Rama, Aurélien Viterisi, Werther Cambarau, Caterina Stenta, Emilio Palomares, Lluis F. Marsal, Max von Delius

UNIVERSITAT ROVIRA I VIRGILI
NOVEL ELECTRON ACCEPTORS AND NEW SOLUTION PROCESSED HOLE BLOCKING LAYER FOR ORGANIC SOLAR CELLS
Caterina Stenta

764

Synthesis M. Bothe et al. Paper

# Second-Generation Azafullerene Monoadducts as Electron Acceptors in Bulk Heterojunction Solar Cells

Michael Bothe[a]
María Pilar Montero-Rama[b]
Aurélien Viterisi[b]
Werther Cambarau[c]
Caterina Stenta[b]
Emilio Palomares[c]
Lluis F. Marsal*[b]
Max von Delius*[a] (ORCID)

[a] Institute of Organic Chemistry and Advanced Materials, University of Ulm, Albert-Einstein-Allee 11, 89081 Ulm, Germany
max.vondelius@uni-ulm.de
[b] Department d'Enginyeria Electrònica, Elèctrica i Automàtica, Universitat Rovira i Virgili, Avda. Països Catalans 16, 43007 Tarragona, Spain
lluis.marsal@urv.cat
[c] Institute of Chemical Research of Catalonia (ICIQ), Avda. Països Catalans 26, 43007 Tarragona, Spain

C_{60} — 3 steps → **4 azafullerene monoadducts** X = O, S; R^1, R^2 = alkyl

Published as part of the Bürgenstock Special Section 2017
Future Stars in Organic Chemistry
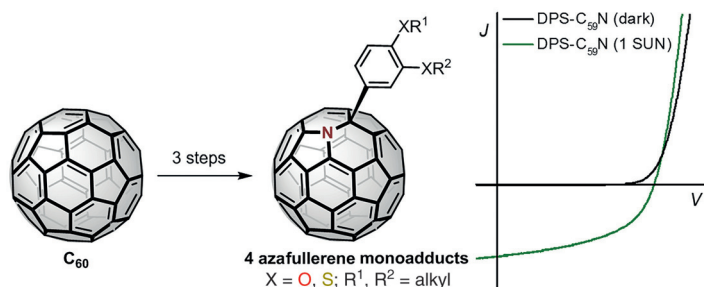
Abstract Four new azafullerene monoadducts (DPS-C_{59}N, HDP-C_{59}N, DBOP-C_{59}N, DHOP-C_{59}N) have been prepared and applied as electron acceptors in solution-processed bulk heterojunction solar cells. The four compounds were designed so that their solubility in organic solvents was maximized and that structure–property comparisons could be drawn with a previously synthesized azafullerene electron acceptor. With the photovoltaic devices that were prepared from the four azafullerenes and polymeric electron donor PTB7 we found that only one of the four new electron acceptors resulted in a power conversion efficiency that exceeded the one observed with a previously reported azafullerene monoadduct. Atomic force microscopy and electron mobility measurements suggest that azafullerenes bearing two alkyl chains lead to non-optimal film morphologies as well as electron mobilities and that future efforts should focus on single *n*-alkyl substitution.
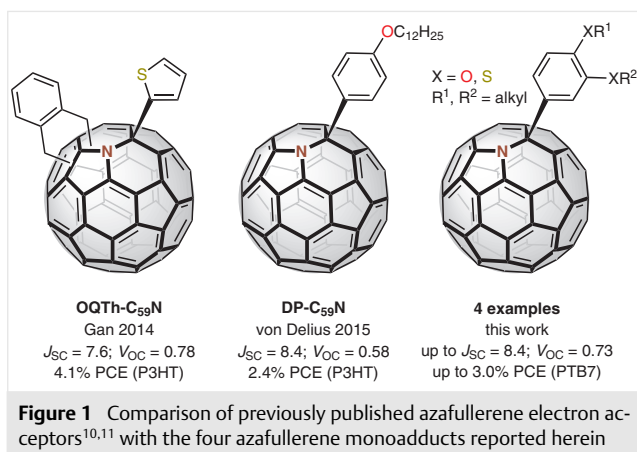
Key words fullerenes, azafullerenes, electrophilic aromatic substitution, organic photovoltaics, structure-property relationships

Azafullerenes, in which one carbon atom in the fullerene framework is replaced by a trivalent nitrogen atom, continue to be the only heterofullerenes that can be prepared in bulk quantities.[1] Since the first successful synthesis of the azafullerene dimer (C_{59}N)$_2$ in 1995,[2] dozens of azafullerene derivatives have been prepared, characterized, and applied in catalysis or organic electronics.[1a,3] Azafullerene monoadducts[4] are particularly attractive synthesis targets, because, in contrast to fullerene monoadducts, they can be prepared without competing multiple addition reactions.[5]

Fullerene monoadducts, such as the prototypical example PCBM,[6,7] are still the most widely used electron acceptors in bulk heterojunction organic solar cells (BHJ-OSCs),[8] even though the importance of non-fullerene electron acceptors is currently increasing.[9] From a molecular perspective, azafullerenes exhibit an advantage for organic photovoltaics (OPV): in contrast to fullerenes, azafullerenes possess an absorbance maximum at around 440 nm, which should lead to more efficient light harvesting and thus a higher short circuit current (J_{SC}). Indeed, we were recently able to demonstrate that an *n*-dodecyloxyphenyl-substituted azafullerene monoadduct (**DP-C_{59}N**, Figure 1),[10] leads to an increased J_{SC} in BHJ-OSCs in comparison to PCBM. Gan and coworkers had previously reported azafullerene bis-adduct **OQTh-C_{59}N** (Figure 1),[11] which due to the typical increase of the LUMO level in bisadducts[8n] outperformed PCBM with respect to the observed open circuit voltage (V_{OC}). BHJ-OSCs based on four azafullerene pentaadducts were studied by Hirsch and Wessendorf and a promising V_{OC} was observed along with a low J_{SC}.[12]

Here we report the synthesis and optoelectronic characterization of four azafullerene monoadducts (Scheme 1), which were designed so that varying the alkyl side chains should improve the blend morphology[8j,13] and ideally lead to increased J_{SC} and V_{OC} in comparison with PCBM. We tested the performance of these new electron acceptors in BHJ-OSCs in conjunction with electron donor PTB7[14,15] and we rationalized the observed performance parameters on the basis of atomic force microscopy (AFM) and electron mobility measurements.
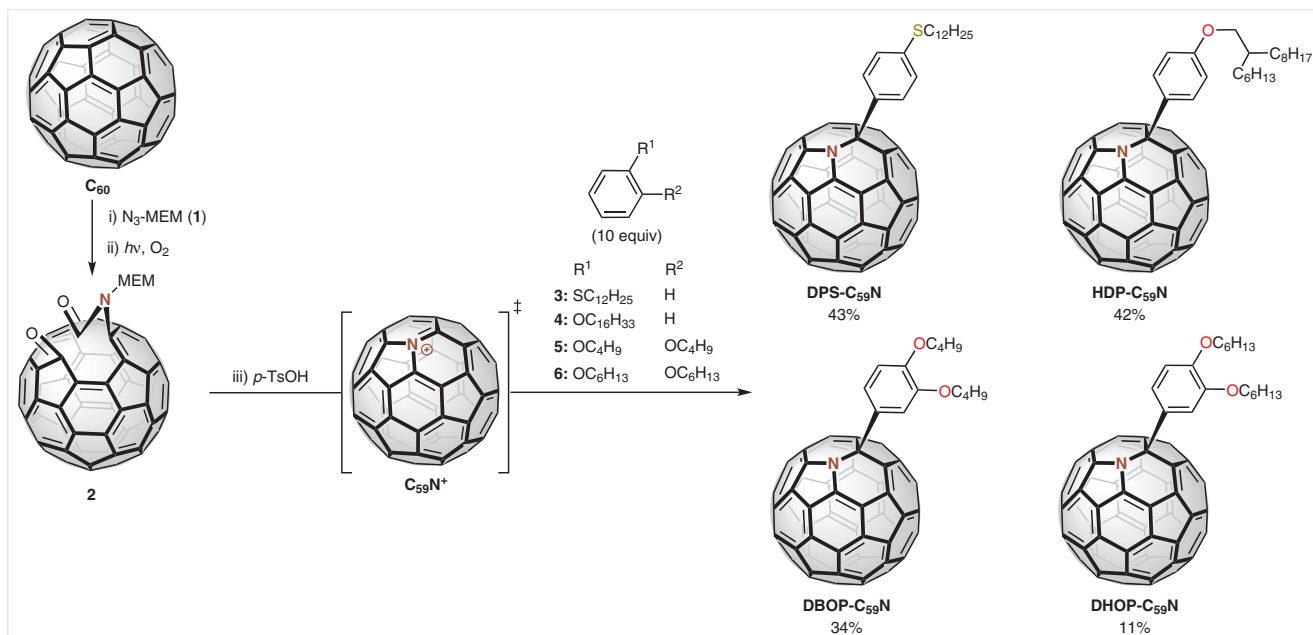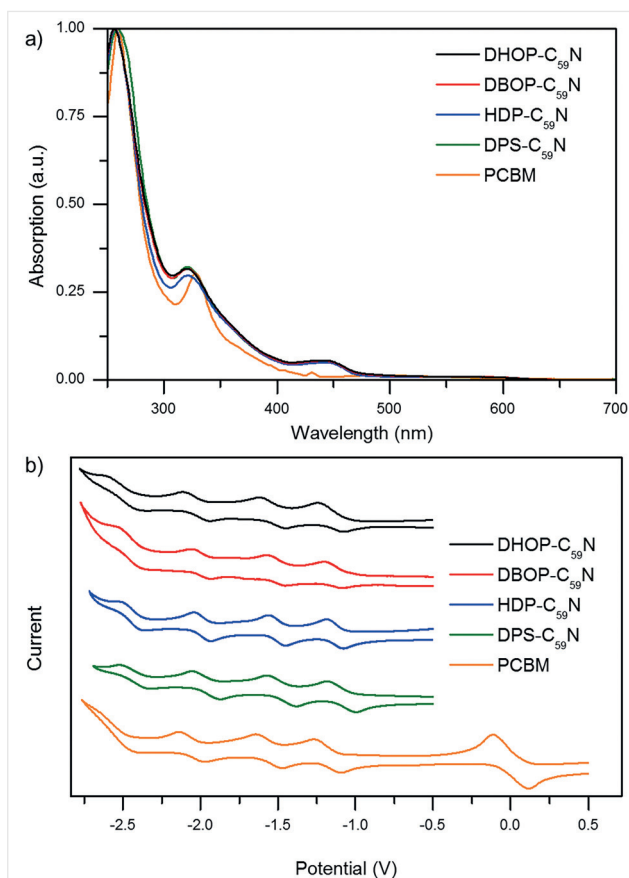
UNIVERSITAT ROVIRA I VIRGILI
NOVEL ELECTRON ACCEPTORS AND NEW SOLUTION PROCESSED HOLE BLOCKING LAYER FOR ORGANIC SOLAR CELLS
Caterina Stenta

765

Figure 1 Comparison of previously published azafullerene electron acceptors[10,11] with the four azafullerene monoadducts reported herein

Our syntheses of azafullerenes **DPS-C$_{59}$N**, **HDP-C$_{59}$N**, **DBOP-C$_{59}$N** and **DHOP-C$_{59}$N** followed a procedure previously reported by Wudl (Scheme 1).[4a–e] Cycloaddition of 2-methoxyethoxymethyl azide (MEM-N$_3$; **1**) with C$_{60}$ furnished a triazoline intermediate, which, upon loss of dinitrogen, in a photooxygenation reaction was converted into C$_{60}$-N-MEM-ketolactam **2** (1.86 g prepared during the course of this study). In a complex reaction sequence, compound **2** rearranges into the azafulleronium ion (C$_{59}$N$^+$), which is moderately reactive in electrophilic aromatic substitution reac-

tions. Hence, when using a tenfold excess of electron-rich aromatic substrates **3–6**, we were able to obtain the desired azafullerene monoadducts in isolated yields ranging from 11% to 43% (Scheme 1).

Even though the four compounds were obtained in reasonable purity after regular silica gel chromatography (ca. 95–97% pure by ^{1}H NMR and HPLC), we decided to re-purify by HPLC, because small amounts of organic impurities are known to have a significant impact on photovoltaic performance.[16] In order to minimize losses in yields, and to avoid potential agglomeration, we subjected the crude azafullerenes directly to preparative HPLC. Finally, the samples were dissolved in a minute amount of CS$_2$ and precipitated from n-pentane to remove residual grease. After this purification procedure, compounds **DPS-C$_{59}$N**, **HDP-C$_{59}$N**, **DBOP-C$_{59}$N** and **DHOP-C$_{59}$N** were obtained in excellent purity (see Supporting Information).

With the four new azafullerenes in hand, we turned our attention towards their optoelectronic characterization. As shown in Figure 2 (a), the UV-vis spectra of the four azafullerenes differ only minimally, which is not a surprising result in light of their similar structures. The comparison with PCBM, however, reveals the enhanced absorbance in the visible range of the spectrum, from which one could expect an additional contribution to J_{SC} in photovoltaic devices.

Scheme 1 Synthesis of C$_{60}$-N-MEM-ketolactam **2** and azafullerene monoadducts **DPS-C$_{59}$N**, **HDP-C$_{59}$N**, **DBOP-C$_{59}$N** and **DHOP-C$_{59}$N**. *Reagents and conditions*: (i) C$_{60}$ (6.94 mmol, 2.0 equiv), MEM-azide **1** (3.52 mmol, 1.0 equiv), 1,2-dichlorobenzene, 150 °C, 1 h (ii) hv, O$_2$, 1,2-dichlorobenzene, 150 °C, 5–7 h, 13% yield (over two steps); (iii) C$_{60}$-N-MEM-ketolactam **2** (70 μmol, 1 equiv), n-dodecyl phenyl sulfide (**3**; 700 μmol, 10 equiv), [(2-hexyldecyl)oxy]benzene (**4**; 700 μmol, 10 equiv), 1,2-di(butyloxy)benzene (**5**; 700 μmol, 10 equiv), or 1,2-di(hexyloxy)benzene (**6**; 700 μmol, 10 equiv), p-TsOH (700 μmol, 10 equiv), 1,2-dichlorobenzene, 150 °C, 15–30 min; yields: **DPS-C$_{59}$N**: 43%, **HDP-C$_{59}$N**: 42%, **DBOP-C$_{59}$N**: 34%, **DHOP-C$_{59}$N**: 11%.

UNIVERSITAT ROVIRA I VIRGILI
NOVEL ELECTRON ACCEPTORS AND NEW SOLUTION PROCESSED HOLE BLOCKING LAYER FOR ORGANIC SOLAR CELLS
Caterina Stenta

766

Figure 2 (a) Qualitative UV-vis absorption spectra of PCBM and the four new azafullerenes (CH_2Cl_2, normalized to peaks at ca. 260 nm); (b) cyclic voltammograms (1,2-dichlorobenzene, NBu_4PF_6, 0.1 M, $c \approx 10^{-3}$ mol·L^{-1}, 298 K, scan rate = 50 mV·s^{-1}, vs. Fc/Fc$^+$); a.u. = arbitrary units

Cyclic voltammetry was carried out to determine the reduction potentials of the new compounds (Figure 2, b). All four azafullerenes (first $E_{1/2}$ ca. –1.1 V vs. ferrocene/ferrocenium couple) are slightly easier to reduce than PCBM ($E_{1/2}$ –1.21 V), and the first three reduction steps were found to be fully reversible. From the reduction potentials, we calculated the LUMO levels, which are in the range from –3.65 to –3.68 eV (Table 1). These LUMO levels are very similar to the LUMO level we calculated for PCBM (–3.62 eV) and should in principle allow efficient charge transfer in combination with standard electron donors in organic solar cells.

To assess the suitability of our compounds in OPV, we fabricated BHJ-OSCs based on the small azafullerene library. PTB7 was chosen as the donor polymer, as it has a proven record of efficiency, and has shown a good adaptability to different types of acceptors.[15] A standard device architecture was used, including PEDOT:PSS as an electron blocking layer and a typical Ca/Ag cathode as depicted in Figure 3 (insert). Devices were initially optimized for donor/acceptor (D/A) ratio, active layer thickness, and additive
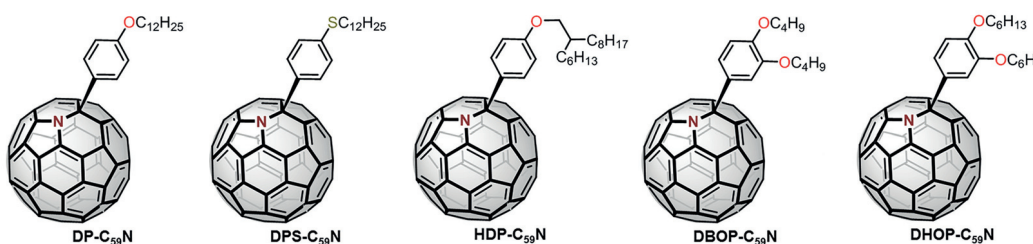
(DIO) concentration. Several solvent systems were assessed in the active layer processing optimization, resulting in chloroform offering the best solubility and film homogeneity properties. While azafullerene **DPS-C$_{59}$N** was found to be soluble at 10 mg/mL concentrations, the remaining three azafullerenes, however, showed lower solubility even after stirring overnight at 50 °C followed by prolonged sonication.
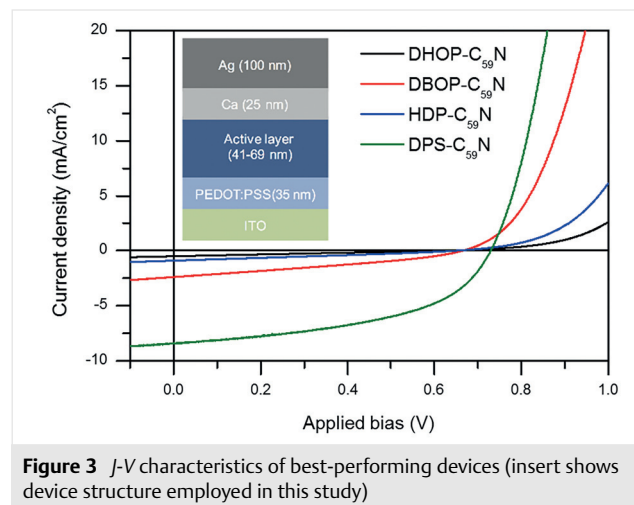
Figure 3 J-V characteristics of best-performing devices (insert shows device structure employed in this study)

The J-V characteristics of the best-performing devices are shown in Figure 3 and summarized in Table 1. It is striking at first glance that except for **DPS-C$_{59}$N**, all the other azafullerenes show rather poorer J-V characteristics. Specifically, **HDP-C$_{59}$N** and **DHOP-C$_{59}$N** show very low J_{SC} values and high shunt resistance. Although devices made from **DBOP-C$_{59}$N** show a great improvement in shunt resistance, they still have a limited J_{SC}. **DPS-C$_{59}$N**-containing devices, however, show a great improvement in all aspects of their J-V characteristics. Most importantly, the J_{SC} is much higher than in the other devices, approaching 8.5 mA/cm^2, while the fill factor (FF) reaches 49%. The V_{OC} is also significantly higher than in the lower-performing azafullerenes.

As shown in Figure 4 (a), the UV-vis spectra of the active layers made from the four azafullerenes show no notable differences in absorption features. All spectra exhibit an intense absorption band centered at around 700 nm, which can be attributed to the PTB7 fraction of the active layer. The overall absorption intensity is significantly higher in devices made from **DHOP-C$_{59}$N**. This increase in absorption is likely the result of a higher donor fraction together with a significantly thicker active layer than in devices made from the other azafullerenes (see Table 1). The slight difference in absorption intensity between these four devices does however not account for the strong difference in J_{SC}. This is further corroborated by the EQE spectra of the devices (Figure 4, b), in which the incident photon-to-current efficiency

UNIVERSITAT ROVIRA I VIRGILI
NOVEL ELECTRON ACCEPTORS AND NEW SOLUTION PROCESSED HOLE BLOCKING LAYER FOR ORGANIC SOLAR CELLS
Caterina Stenta

767

Table 1 Overview of Key Spectroscopic and Optoelectronic Properties of Previously Published Azafullerene **DP-C$_{59}$N**[10] and the Four New Azafullerenes **DPS-C$_{59}$N**, **HDP-C$_{59}$N**, **DBOP-C$_{59}$N**, and **DHOP-C$_{59}$N**, as well as Photovoltaic, AFM, and Electron Mobility Parameters

	DP-C$_{59}$N	DPS-C$_{59}$N	HDP-C$_{59}$N	DBOP-C$_{59}$N	DHOP-C$_{59}$N
$E_{1/2}^{red1}$ (V)[a]	−1.17	−1.09	−1.13	−1.14	−1.16
LUMO (eV)	−3.62	−3.68	−3.67	−3.65	−3.65
JSC (mA·cm^{-2})[b]	8.39	8.43	0.92	2.40	0.55
V_{OC} (V)[b]	0.568	0.728	0.655	0.666	0.632
FF (%)[b]	50	49	28	32	25
PCE (%)[b]	2.42	3.03	0.19	0.55	0.09
Donor/acceptor ratio		2:3	2:3	1:1	1:1
1,8-Diiodooctane (DIO) content (%)		2	2	3	3
Active layer thickness (nm)		60	69	46	41
Peak-to-peak height (nm)		36	7	30	35
RMS roughness (nm)[c]		4.8	0.8	4.2	5.7
Electron mobility (cm^2·Vs^{-1})		2.3 × 10^{-5}		9.3 × 10^{-8}	1.2 × 10^{-7}

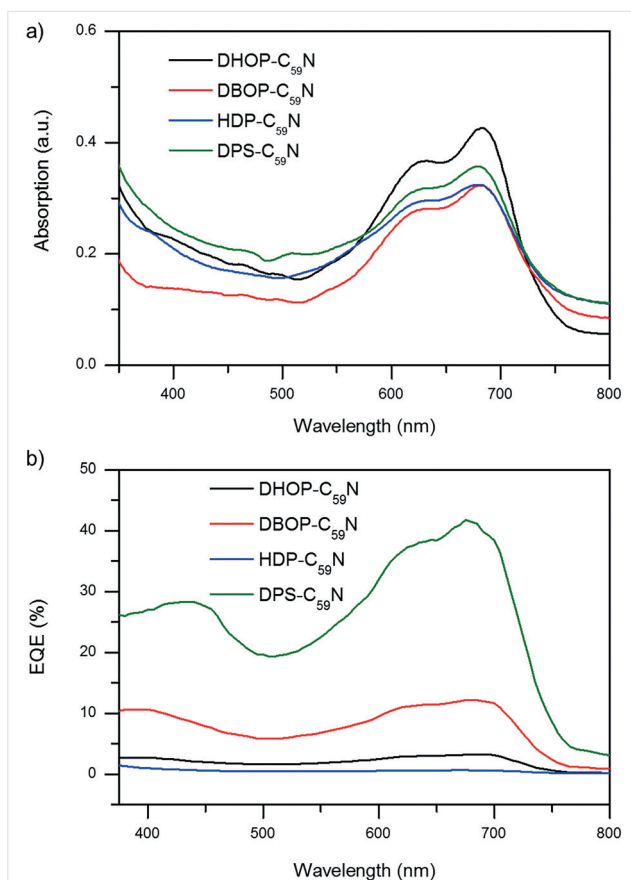[a] E vs. Fc/Fc$^+$.
[b] Values of best-performing devices measured at 1 SUN A.M. 1.5 illumination (100 mW cm^{-2}); solvent = CHCl$_3$; FF = fill factor; PCE = power conversion efficiency; see Supporting Information for further details.
[c] RMS = root mean square.

is shown to be proportional to the J_{SC} of the corresponding devices (**DPS-C$_{59}$N** outperforms the other three azafullerenes over the entire spectral range).

It is reasonable to assume that a non-optimum film morphology is likely the cause of the modest J-V characteristics, especially for compounds **DBOP-C$_{59}$N**, **DHOP-C$_{59}$N**, and **HDP-C$_{59}$N**. To shed light on the morphological characteristics of the active layers, we recorded AFM micrographs of active layers deposited under the conditions that were used to prepare solar cell devices (Figure 5). Interestingly, the topography of the active layers shows rather distinct features. **DBOP-C$_{59}$N**, **DPS-C$_{59}$N**, and **DHOP-C$_{59}$N** exhibit a strikingly high surface roughness, whereas **HDP-C$_{59}$N** as the lowest performing azafullerene exhibits a rather flat topography, as indicated by the RMS (root mean square) surface roughness values, and maximum peak-to-peak height (Table 1). The high roughness in **DBOP-C$_{59}$N**, **DPS-C$_{59}$N**, and **DHOP-C$_{59}$N** devices is indicative of the material's segregation in the bulk of the active layer, however to a different extent for each azafullerene. Indeed, the protruding domains and valleys in **DHOP-C$_{59}$N** are much larger than in all the other derivatives, while the corresponding phase imag-

es show little phase shift, which is indicative of poor materials' segregation (Figure 5, a/a′). In contrast, in the case of **DBOP-C$_{59}$N** and **DPS-C$_{59}$N**, the phase images clearly show a greater phase shift matching the regions of higher peak height (Figure 5, b/b′ and c/c′). The phase shifts observed in the active layers made from **HDP-C$_{59}$N** are, as well, indicative of some phase segregation, but to a reduced magnitude. In summary, our AFM studies suggest that segregation of donor and acceptor phases, a strict requirement for obtaining high performance devices,[17] has occurred to some extent only in films made from azafullerenes **DBOP-C$_{59}$N** and **DPS-C$_{59}$N**.

Finally, to link the morphology data with the photophysical properties of the devices, we carried out electron mobility measurements on electron-only devices fabricated under identical conditions as in OSC devices. We used the Mott–Gurney equation on the space charge–limited current region of the electron-only devices J-V characteristics measured in the dark to calculate the zero-field electron mobility of the devices in the bulk (see Supporting Information).[18]

UNIVERSITAT ROVIRA I VIRGILI
NOVEL ELECTRON ACCEPTORS AND NEW SOLUTION PROCESSED HOLE BLOCKING LAYER FOR ORGANIC SOLAR CELLS
Caterina Stenta

768

Figure 4 (a) UV-vis spectra of active layers deposited under optimum device conditions; (b) EQE spectra of best performing devices made from each azafullerene

Our analysis showed that the electron mobility follows a trend in which **DPS-C$_{59}$N** possesses the highest mobility, while **DBOP-C$_{59}$N** and **DHOP-C$_{59}$N** exhibit mobilities about two and four orders of magnitude lower than **DPS-C$_{59}$N**, respectively (Table 1). The electron mobility of **HDP-C$_{59}$N** could unfortunately not be calculated, due to the fact that no space charge region formed in the electron-only devices.

In conclusion, our studies indicate that (thio)phenol-functionalized azafullerenes substituted with single n-alkyl chains lead to favorable J-V characteristics. Although it can be difficult to draw clear structure–property relationships in OPV, it is reasonable to deduce from our studies that two-fold n-alkyl-substituted and branched-alkyl-substituted derivatives lead to poorer characteristics. This poor device performance can be attributed to some extent to the intrinsically lower electron mobilities in bis-functionalized azafullerenes, which is associated with the fullerenes' packing in the solid state and poorer film-forming properties. The low mobility of the fullerenes restricts the thickness of the active layer to very thin layers, limiting the absorption of the active layer to a great extent and therefore the J_{SC}. Moreover, the extremely rough nature of the active layer surface, as shown from the AFM images, is likely to induce increased surface recombination, leading to deteriorated J-V characteristics, i.e. low FF and suboptimum shunt and series resistance. Finally, poor segregation (either too large, e.g. **DHOP-C$_{59}$N**, or too small domains, e.g. **DBOP-C$_{59}$N** and **HDP-C$_{59}$N**) is likely to impose a limit on the exciton splitting yield, further limiting the J_{SC}. Further studies on azafullerene-based OSCs should thus focus on single n-alkyl chain functionalization.
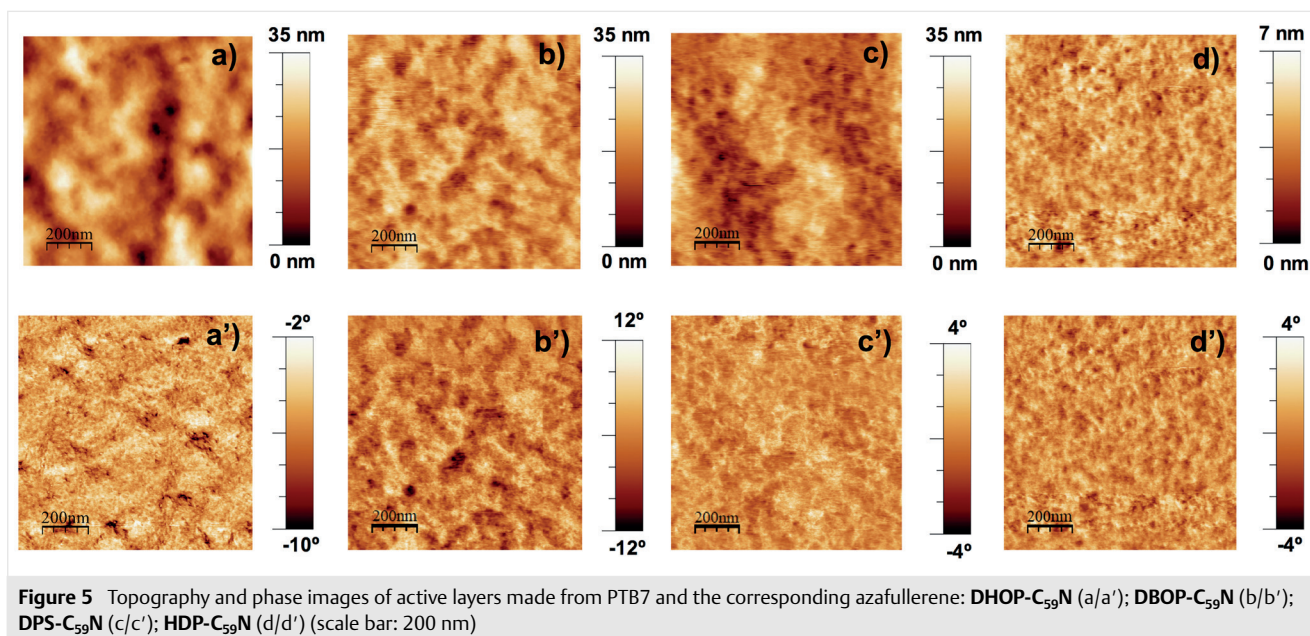
Figure 5 Topography and phase images of active layers made from PTB7 and the corresponding azafullerene: **DHOP-C$_{59}$N** (a/a'); **DBOP-C$_{59}$N** (b/b'); **DPS-C$_{59}$N** (c/c'); **HDP-C$_{59}$N** (d/d') (scale bar: 200 nm)

UNIVERSITAT ROVIRA I VIRGILI
NOVEL ELECTRON ACCEPTORS AND NEW SOLUTION PROCESSED HOLE BLOCKING LAYER FOR ORGANIC SOLAR CELLS
Caterina Stenta

769

Unless otherwise stated, all reagents were purchased from commercial sources and used without further purification. C_{60} and PCBM were purchased from IoLiTec Ionic Liquids Technologies GmbH. HPLC grade solvents were used for reactions with fullerenes. ^1H and ^{13}C NMR spectra were recorded on Bruker Avance 300 (^1H: 300 MHz, ^{13}C: 75 MHz), Bruker Avance 400 (^1H: 400 MHz, ^{13}C: 100 MHz), and Jeol EX400 (^1H: 400 MHz, ^{13}C: 100 MHz) instruments at room temperature. Chemical shifts are given in parts per million and referenced to residual solvent (^1H: $CDCl_3$, 7.24 ppm; ^{13}C: $CDCl_3$: 77 ppm). Qualitative UV-vis measurements were carried out on a Varian Cary 5000 UV-vis-NIR spectrophotometer of samples in dichloromethane at room temperature. Mass spectra were obtained on Bruker Maxis 4G (HRMS-APPI, toluene) and Thermo Scientific ISQ LT (EI) instruments. Cyclic voltammograms were recorded under nitrogen or argon atmosphere by using a BAS CV-50W potentiostat and a three electrode set-up (working electrode: Pt disk, auxiliary electrode: Pt wire, reference electrode: $Ag/AgNO_3$ or silver wire, supporting electrolyte: tetrabutylammonium hexafluorophosphate (0.1 mol/L), solvent: 1,2-dichlorobenzene, scan rate: 50 mV/sec). Potentials are referenced to the ferrocene/ferrocenium couple as internal standard (Fc/Fc^+). Approximate LUMO energy levels vs. vacuum were calculated according to the equation $E_{LUMO} = -(4.8 + E_{1/2}^{red1})$ eV with $E_{1/2}^{red1} = (E_{p,c} + E_{p,a})/2$. Analytical HPLC was conducted on a Shimadzu LCMS 2020 (column: Cosmosil Buckyprep, toluene, 1.0 mL/min). Crude azafullerenes were purified by means of preparative HPLC (Cosmosil Buckyprep, toluene, 18 mL/min). Precursor compounds n-dodecyl phenyl sulfide (**3**),[19] 7-(bromomethyl)pentadecane,[20] 1,2-di(butyloxy)benzene (**5**),[21] 1,2-di(hexyloxy)benzene (**6**),[21] 2-methoxyethoxymethyl azide (**1**),[4e] and C_{60}-N-MEM-ketolactam (**2**)[4e] were synthesized according to published procedures. The preparation of solar cells is described in the Supporting Information.

[(2-Hexyldecyl)oxy]benzene (4)

In an oven-dried two-neck round-bottom flask, Cs_2CO_3 (15.6 g, 48.0 mmol) was dissolved in anhydrous DMF (100 mL) and the mixture was heated to reflux under a nitrogen atmosphere. After 15 min, phenol (3.76 g, 40.0 mmol), and, after an additional 40 min, 7-(bromomethyl)pentadecane (**S1**) (202 g, 66.3 mmol) were added. The progress of the reaction was monitored via TLC and after complete conversion of phenol, the reaction mixture was cooled to r.t. and the solvent was removed under reduced pressure. The residue was taken up in CH_2Cl_2, filtered, and washed with water and brine. Purification by column chromatography (silica gel, hexanes) afforded the title compound as a colorless oil.

Yield: 10.8 g (33.9 mmol, 85%).

^1H NMR (400 MHz, 298 K, $CDCl_3$): δ = 7.37–7.33 (m, 2 H), 7.02–6.98 (m, 3 H), 3.92 (d, ^3J = 5.7 Hz, 2 H), 1.91–1.86 (m, 1 H), 1.61–1.31 (m, 24 H), 1.02–0.99 (m, 6 H).

^{13}C NMR (100 MHz, 298 K, $CDCl_3$): δ = 159.4, 129.3, 120.3, 114.5, 70.7, 38.0, 32.0, 31.9, 31.5, 31.4, 30.1, 29.8, 29.6, 29.4, 26.9, 26.9, 22.7, 14.1.

MS (EI): m/z calcd for $C_{22}H_{38}O^+$: 318.3; found: 318.3 [M^+], 225.2 [M – OC_6H_5]$^+$.

Azafullerene Monoadducts; General Procedure

The syntheses were carried out in parallel, because we observed significantly reduced yields upon scale-up. In four oven-dried round-bottom flasks (50 mL), **2** (4 × 60 mg, 4 × 70 µmol) was dissolved in 1,2-dichlorobenzene (4 × 15 mL, analytical purity). Subsequently, **3** (4 × 195 mg, 4 × 700 µmol) or **4** (4 × 223 mg, 4 × 700 µmol) or **5** (4 ×

156 mg, 4 × 700 µmol) or **6** (4 × 198 mg, 4 × 700 µmol) and TsOH (4 × 133 mg, 700 µmol) were added and the reaction mixtures were stirred at 150 °C on a preheated heat-on block until no C_{60}-N-MEM-ketolactam **2** could be detected by TLC (ca. 15–30 min). Alternatively, the reaction progress can be monitored by analytical HPLC (Cosmosil, toluene, 1 mL/min). After quick cooling to r.t. by means of an ice bath, the reaction mixtures were combined and directly subjected to flash column chromatography (silica gel, toluene, HPLC grade). The solvent was removed under reduced pressure and the residues were purified by preparative HPLC (Cosmosil, toluene, 18 mL/min). The crude product should never be completely dried prior to HPLC purification in order to reduce losses caused by filtration by syringe filter. Finally, the product was dissolved in a minute amount of CS_2 and reprecipitated from n-pentane. All target compounds were isolated as dark brown solids.

n-Dodecyl Phenyl Sulfide Azafullerene (DPS-$C_{59}N$)

Yield: 119 mg (119 µmol, 43%).

^1H NMR (400 MHz, 298 K, $CDCl_3$): δ = 8.76 (d, ^3J = 8.2 Hz, 2 H), 7.79 (d, ^3J = 8.2 Hz, 2 H), 3.12 (t, ^3J = 7.4 Hz, 2 H), 1.81 (quint, 2 H), 1.56–1.49 (m, 2 H), 1.42–1.19 (m, 16 H), 0.88 (m, 3 H).

^{13}C NMR (100 MHz, 298 K, $CDCl_3/CS_2$ 2:1): δ = 154.4, 148.6, 147.8, 147.6, 147.6, 147.3, 147.2, 146.6, 146.4, 146.2, 145.9, 145.7, 145.0, 145.0, 144.5, 144.3, 144.0, 143.1, 142.8, 142.1, 141.8, 141.5, 141.4, 141.0, 140.9, 140.0, 139.8, 138.1, 137.5, 133.0, 129.1, 127.7, 124.1, 82.7, 33.2, 32.0, 29.8, 29.8, 29.7, 29.5, 29.4, 29.2, 29.2, 22.8, 14.2.

HRMS (APPI): calcd for $C_{77}H_{29}NS$: 999.2015; found: 999.2007.

[(2-Hexyldecyl)oxy]benzene Azafullerene (HDP-$C_{59}N$)

Yield: 121 mg (116 µmol, 42%).

^1H NMR (400 MHz, 298 K, $CDCl_3/CS_2$ 2:1): δ = 8.69 (d, ^3J = 8.8 Hz, 2 H), 7.33 (d, ^3J = 8.8 Hz, 2 H), 4.03 (d, ^3J = 5.6 Hz, 2 H), 1.95–1.86 (m, 1 H), 1.61–1.28 (m, 24 H), 0.94–0.89 (m, 6 H).

^{13}C NMR (100 MHz, 298 K, $CDCl_3/CS_2$ 2:1): δ = 160.4, 154.4, 149.0, 147.8, 147.6, 147.6, 147.2, 146.6, 146.4, 146.2, 145.9, 145.8, 145.7, 145.0, 145.0, 144.5, 144.3, 144.0, 143.1, 142.7, 142.0, 141.8, 141.5, 141.4, 141.0, 140.9, 139.7, 137.5, 133.0, 133.0, 128.6, 124.1, 115.8, 82.6, 71.2, 38.1, 32.0, 32.0, 31.5, 31.5, 30.2, 29.9, 29.8, 29.5, 27.1, 27.0, 22.9, 22.8, 14.3, 14.3.

HRMS (APPI): calcd for $C_{81}H_{37}NO$: 1039.2870; found: 1039.2867.

1,2-Di(butyloxy)benzene Azafullerene (DBOP-$C_{59}N$)

Yield: 91 mg (96 µmol, 34%).

^1H NMR (400 MHz, 298 K, $CDCl_3/CS_2$, 2:1): δ = 8.30 (m, 2 H), 7.30 (m, 1 H), 4.31 (t, ^3J = 6.4 Hz, 2 H), 4.21 (t, ^3J = 6.4 Hz, 2 H), 1.99–1.91 (m, 4 H), 1.68–1.58 (m, 4 H), 1.09–1.04 (m, 6 H).

^{13}C NMR (100 MHz, 298 K, $CDCl_3/CS_2$ 2:1): δ = 154.4, 150.5, 150.4, 148.9, 147.8, 147.7, 147.6, 147.2, 146.6, 146.6, 146.4, 146.2, 146.2, 145.9, 145.8, 145.7, 145.7, 145.0, 145.0, 144.5, 144.3, 144.0, 143.1, 142.8, 142.1, 141.8, 141.6, 141.4, 141.0, 140.9, 139.8, 137.6, 133.7, 132.9, 128.9, 128.1, 125.2, 124.1, 120.1, 114.2, 112.8, 82.8, 69.4, 69.0, 31.6, 31.4, 19.5, 19.5, 14.1, 14.0.

HRMS (APPI): calcd for $C_{73}H_{21}NO_2$: 943.1567; found: 943.1562.

1,2-Di(hexyloxy)benzene Azafullerene (DHOP-$C_{59}N$)

Yield: 30 mg (30 µmol, 11%).

UNIVERSITAT ROVIRA I VIRGILI
NOVEL ELECTRON ACCEPTORS AND NEW SOLUTION PROCESSED HOLE BLOCKING LAYER FOR ORGANIC SOLAR CELLS
Caterina Stenta

770

^{1}H NMR (400 MHz, 298 K, CDCl$_3$/CS$_2$ 2:1): δ = 8.31 (m, 2 H), 7.32 (m, 1 H), 4.31 (t, ^3J = 6.5 Hz, 2 H), 4.21 (t, ^3J = 6.5 Hz, 2 H), 2.01–1.92 (m, 4 H), 1.64–1.57 (m, 4 H), 1.44–1.39 (m, 8 H), 0.96 (t, ^3J = 7.0 Hz, 3 H), 0.93 (t, ^3J = 7.0 Hz, 3 H).

^{13}C NMR (100 MHz, 298 K, CDCl$_3$/CS$_2$ 2:1): δ = 154.5, 150.6, 150.4, 149.0, 147.9, 147.7, 147.7, 147.3, 146.7, 146.5, 146.3, 145.9, 145.9, 145.7, 145.1, 145.1, 144.6, 144.4, 144.1, 143.2, 142.8, 142.2, 141.9, 141.6, 141.5, 141.0, 140.9, 139.8, 137.6, 133.7, 133.0, 129.0, 128.5, 128.2, 125.2, 124.1, 120.0, 144.3, 112.9, 82.8, 69.7, 69.4, 32.0, 31.7, 31.7, 31.4, 29.8, 29.7, 29.5, 29.4, 29.4, 25.9, 25.9, 22.8, 14.2, 14.1.

HRMS (APPI): calcd for C$_{77}$H$_{29}$NO$_2$: 999.2193; found: 999.2192.

Funding Information

Acknowledgment

Supporting Information

Supporting information for this article is available online at https://doi.org/10.1055/s-0036-1591871.

References

(1) (a) von Delius, M.; Hirsch, A. In *Chemical Synthesis and Applications of Graphene and Carbon Materials*; Antonietti, M.; Müllen, K., Eds.; Wiley-VCH: Weinheim, **2017**, 191. (b) Vostrowsky, O.; Hirsch, A. *Chem. Rev.* **2006**, *106*, 5191.

(2) Hummelen, J. C.; Knight, B.; Pavlovich, J.; González, R.; Wudl, F. *Science* **1995**, *269*, 1554.

(3) (a) Kumashiro, R.; Tanigaki, K.; Ohashi, H.; Tagmatarchis, N.; Kato, H.; Shinohara, H.; Akasaka, T.; Kato, K.; Aoyagi, S.; Kimura, S.; Takata, M. *Appl. Phys. Lett.* **2004**, *84*, 2154. (b) Fei, X.; Neilson, J.; Li, Y.; Lopez, V.; Garrett, S. J.; Gan, L.; Gao, H.-J.; Gao, L. *Nano Lett.* **2017**, *17*, 2887. (c) Hashikawa, Y.; Murata, M.; Wakamiya, A.; Murata, Y. *J. Am. Chem. Soc.* **2016**, *138*, 4096. (d) Coro, J.; Suárez, M.; Silva, L. S. R.; Eguiluz, K. I. B.; Salazar-Banda, G. R. *Int. J. Hydrogen Energy* **2016**, *41*, 17944. (e) Rotas, G.; Tagmatarchis, N. *Chem. Eur. J.* **2016**, *22*, 1206. (f) Kaneko, T.; Li, Y.; Nishigaki, S.; Hatakeyama, R. *J. Am. Chem. Soc.* **2008**, *130*, 2714.

(4) (a) Bellavia-Lund, C.; González, R.; Hummelen, J. C.; Hicks, R. G.; Sastre, A.; Wudl, F. *J. Am. Chem. Soc.* **1997**, *119*, 2946. (b) Nuber, B.; Hirsch, A. *Chem. Commun.* **1998**, 405. (c) Hauke, F.; Hirsch, A. *Tetrahedron* **2001**, *57*, 3697. (d) Vougioukalakis, G. C.; Roubelakis, M. M.; Orfanopoulos, M. *J. Org. Chem.* **2010**, *75*, 4124. (e) von Delius, M.; Hauke, F.; Hirsch, A. *Eur. J. Org. Chem.* **2008**, 4109. (f) Roubelakis, M. M.; Vougioukalakis, G. C.; Nye, L. C.; Drewello, T.; Orfanopoulos, M. *Tetrahedron* **2010**, *66*, 9363.

(g) Hauke, F.; Vostrowsky, O.; Hirsch, A.; Quaranta, A.; Leibl, W.; Leach, S.; Edge, R.; Navaratnam, S.; Bensasson, R. V. *Chem. Eur. J.* **2006**, *12*, 4813. (h) Vougioukalakis, G. C.; Hatzimarinaki, M.; Lykakis, I. N.; Orfanopoulos, M. *J. Org. Chem.* **2006**, *71*, 829. (i) Fu, W.; Zhang, J.; Fuhrer, T.; Champion, H.; Furukawa, K.; Kato, T.; Mahaney, J. E.; Burke, B. G.; Williams, K. A.; Walker, K.; Dixon, C.; Ge, J.; Shu, C.; Harich, K.; Dorn, H. C. *J. Am. Chem. Soc.* **2011**, *133*, 9741.

(5) (a) Hirsch, A.; Brettreich, M. *Fullerenes – Chemistry and Reactions*; Wiley-VCH: Weinheim, **2004**. (b) *Fullerenes: Principles and Applications*, 2nd ed.; Langa, F.; Nierengarten, J.-F., Eds.; RSC Publishing: Cambridge, **2011**.

(6) PCBM = [6,6]-phenyl-C$_{61}$-butyric acid methyl ester.

(7) Hummelen, J. C.; Knight, B. W.; LePeq, F.; Wudl, F.; Yao, J.; Wilkins, C. L. *J. Org. Chem.* **1995**, *60*, 532.

(8) (a) Dang, M. T.; Hirsch, L.; Wantz, G. *Adv. Mater.* **2011**, *23*, 3597. (b) Deibel, C.; Dyakonov, V. *Rep. Prog. Phys.* **2010**, *73*, 096401. (c) Cai, W.; Gong, X.; Cao, Y. *Sol. Energy Mater. Sol. Cells* **2010**, *94*, 114. (d) Mishra, A.; Bäuerle, P. *Angew. Chem. Int. Ed.* **2012**, *51*, 2020. (e) Ameri, T.; Li, N.; Brabec, C. J. *Energy Environ. Sci.* **2013**, *6*, 2390. (f) Ameri, T.; Khoram, P.; Brabec, C. J. *Adv. Mater.* **2013**, *25*, 4245. (g) Darling, S. B.; You, F. *RSC Adv.* **2013**, *3*, 17633. (h) Mazzio, K. A.; Luscombe, C. K. *Chem. Soc. Rev.* **2015**, *44*, 78. (i) Kang, H.; Kim, G.; Kim, J.; Kwon, S.; Kim, H.; Lee, K. *Adv. Mater.* **2016**, *28*, 7821. (j) Heeger, A. J. *Adv. Mater.* **2014**, *26*, 10. (k) Delgado, J. L.; Bouit, P.-A.; Filippone, S.; Herranz, M. Á.; Martín, N. *Chem. Commun.* **2010**, *46*, 4853. (l) He, Y.; Li, Y. *Phys. Chem. Chem. Phys.* **2011**, *13*, 1970. (m) Ganesamoorthy, R.; Sathiyan, G.; Sakthivel, P. *Sol. Energy Mater. Sol. Cells* **2017**, *161*, 102. (n) Li, Y. *Chem. Asian J.* **2013**, *8*, 2316. (o) Morinaka, Y.; Nobori, M.; Murata, M.; Wakamiya, A.; Sagawa, T.; Yoshikawa, S.; Murata, Y. *Chem. Commun.* **2013**, *49*, 3670. (p) Schroeder, B. C.; Li, Z.; Brady, M. A.; Faria, G. C.; Ashraf, R. S.; Takacs, C. J.; Cowart, J. S.; Duong, D. T.; Chiu, K. H.; Tan, C.-H.; Cabral, J. T.; Salleo, A.; Chabinyc, M. L.; Durrant, J. R.; McCulloch, I. *Angew. Chem. Int. Ed.* **2014**, *53*, 12870. (q) Wienk, M. M.; Kroon, J. M.; Verhees, W. J. H.; Knol, J.; Hummelen, J. C.; van Hal, P. A.; Janssen, R. A. J. *Angew. Chem. Int. Ed.* **2013**, *42*, 3371.

(9) (a) Lin, Y.; Zhan, X. *Mater. Horiz.* **2014**, *1*, 470. (b) Zhan, C.; Zhang, X.; Yao, J. *RSC Adv.* **2015**, *5*, 93002. (c) Kim, T.; Kim, J.-H.; Kang, T. E.; Lee, C.; Kang, H.; Shin, M.; Wang, C.; Ma, B.; Jeong, U.; Kim, T.-S.; Kim, B. J. *Nat. Commun.* **2015**, *6*, 8547. (d) Bin, H.; Gao, L.; Zhang, Z.-G.; Yang, Y.; Zhang, Y.; Zhang, C.; Chen, S.; Xue, L.; Yang, C.; Xiao, M.; Li, Y. *Nat. Commun.* **2016**, *7*, 13651. (e) Holliday, S.; Ashraf, R. S.; Wadsworth, A.; Baran, D.; Yousaf, S. A.; Nielsen, C. B.; Tan, C.-H.; Dimitrov, S. D.; Shang, Z.; Gasparini, N.; Alamoudi, M.; Laquai, F.; Brabec, C. J.; Salleo, A.; Durrant, J. R.; McCulloch, I. *Nat. Commun.* **2016**, *7*, 11585. (f) Fan, Y.; Barlow, S.; Zhang, S.; Lin, B.; Marder, S. R. *RSC Adv.* **2016**, *6*, 70493. (g) Bin, H.; Zhang, Z.-G.; Gao, L.; Chen, S.; Zhong, L.; Xue, L.; Yang, C.; Li, Y. *J. Am. Chem. Soc.* **2016**, *138*, 4657. (h) Eftaiha, A. F.; Sun, J.-P.; Hill, I. G.; Welch, G. C. *J. Mater. Chem. A* **2014**, *2*, 1201. (i) Fernández-Lázaro, F.; Zink-Lorre, N.; Sastre-Santos, Á. *J. Mater. Chem A* **2016**, *4*, 9336. (j) Li, S.; Liu, W.; Li, C.-Z.; Shi, M.; Chen, H. *Small* **2017**, *13*, 1701120. (k) Liang, N.; Jiang, W.; Hou, J.; Wang, Z. *Mater. Chem. Front.* **2017**, *1*, 1291. (l) Kuzmich, A.; Padula, D.; Ma, H.; Troisi, A. *Energy Environ. Sci.* **2017**, *10*, 395. (m) Li, S.; Zhang, Z.; Shi, M.; Li, C.-Z.; Chen, H. *Phys. Chem. Chem. Phys.* **2017**, *19*, 3440.

(10) Cambarau, W.; Fritze, U. F.; Viterisi, A.; Palomares, E.; von Delius, M. *Chem. Commun.* **2015**, *51*, 1128.

(11) Xiao, Z.; He, D.; Zuo, C.; Gan, L.; Ding, L. *RSC Adv.* **2014**, *4*, 24029.

UNIVERSITAT ROVIRA I VIRGILI
NOVEL ELECTRON ACCEPTORS AND NEW SOLUTION PROCESSED HOLE BLOCKING LAYER FOR ORGANIC SOLAR CELLS
Caterina Stenta

771

Synthesis M. Bothe et al. **Paper**

(12) Wessendorf, C. D.; Eigler, R.; Eigler, S.; Hanisch, J.; Hirsch, A.; Ahlswede, E. *Sol. Energy Mater. Sol. Cells* **2015**, *132*, 450.

(13) (a) Fernández, D.; Viterisi, A.; Ryan, J. W.; Gispert-Guirado, F.; Vidal, S.; Filippone, S.; Martín, N.; Palomares, E. *Nanoscale* **2014**, *6*, 5871. (b) Heremans, P.; Cheyns, D.; Rand, B. P. *Acc. Chem. Res.* **2009**, *42*, 1740. (c) Sajjad, M. T.; Ward, A. J.; Kästner, C.; Ruseckas, A.; Hoppe, H.; Samuel, I. D. W. *J. Phys. Chem. Lett.* **2015**, *6*, 3054. (d) Dang, M. T.; Hirsch, L.; Wantz, G.; Wuest, J. D. *Chem. Rev.* **2013**, *113*, 3734. (e) Zhang, P.; Li, C.; Li, Y.; Yang, X.; Chen, L.; Xu, B.; Tian, W.; Tu, Y. *Chem. Commun.* **2013**, *49*, 4917. (f) Faist, M. A.; Shoaee, S.; Tuladhar, S.; Dibb, G. F. A.; Foster, S.; Gong, W.; Kirchartz, T.; Bradley, D. D. C.; Durrant, J. R.; Nelson, J. *Adv. Energy Mater.* **2013**, *3*, 744.

(14) PTB7 = poly([4,8-bis(2-ethylhexyloxy)benzo(1,2-*b*:4,5-*b'*)dith-iophene-2,6-diyl]{3-fluoro-2-[(2-ethylhexyl)carbonyl]thieno-[3,4-*b*]thiophenediyl)

(15) (a) Liang, Y.; Xu, Z.; Xia, J.; Tsai, S.-T.; Wu, Y.; Li, G.; Ray, C.; Yu, L. *Adv. Mater.* **2010**, *22*, E135. (b) He, Z.; Zhong, C.; Su, S.; Xu, M.; Wu, H.; Cao, Y. *Nat. Photonics* **2012**, *6*, 591. (c) Liu, F.; Zhao, W.; Tumbleston, J. R.; Wang, C.; Gu, Y.; Wang, D.; Briseno, A. L.; Ade, H.; Russell, T. P. *Adv. Energy Mater.* **2014**, *4*, 1301377. (d) Guo, S.; Ning, J.; Körstgens, V.; Yao, Y.; Herzig, E. M.; Roth, S. V.; Müller-Buschbaum, P. *Adv. Energy Mater.* **2015**, *5*, 1401315. (e) Guerrero, A.; Montcada, N. F.; Ajuria, J.; Etxebarria, I.; Pacios, R.; Garcia-Belmonte, G.; Palomares, E. *J. Mater. Chem. A* **2013**, *1*, 12345. (f) Lu, L.; Yu, L. *Adv. Energy Mater.* **2014**, *26*, 4413.

(g) Park, S.; Jeong, J.; Hyun, G.; Kim, M.; Lee, H.; Yi, Y. *Sci. Rep.* **2016**, *6*, 35262. (h) Cho, S.; Rolczynski, B. S.; Xu, T.; Yu, L.; Chen, L. X. *J. Phys. Chem. B* **2015**, *119*, 7447.

(16) (a) Kaake, L.; Dang, X.-D.; Leong, W. L.; Zhang, Y.; Heeger, A.; Nquyen, T.-Q. *Adv. Mater.* **2013**, *25*, 1706. (b) Usluer, Ö.; Abbas, M.; Wantz, G.; Vignau, L.; Hirsch, L.; Grana, E.; Brochon, C.; Cloutet, E.; Hadziioannou, G. *ACS Macro Lett.* **2014**, *3*, 1134. (c) Nikiforov, M. P.; Lai, B.; Chen, S.; Schaller, R. D.; Strzalka, J.; Maser, J.; Darling, S. B. *Energy Environ. Sci.* **2013**, *6*, 1513. (d) Cowan, S. R.; Leong, W. L.; Banerji, N.; Dennler, G.; Heeger, A. J. *Adv. Funct. Mater.* **2011**, *21*, 3083.

(17) (a) Xu, Z.; Chen, L.-M.; Yang, G.; Huang, C.-H.; Hou, J.; Wu, Y.; Li, G.; Hsu, C.-S.; Yang, Y. *Adv. Funct. Mater.* **2009**, *19*, 1227. (b) Ruderer, M. A.; Guo, S.; Meier, R.; Chiang, H.-Y.; Körstgens, V.; Wiedersich, J.; Perlich, J.; Roth, S. V.; Müller-Buschbaum, P. *Adv. Funct. Mater.* **2011**, *21*, 3382.

(18) (a) Mihailetchi, V. D.; van Duren, J. K. J.; Blom, P. W. M.; Hummelen, J. C.; Janssen, R. A. J.; Kroon, J. M.; Rispens, M. T.; Verhees, W. J. H.; Wienk, M. M. *Adv. Funct. Mater.* **2003**, *13*, 43. (b) Blom, P. W. M.; Mihailetchi, V. D.; Koster, L. J. A.; Markov, D. E. *Adv. Mater.* **2007**, *19*, 1551.

(19) Salvatore, R. N.; Smith, R. A.; Nischwitz, A. K.; Gavin, T. *Tetrahedron Lett.* **2005**, *46*, 8931.

(20) Guo, X.; Ortiz, R. P.; Zheng, Y.; Kim, M.-G.; Zhang, S.; Hu, Y.; Lu, G.; Facchetti, A.; Marks, T. J. *J. Am. Chem. Soc.* **2011**, *133*, 13685.

(21) Zhang, Q.; Peng, H.; Zhang, G.; Lu, Q.; Chang, J.; Dong, Y.; Shi, X.; Wei, J. *J. Am. Chem. Soc.* **2014**, *136*, 5057.

Bibliography

[1] Godfrey B., Renewable Energy: Power for a Sustainable Future, OUP Oxford, 2012.

[2] https://www.ise.fraunhofer.de/, January 2018.

[3] https://www.nrel.gov/pv/, March 2018.

[4] Brian O'Regan; Michael Grätzel (24 October 1991). "A low-cost, high-efficiency solar cell based on dye-sensitized colloidal TiO2 films". Nature. 353 (6346): 737–740.

[5] Stenta, Caterina. Study and characterization of the ZnPc:C 60 /MoO x interface in organic solar cells by means of photo electron sp ectroscopy. Master thesis, April 2013.

[6] Wright, Matthew, and Ashraf Uddin. "Organic—inorganic hybrid solar cells: A comparative review." Solar energy materials and solar cells 107 (2012): 87-111.

[7] Kubař, Tomáš, and Marcus Elstner. "A hybrid approach to simulation of electron transfer in complex molecular systems." Journal of The Royal Society Interface 10.87 (2013): 20130415.

[8] Mahendra, Ajit Kumar, and Ram Kumar Singh. "Onsager reciprocity principle for kinetic models and kinetic schemes." arXiv preprint arXiv:1308.4119 (2013).

[9] Ryan, James. Organic and Hybrid Optoelectronic Devices: Understanding Key Loss Mechanisms. Doctoral thesis, 2013.

[10] Petritsch, Klaus. Organic solar cell architectures. Cambridge and Graz 2000.

[11] Elumalai, Naveen Kumar, and Ashraf Uddin. "Open circuit voltage of organic solar cells: an in-depth review." Energy & Environmental Science 9.2 (2016): 391-410.

[12] Scharber, Markus C., et al. Design rules for donors in bulk-hetero junction solar cellsTowards 10% energy-conversion eciency. Advanced Materials, 2006, 18.6: 789-794.

[13] Bundgaard, Eva; Krebs, Frederik C. Low band gap p olymers for organic photovoltaics. Solar Energy Materials and Solar Cells, 2007, 91.11: 954-985.

[14] Sariciftci, N. S., et al. Photoinduced electron transfer from a conducting polymer to buckmin- sterfullerene. Science, 1992, 258.5087: 1474-1476.

[15] Akamatu, Hideo, Hiroo Inokuchi, and Yoshio Matsunaga. "Electrical conductivity of the perylene–bromine complex." Nature 173.4395 (1954): 168.

[16] Chiang, C. K., et al. "Conducting polymers: Halogen doped polyacetylene." The Journal of Chemical Physics 69.11 (1978): 5098-5104.

[17] Shirakawa, H., et al. "AJ Heeger J. Chem. Soc." Chem. Commun 578 (1977): 31.

[18] Gandini, Alessandro, and Mohamed Naceur Belgacem. "Furans in polymer chemistry." Progress in Polymer Science 22.6 (1997): 1203-1379.

[19] Facchetti, Antonio. "Polymer donor–polymer acceptor (all-polymer) solar cells." Materials Today 16.4 (2013): 123-132.

[20] Scharber, Markus Clark, and Niyazi Serdar Sariciftci. "Efficiency of bulk-heterojunction organic solar cells." Progress in polymer science 38.12 (2013): 1929-1940.

[21] Lu, Luyao, et al. "Status and prospects for ternary organic photovoltaics." Nature Photonics 9.8 (2015): 491.

[22] Mühlbacher, David, et al. "High photovoltaic performance of a low-bandgap polymer." Advanced Materials 18.21 (2006): 2884-2889.

[23] Hou, Jianhui, et al. "Synthesis, characterization, and photovoltaic properties of a low band gap polymer based on silole-containing polythiophenes and 2, 1, 3-benzothiadiazole." Journal of the American Chemical Society 130.48 (2008): 16144-16145.

[24] Huo, Lijun, et al. "A Polybenzo [1, 2-b: 4, 5-b´] dithiophene Derivative with Deep HOMO Level and Its Application in High-Performance Polymer Solar Cells." Angewandte Chemie International Edition 49.8 (2010): 1500-1503.

[25] Chen, Chih-Ping, et al. "Low-bandgap poly (thiophene-phenylene-thiophene) derivatives with broaden absorption spectra for use in high-performance bulk-heterojunction polymer solar cells." Journal of the American Chemical Society 130.38 (2008): 12828-12833.

[26] You, Jingbi, et al. "Recent trends in polymer tandem solar cells research." Progress in polymer science 38.12 (2013): 1909-1928.

[27] Park, Soohyung, et al. "The origin of high PCE in PTB7 based photovoltaics: proper charge neutrality level and free energy of charge separation at PTB7/PC 71 BM interface." Scientific reports 6 (2016): 35262.

[28] Liu, Yongsheng, et al. "Solution-processed small-molecule solar cells: breaking the 10% power conversion efficiency." Scientific reports 3 (2013): 3356.

[29] Dou, Letian, et al. "A selenium-substituted low-bandgap polymer with versatile photovoltaic applications." Advanced Materials 25.6 (2013): 825-831.

[30] Collins, Samuel D., et al. "Small is Powerful: Recent Progress in Solution-Processed Small Molecule Solar Cells." Advanced Energy Materials 7.10 (2017).

[31] Yu, Gang, et al. "Polymer photovoltaic cells: enhanced efficiencies via a network of internal donor-acceptor heterojunctions." Science 270.5243 (1995): 1789-1791.

[32] Mi, Dongbo, et al. "Fullerene derivatives as electron acceptors for organic photovoltaic cells." Journal of nanoscience and nanotechnology 14.2 (2014): 1064-1084.

[33] Pal, Amrita, et al. "Comparative density functional theory–density functional tight binding study of fullerene derivatives: effects due to fullerene size, addends, and crystallinity on band structure, charge transport and optical properties." Physical Chemistry Chemical Physics 19.41 (2017): 28330-28343.

[34] Hashikawa, Yoshifumi, et al. "Synthesis and properties of endohedral aza [60] fullerenes: H2O@ C59N and H2@ C59N as their dimers and monomers." Journal of the American Chemical Society 138.12 (2016): 4096-4104.

[35] Nielsen, Christian B., et al. "Non-fullerene electron acceptors for use in organic solar cells." Accounts of chemical research 48.11 (2015): 2803-2812.

[36] Zhan, Chuanlang, Xinliang Zhang, and Jiannian Yao. "New advances in non-fullerene acceptor based organic solar cells." RSC Advances 5.113 (2015): 93002-93026.

[37] Benten, Hiroaki, et al. "Recent research progress of polymer donor/polymer acceptor blend solar cells." Journal of Materials Chemistry A 4.15 (2016): 5340-5365.

[38] Wang, Qungui, et al. "Non-Fullerene Acceptor-Based Solar Cells: From Structural Design to Interface Charge Separation and Charge Transport." Polymers 9.12 (2017): 692.

[39] Chen, Wangqiao, and Qichun Zhang. "Recent progress in non-fullerene small molecule acceptors in organic solar cells (OSCs)." Journal of Materials Chemistry C 5.6 (2017): 1275-1302.

[40] Zhao, Wenchao, et al. "Molecular optimization enables over 13% efficiency in organic solar cells." Journal of the American Chemical Society 139.21 (2017): 7148-7151.

[41] Lin, Hao, and Qiang Wang. "Non-fullerene small molecule electron acceptors for high-performance organic solar cells." Journal of Energy Chemistry (2017).

[42] Margulies, Eric A., et al. "Excimer formation in cofacial and slip-stacked perylene-3, 4: 9, 10-bis (dicarboximide) dimers on a redox-inactive triptycene scaffold." Physical Chemistry Chemical Physics 16.43 (2014): 23735-23742.

[43] Chen, Li-Min, et al. "Interface investigation and engineering–achieving high performance polymer photovoltaic devices." Journal of Materials Chemistry 20.13 (2010): 2575-2598.

[44] Lee, S-W., K. Hirakawa, and Y. Shimada. "Bound-to-continuum intersubband photocon-
ductivity of self-assembled InAs quantum dots in modulation-doped heterostructures." Ap-
plied Physics Letters 75.10 (1999): 1428-1430.

[45] Peumans, P., and S. R. Forrest. "Very-high-efficiency double-heterostructure copper ph-
thalocyanine/C 60 photovoltaic cells." Applied Physics Letters 79.1 (2001): 126-128.

[46] Park, Sung Heum, et al. "Bulk heterojunction solar cells with internal quantum efficiency
approaching 100%." Nature photonics 3.5 (2009): 297.

[47] Balis, Nikolaos, Emmanuel Stratakis, and Emmanuel Kymakis. "Graphene and transition
metal dichalcogenide nanosheets as charge transport layers for solution processed solar
cells." Materials Today 19.10 (2016): 580-594.

[48] Mor, Gopal K., et al. "High efficiency double heterojunction polymer photovoltaic cells using
highly ordered Ti O 2 nanotube arrays." Applied Physics Letters 91.15 (2007): 152111.

[49] Kołodziejczak-Radzimska, Agnieszka, and Teofil Jesionowski. "Zinc oxide—from synthesis
to application: a review." Materials 7.4 (2014): 2833-2881.

[50] Gadisa, Abay, et al. "Solution processed Al-doped ZnO nanoparticles/TiOx composite for
highly efficient inverted organic solar cells." ACS applied materials & interfaces 5.17 (2013):
8440-8445.

[51] Loiudice, Anna, et al. "Organic photovoltaic devices with colloidal TiO 2 nanorods as key
functional components." Physical Chemistry Chemical Physics 14.11 (2012): 3987-3995.

[52] Siddiki, Mahbube K., Swaminathan Venkatesan, and Qiquan Qiao. "Nb 2 O 5 as a new elec-
tron transport layer for double junction polymer solar cells." Physical Chemistry Chemical
Physics 14.14 (2012): 4682-4686.

[53] Trost, Sara, et al. "Room-temperature solution processed SnO x as an electron extraction
layer for inverted organic solar cells with superior thermal stability." Journal of Materials
Chemistry 22.32 (2012): 16224-16229.

[54] Yin, Zhigang, Jiajun Wei, and Qingdong Zheng. "Interfacial materials for organic solar
cells: recent advances and perspectives." Advanced Science 3.8 (2016).

[55] He, Zhicai, Hongbin Wu, and Yong Cao. "Recent advances in polymer solar cells: realization
of high device performance by incorporating water/alcohol-soluble conjugated polymers as
electrode buffer layer." Advanced Materials 26.7 (2014): 1006-1024.

[56] Reese, Matthew O., et al. "Optimal negative electrodes for poly (3-hexylthiophene):[6, 6]-
phenyl C61-butyric acid methyl ester bulk heterojunction photovoltaic devices." Applied
Physics Letters 92.5 (2008): 35.

BIBLIOGRAPHY

[57] Gupta, Vinay, et al. "Barium: an efficient cathode layer for bulk-heterojunction solar cells." Scientific reports 3 (2013): 1965.

[58] Chen, Fei, et al. "Tuning indium tin oxide work function with solution-processed alkali carbonate interfacial layers for high-efficiency inverted organic photovoltaic cells." Nanotechnology 24.48 (2013): 484011.

[59] Jia, Yuehua, et al. "Efficient polymer bulk heterojunction solar cells with cesium acetate as the cathode interfacial layer." Renewable energy 50 (2013): 565-569.

[60] Lindemann, William R., et al. "An X-ray fluorescence study on the segregation of Cs and I in an inverted organic solar cell." Organic Electronics 14.12 (2013): 3190-3194.

[61] Raïssi, Mahfoudh, Laurence Vignau, and Bernard Ratier. "Enhancing the short-circuit current, efficiency of inverted organic solar cells using tetra sulfonic copper phthalocyanine (TS-CuPc) as electron transporting layer." Organic Electronics 15.4 (2014): 913-919.

[62] Jia, Tao, et al. "Application of a water-soluble metallophthalocyanine derivative as a cathode interlayer for the polymer solar cells." Solar Energy Materials and Solar Cells 141 (2015): 93-100.

[63] Tan, Zhan'ao, et al. "High-Performance Inverted Polymer Solar Cells with Solution-Processed Titanium Chelate as Electron-Collecting Layer on ITO Electrode." Advanced Materials 24.11 (2012): 1476-1481.

[64] Jin, Sung H., et al. "Conformal coating of titanium suboxide on carbon nanotube networks by atomic layer deposition for inverted organic photovoltaic cells." Carbon 50.12 (2012): 4483-4488.

[65] Yang, Hong Bin, et al. "Graphene quantum dots-incorporated cathode buffer for improvement of inverted polymer solar cells." Solar Energy Materials and Solar Cells 117 (2013): 214-218.

[66] Liu, Jun, Michael Durstock, and Liming Dai. "Graphene oxide derivatives as hole-and electron-extraction layers for high-performance polymer solar cells." Energy & Environmental Science 7.4 (2014): 1297-1306.

[67] Small, Cephas E., et al. "High-efficiency inverted dithienogermole–thienopyrrolodione-based polymer solar cells." Nature Photonics 6.2 (2012): 115.

UNIVERSITAT ROVIRA I VIRGILI
NOVEL ELECTRON ACCEPTORS AND NEW SOLUTION PROCESSED HOLE BLOCKING LAYER FOR ORGANIC SOLAR CELLS
Caterina Stenta

UNIVERSITAT ROVIRA I VIRGILI
NOVEL ELECTRON ACCEPTORS AND NEW SOLUTION PROCESSED HOLE BLOCKING LAYER FOR ORGANIC SOLAR CELLS
Caterina Stenta

UNIVERSITAT
ROVIRA i VIRGILI